LABORATORY STUDIES OF SURFACE-ATMOSPHERE WATER EXCHANGE PROCESSES ON MARS

GEORGE NIKOLAKAKOS

A DISSERTATION SUBMITTED TO THE FACULTY OF GRADUATE STUDIES IN PARTIAL FULFILMENT OF THE REQUIREMENTS FOR THE DEGREE OF

DOCTOR OF PHILOSOPHY

GRADUATE PROGRAM IN PHYSICS AND ASTRONOMY
YORK UNIVERSITY
TORONTO, ONTARIO

SEPTEMBER 2018

Abstract

The recent discoveries of highly deliquescent perchlorate salts and strongly adsorbing porous minerals on the surface of Mars are intriguing as liquid brine solutions and adsorbed water could potentially provide a habitable environment for living organisms on present day Mars. A deeper understanding of these processes would also aid in the interpretation of data from past and present Mars missions, provide insight into the geological history of water on Mars, and assist in constraining the current inventory of water on Mars.

A Raman scattering lidar (light detection and ranging) instrument and environmental simulation chamber were developed to investigate the exchange of water between the atmosphere and surface of Mars. Raman scattering was applied to detect water uptake by samples of magnesium perchlorate hexahydrate. When exposed to the water vapour pressure and temperatures found at the landing site of the NASA Phoenix mission, magnesium perchlorate samples of the size found on Mars began to take up water from the atmosphere (deliquescence) at temperatures above the frost point temperature for pure water ice. Significant water uptake from the atmosphere began to occur within minutes, indicating that bulk deliquescence is likely to occur on present-day Mars. This demonstrates that perchlorate in the surface material can contribute to the hydrological cycle on Mars by absorbing water directly from the atmosphere and forming liquid water brine.

Chamber experiments were also conducted to study the adsorption of water on regolith grains. Raman spectroscopy was applied to study the adsorption properties of

zeolites under conditions found at the Mars Phoenix site. Experiments demonstrated that zeolites on the surface of Mars are capable of adsorbing water from the atmosphere on diurnal time scales and that Raman spectroscopy provides a promising method for detecting this process during a landed mission. When the water vapour pressure and temperature were low enough, the zeolite sample also adsorbed carbon dioxide, resulting in the simultaneous adsorption of water and carbon dioxide on the mineral grains. Additional experiments were carried out using a mixture of magnesium perchlorate and chabazite. The sample of mixed surface material remained visually unchanged during water adsorption, but darkened during deliquescence.

Dedication

To the memory of my mother.

Acknowledgements

I would like to express my great appreciation to my research supervisor Dr. James Whiteway for his support and for his confidence in my abilities. I have been fortunate to have a great deal of independence, generous access to laboratory resources and many opportunities to present my work during the course of this research project.

I would like to thank Dr. Michael Daly for serving on my supervisory committee for the entirety of my graduate studies and for allowing me access to his laboratory resources. I would also like to thank Dr. Frank Daerden for providing me access to and support with his Mars model data.

A special thanks to my good friends George Conidis and Evan Eshelman for providing invaluable conversations both personally and academically. To my uncle Anthony Nikolakakos for encouraging scientific thought at a young age. To Caroline Peterson for her love and support. And to Hunter, Catherine, and William for reminding me not to take life too seriously.

Lastly, this work would not have been possible without funding support from the NSERC CREATE Training Program for Integrating Atmospheric Chemistry and Physics from Earth to Space (IACPES).

Table of Contents

List of Tables

List of Figures

Preface

Sections of the following chapters of this dissertation have been adapted from previously published peer reviewed papers:

Chapter 4:

Nikolakakos, G., and J. A. Whiteway (2015), Laboratory investigation of perchlorate deliquescence at the surface of Mars with a Raman scattering lidar, Geophysical Research Letters, 42, 7899–7906, doi:10.1002/2015GL065434.

Chapter 5:

Nikolakakos, G., and J.A. Whiteway (2018), Laboratory study of adsorption and deliquescence on the surface of Mars, Icarus, 308, 221-229, doi:10.1016/j.icarus.2017.05.006.

Chapter One

Introduction

One of the central motivations driving planetary exploration is the search for habitable environments that could potentially support life. Water is essential to life as we know it and therefore increased knowledge about the current state of water on planets other than Earth is critical to this search. Despite presently being a relatively cold and dry planet, Mars displays an active water cycle which includes evidence for vast amounts of subsurface water ice [*Boynton et al.,* 2002], water ice clouds and precipitation [*Whiteway et al*., 2009], and frost formation on the surface [*Smith et al*., 2009]. While these processes all involve the vapour and solid ice phases, an open question is whether liquid water is possible given the current conditions on Mars.

The detection of perchlorate salt in the surface regolith of Mars [*Hecht et al.,* 2009] has been one of the most exciting recent discoveries in the field of planetary science. Perchlorate is capable of absorbing water vapour directly from the atmosphere and forming a liquid water brine solution which could be stable on the surface of present day Mars [*Chevrier et al.,* 2009]. This discovery has been further bolstered by the visual identification of dark streaks on steep slopes on the surface of Mars which appear to incrementally grow and fade on a seasonal basis [*McEwen et al*., 2011]. These features, termed Recurring Slope Lineae, have been spectroscopically associated with perchlorate salts and are thought to be the result of seeping liquid water, likely in the form of

perchlorate brine [*Ojha et al.*, 2015]. In addition to liquid salt solutions, there is strong evidence that water can also exist on Mars in the form of liquid-like adsorbed water, thin films that form on the surface of certain types of porous minerals [*Jakosky et al.*, 1983].

The study of these processes is of great importance, as previous research has suggested that both salt solutions and adsorbed water may be able to support microbial life under environmental conditions similar to those presently found on Mars [*Mohlmann et al.*, 2005; *Davila et al.*, 2010]. Additionally, these processes may be able to strongly influence the current Martian hydrological cycle [*Hecht et al*., 2009; *Jakosky et al.*, 1983]. This has implications for the geological history of Mars as well as for determining the current global inventory of water.

This dissertation summarizes research conducted since September 2011 towards completion of the PhD program in the Department of Physics and Astronomy at York University. The work has sought to answer three essential questions:

1. Can Raman scattering spectroscopy be used to detect and discriminate between the different processes and minerals that are associated with the exchange of water between the atmosphere and the surface on Mars?
2. Are the processes of salt deliquescence and surface regolith water adsorption currently contributing to the hydrological cycle on Mars? If so, can these processes explain observations made by instruments during landed and orbital missions to Mars?
3. Can water presently exist on Mars in phases other than ice and vapour (e.g. liquid)? If so, where and when is this water found on the surface of Mars?

The research presented in this dissertation provides evidence in support of answering each of these questions. The following chapters offer a detailed description of the work that has been carried out to arrive at the answers.

Chapter 2 provides context for the experiments that were performed in this project by giving an overview of the current understanding of the Martian water cycle. The chapter begins with a review of the terminology and thermodynamic concepts that are relevant to the phase transitions of water. A description of the various surface-atmosphere water exchange processes involving the vapour and ice phases is then presented. These processes have been detected by a variety of instruments on board landed and orbital missions to Mars. An explanation of the theory behind the deliquescence and efflorescence of salts as well as the freezing point depression of salt solutions is then provided. This is followed by a discussion on the detection of perchlorate salts on Mars and evidence for possible liquid water flows on present day Mars. The chapter concludes with an overview of the theory of adsorption and a description of microporous minerals such as zeolites.

Chapter 3 discusses the instrumentation developed for this work, introduced by an overview of Raman scattering theory. A detailed description of the experimental setup that was designed and constructed for the research project is then provided. This includes an ultraviolet Raman spectroscopy lidar (light detection and ranging) instrument and an optically coupled environmental simulation chamber.

Chapter 4 presents experiments that have examined the deliquescence, efflorescence and freezing of magnesium perchlorate salt. In these experiments, a sample

of magnesium perchlorate was subjected to the water vapour partial pressure and temperatures found at the landing site of the Phoenix Mars mission. Laser Raman scattering was applied to detect the onset of deliquescence and provide a relative estimate of the quantity of water taken up and subsequently released by the sample. As the temperature of the sample decreased at the same rate as measured on Mars during the evening, significant uptake of water from the atmosphere was observed to occur prior to the frost point temperature being reached. The resulting liquid water brine solution was found to freeze at the eutectic temperature of -67°C. This is the first experimental study to examine the bulk deliquescence and freezing of perchlorate salts under realistic Martian conditions. These experimental results were then combined with the output of a general circulation model of Mars to determine the likely global and seasonal distribution of magnesium perchlorate brine at the surface of Mars.

Chapter 5 builds on the investigations of pure magnesium perchlorate by presenting experimental studies on the adsorption of water by zeolite minerals, as well as the deliquescence of perchlorate in the presence of adsorbed water. A sample of the zeolitic mineral chabazite was subjected to a range of water vapour partial pressures and temperatures found on present day Mars. Laser Raman scattering was applied to detect the relative amounts of water and carbon dioxide adsorbed by the sample. Results show that zeolites are capable of adsorbing water from the atmosphere on diurnal time scales and that Raman scattering spectroscopy provides a promising method for detecting this process during a landed mission. When the water vapour partial pressure and temperature were sufficiently low, the zeolite sample also adsorbed carbon dioxide, resulting in the simultaneous adsorption of water and carbon dioxide on the surface of the mineral grains.

It was previously unknown whether the process of water adsorption by the regolith was rapid enough to influence the diurnal water cycle under current Martian conditions and this study demonstrated that zeolite adsorption occurs on the order of one hour. Additional experiments were carried out using a mixture of magnesium perchlorate and chabazite. The sample of mixed surface material remained visually unchanged during water adsorption, but was found to darken during deliquescence. This confirmed that the deliquescence of perchlorate and regolith mixtures can produce the darkening associated with Recurring Slope Lineae streaks. This is the first time that the deliquescence of perchlorate/regolith mixtures has been examined under realistic Martian conditions, and more notably the first time that the deliquescence of perchlorate has been investigated in the presence of adsorbed water.

Chapter 6 provides an overall summary of the work presented in this dissertation, and Chapter 7 concludes by proposing potential experimental improvements and future scientific investigations.

Chapter Two

Background

2.1 Mars

With the exception of Earth, Mars is the most hospitable planet in our solar system. Numerous geological features indicate that large quantities of liquid water likely flowed at one time on the surface of ancient Mars. These features include valley networks and channels [*Carr,* 1995], open-basin lakes [*Fassett and Head*, 2008], and possible ancient ocean shorelines [*Head et al*., 1999]. While debate exists over whether early Mars was warm and wet, cold and wet, or some combination of the two [*Carr and Head,* 2010], these early flows of liquid water were likely sustained by environmental conditions that would have been capable of supporting primitive life [*Grotzinger et al.,* 2014]. Geological and mineralogical evidence suggests that this wet period on Mars ended approximately 3.8 to 3.0 billion years ago [*Bibring et al.,* 2006].

Present day Mars has a thin atmosphere that is composed primarily of carbon dioxide. The average surface pressure is 600 Pa, which is less than 1% of that on Earth, and varies seasonally as carbon dioxide condenses out of the atmosphere and is deposited at the poles during the winter seasons. Mars orbits the Sun at an average distance of 227.9 million km (1.524 AU) and does not feature a significant greenhouse effect, resulting in an average surface temperature of approximately -60˚C [*McKay et al.*, 1991]. The combination of low surface pressures and temperatures does not allow pure liquid water

to currently be stable on the surface, however water is present in both the ice and vapour phases and possibly also in the form of liquid brine solutions and liquid-like adsorbed water.

Water is constantly exchanged between the atmosphere and the surface of Mars, resulting in a subtle but distinct Martian hydrological cycle. A deeper understanding of the processes involved in this water cycle is vital to determining the present global inventory of water, to understanding the history and future evolution of water on Mars, and to exploring whether life could presently survive on Mars.

2.2 Surface-Atmosphere Water Exchange Processes on Mars

The partial pressure of water vapour (e) is a measure of the pressure exerted by water vapour molecules in a volume of mixed air and increases as the amount of water vapour in the air increases. The saturation (equilibrium) vapour pressure is a function of temperature and is defined as the partial pressure of water vapour when the rate of water molecules evaporating from a flat surface of water to the air is equal to the rate of water molecules that are condensing from the air to the surface. At a given temperature, the saturation vapour pressure with respect to liquid water (e_s) is always greater than the saturation vapour pressure with respect to ice (e_i).

These quantities are commonly expressed in terms of relative humidity (RH), which is equal to $(e/e_s)*100\%$. At temperatures above the freezing point of pure water (0˚C), relative humidity is computed with respect to liquid water, but is generally calculated with respect to ice (RHi) at temperatures below freezing (the typical case on Mars). The dew point temperature (T_d) is also a commonly used measure of the

atmospheric water vapour content, where T_d is the temperature to which air would need to be cooled for the relative humidity to be 100% ($e=e_s$). When the temperature is below the freezing point of pure water (0˚C), this quantity is computed with respect to ice and is called the frost point temperature (T_f). The dew point or frost point temperature is a function of the partial pressure of water vapour. Conversions between these quantities in this dissertation have been calculated using the water vapour pressure equations of *Buck* [1981].

The air is said to be saturated with water vapour when the partial pressure of water vapour is equal to the saturation vapour pressure above the surface ($e=e_s$ or $e=e_i$; RH=100% or RHi=100%; $T=T_d$ or $T=T_f$). If the partial pressure of water vapour exceeds the saturation vapour pressure, the air is said to be supersaturated. When saturation occurs, $e \geq e_s$ (or $e \geq e_i$), the rate of condensation (or deposition) to the surface will exceed the rate of evaporation (or sublimation) from the surface such that a net amount of water vapour is deposited onto the surface. The rate at which the vapour is deposited depends on several factors including the difference between the partial pressure and the saturation pressure, the temperature, and the total air pressure. During this process, water vapour molecules are transferred to the surface in either the liquid phase (condensation) or the ice phase (deposition). The opposite occurs when the partial pressure of water vapour is less than the saturation vapour pressure ($e < e_s$ or $e < e_i$). In this case the rate of evaporation (or sublimation) from the surface will exceed the rate of condensation (or deposition) to the surface and a net amount of water vapour molecules will leave the surface of the liquid or the ice phase and enter the atmosphere in the vapour phase. These thermodynamic processes drive much of the Martian water cycle, both on a seasonal and daily time scale.

Several surface-atmosphere water exchange processes have been directly observed to occur on Mars. These include seasonal water ice cap deposition and sublimation [*Haberle and Jakosky*, 1990], daily cycles of frost deposition and sublimation [*Smith et al.*, 2009], and water ice cloud formation, precipitation, and sublimation [*Whiteway et al.*, 2009]. Other processes have yet to be directly observed, but have been speculated to occur based on meteorological and mineralogical data returned from orbital and landed Mars exploration missions. These include the deliquescence and efflorescence of salts [*Hecht et al.*, 2009] and the adsorption and desorption of water from surface mineral grains [*Jakosky and Farmer*, 1982]. A description of these processes is presented in the sections that follow with emphasis on deliquescence and adsorption. These two processes are of great importance as they have potential implications for life on Mars and could significantly influence the Martian hydrological cycle. Figure 2.1 provides a visual overview of the various processes involved in the present Martian water cycle.

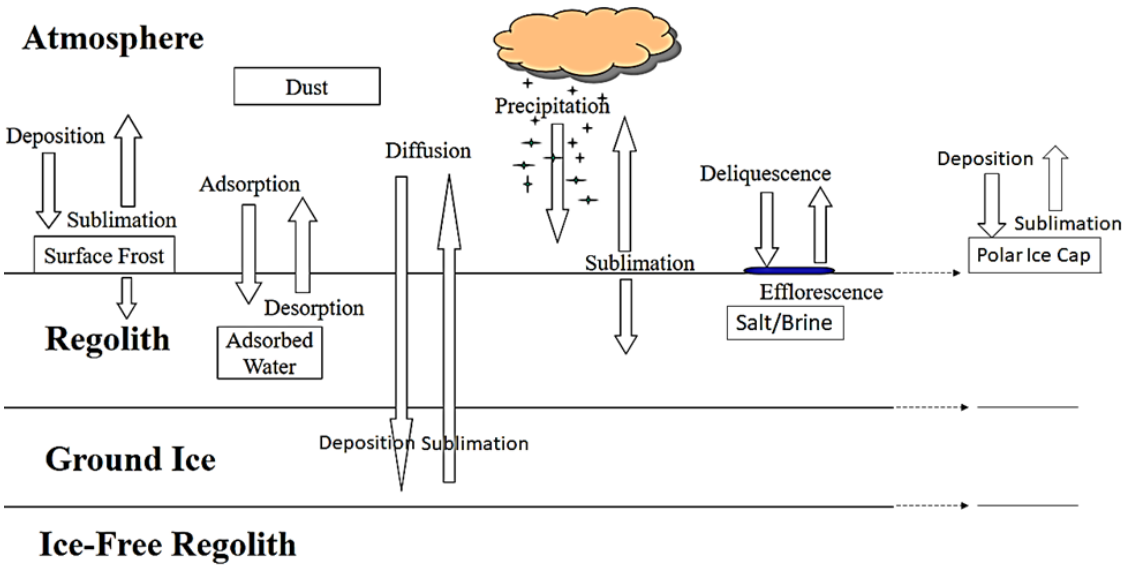

Figure 2.1. Summary of the processes involved in the Martian water cycle.

2.3 Water Vapour on Mars

In addition to carbon dioxide, the Martian atmosphere is composed of several trace constituents including water vapour. Water vapour on Mars was first detected spectroscopically using Earth-based astronomical observations [*Spinrad et al.,* 1963], and has since been more thoroughly mapped by instruments on board spacecraft in orbit around Mars. The Mars Atmospheric Water Detector Experiment (MAWD) on the Viking Orbiter provided the first global measurements of water vapour using near-infrared spectroscopy [*Jakosky and Farmer*, 1982]. More recently the Thermal Emission Spectrometer (TES) instrument on the Mars Global Surveyor [*Smith*, 2004] and the Spectroscopy for Investigation of Characteristics of the Atmosphere of Mars (SPICAM) spectrometer on the Mars Express orbiter [*Trokhimovskiy et al.*, 2015] have provided higher temporal and spatial resolution measurements of vertically integrated column abundances of water vapour on Mars.

Figure 2.2 shows the seasonal and latitudinal distribution of water vapour column abundance, expressed in units of precipitable microns, on Mars based on a four-year average of SPICAM orbital measurements [*Trokhimovskiy et al.*, 2015]. Time is expressed on the x-axis in terms of solar longitude (Ls), where Ls=90° represents the northern hemisphere summer solstice. The largest quantities of water vapour are found near the north pole following the time of the northern hemisphere summer solstice as warming temperatures result in the sublimation of water ice from the northern polar ice cap (see Sec. 2.6 for more on the polar ice caps). This water re-enters the atmosphere in the vapour phase and is gradually transported equatorward as the northern summer season progresses. Water is also released from the surface in response to warming local

temperatures as water sublimates from the subsurface ice table (see Sec. 2.5), is desorbed from surface mineral grains (see Sec. 2.12) or is effloresced from salt brines (see Sec 2.10). A similar, but less substantial seasonal water vapour pattern is observed at the south pole during the southern hemisphere summer season. Water vapour abundances near the poles are observed to fall dramatically during their respective winters when decreasing temperatures lead to the deposition of atmospheric water vapour back to the surface. Unlike the polar and midlatitude regions, which experience dramatic seasonal changes in atmospheric water vapour content, the maximum water vapour abundance is significantly lower near the equator and remains nearly constant throughout the Martian year.

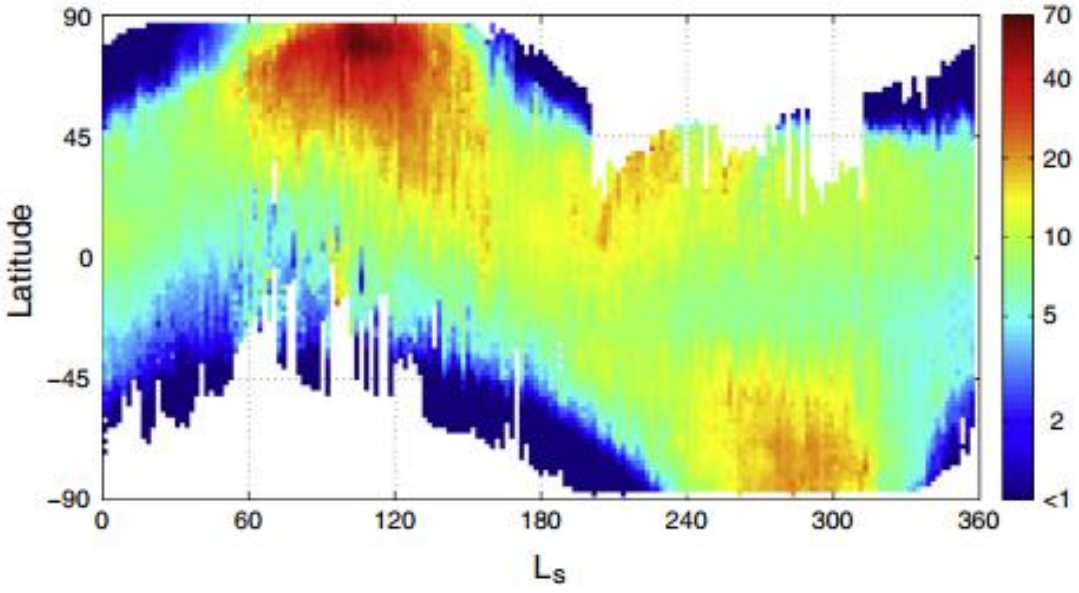

Figure 2.2. SPICAM measurements of column water vapour abundance on Mars (units of precipitable microns) [figure taken from *Trokhimovskiy et al*., 2015].

While the precise vertical distribution of water vapour near the surface on Mars has not been measured directly, landed missions have provided measurements of the atmospheric water vapour content near the surface. The NASA Mars Phoenix Lander operated in the northern arctic region of Mars (68.22°N, 234.25°E) for 5 months starting on 25 May 2008. The duration of the mission covered the northern hemisphere late spring and summer seasons, which corresponded to the solar longitude period between Ls=76.5° and Ls=148° [*Smith et al*., 2009]. Among the instrument payload was the Thermal and Electrical Conductivity Probe (TECP) which provided measurements of atmospheric humidity near the surface over the entirety of the mission. Initial TECP results (Fig. 2.3) showed a distinct repeating daily cycle in which the atmospheric water vapour abundance at the Phoenix site reached a maximum plateau during the daytime with the partial pressure of water vapour reaching a high of 2 Pa. The water vapour pressure was then observed to decrease dramatically in the evening, often prior to 100% relative humidity (over ice) being reached, before again increasing and reaching a plateau of 2 Pa during the daytime [*Zent et al*., 2010]. Figure 2.3 shows a plot of the measured atmospheric frost point temperature, the atmospheric temperature at a height of 1 meter, and the modelled surface temperature during sol 70 of the mission. A decrease in the atmospheric water vapour content begins around 19h (as indicated by a drop in the frost point temperature), but the air does not become saturated with respect to water until several hours later when the ground and air temperatures match the frost point temperature. This indicates that a significant exchange of water is occurring between the atmosphere and surface of Mars which cannot be explained by frost deposition alone. Current knowledge of Martian surface mineralogy suggests that the processes most likely responsible for this exchange

are deliquescence of salts such as perchlorate [*Hecht et al.,* 2009] and/or the adsorption of water onto mineral grains [*Jakosky et al.,* 1997].

A new TECP calibration function was later provided which greatly reduced the measured water vapour quantities at the Phoenix site [*Zent et al*., 2016]. A similar diurnal pattern of evening decrease and morning increase was observed, but the maximum partial pressure of water vapour at the Phoenix was now suggested to be just 0.5 Pa.

Relative humidity at the surface of Mars has also been measured by the Rover Environmental Monitoring Station (REMS) instrument on the NASA Curiosity rover at Gale Crater near the Martian equator (4.59°S, 137.44°E) [*Harri et al.,* 2014]. The Curiosity rover is part of the Mars Science Laboratory (MSL) mission and has been active since landing on Mars on August 6, 2012. The atmospheric water vapour content at this site has been measured to be significantly lower than at the polar Phoenix site, with a maximum partial pressure of just 0.2 Pa. Despite these much drier conditions, a similar diurnal pattern of atmospheric water vapour depletion has been observed in the evening prior to saturation being reached. This suggests that adsorption, deliquescence, or both may also be active processes at this site [*Savijarvi et al*., 2015; *Martin-Torres et al*., 2015].

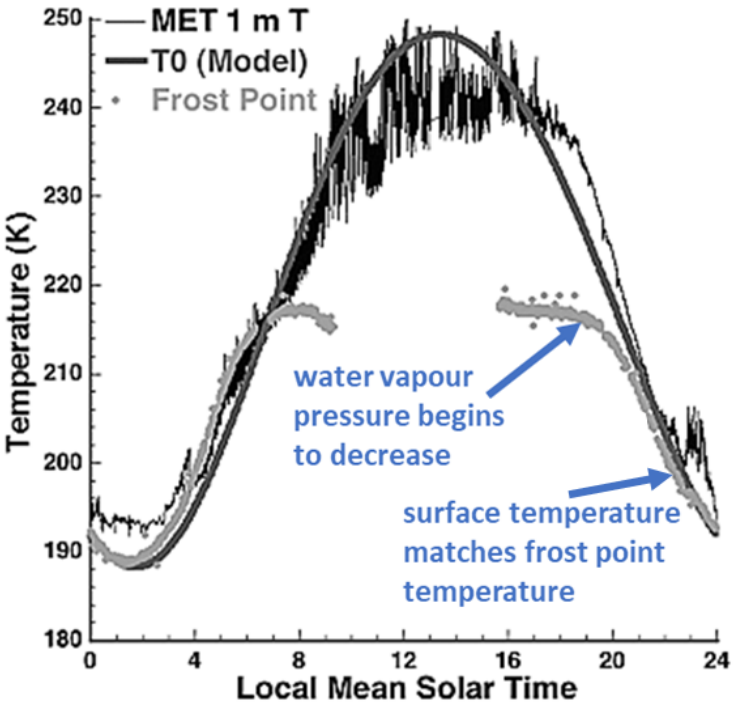

Figure 2.3. TECP measurements of atmospheric water vapour content (expressed in terms of frost point temperature), air temperature at 1-m height, and modelled surface temperature at the Phoenix site on sol 70 of the mission [figure modified from *Zent et al.* 2010].

2.4 Surface Frost Deposition and Sublimation

Surface water frost occurs when air near the ground becomes saturated with respect to water ice ($e \geq e_i$) and atmospheric water vapour is deposited as ice when it encounters the surface. Frost formation was imaged at the high northern latitude Mars Phoenix site by the Stereo Surface Imager (SSI) on the NASA Mars Phoenix Lander. The surface of the Phoenix landing site was found to be free of water ice during late spring and early summer until frost formation was first observed on sol 80 of the mission (Ls ~

112°) [*Cull et al.*, 2010]. Ground frosts were observed sporadically between sol 80 and sol 110 and more frequently afterwards [*Nelli et al*., 2010]. These frosts formed during the night as the ground cooled and then sublimated during the daytime as the surface temperature warmed. This diurnal cycle of frost formation and sublimation continued until the end of the mission in late summer [*Smith et al.*, 2009]. Figure 2.4 shows an SSI image of frost formation at the Phoenix site captured during the morning of sol 80 of the mission.

A thin, light coloured ground cover was also imaged at the northern NASA Viking 2 lander site (47.97°N, 225.74°W). This ground cover persisted for 249 Martian days during the first winter of the mission before sublimating, and it was concluded that this layer was composed of water frost [*Svitek and Murray*, 1990].

Surface frost formation has not been directly detected at lower latitudes, but has been inferred to occur at equatorial Gale Crater based on relative humidity and surface temperature measurements made by instruments on the NASA Mars Curiosity rover [*Martinez et al.*, 2016].

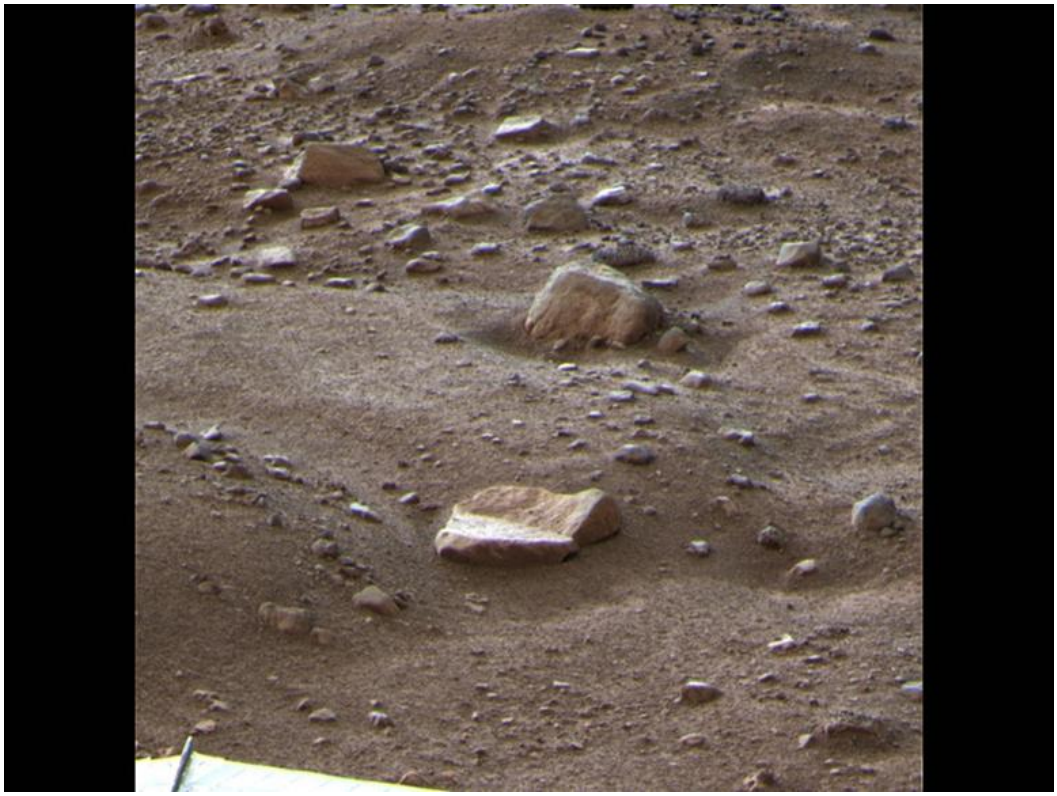

Figure 2.4. Surface frost imaged at the Mars Phoenix site on sol 80 of the mission [figure taken from *Smith et al.,* 2009].

2.5 Mars Subsurface Water Ice Table

The existence of vast amounts of water ice in the Martian subsurface was first suggested based on thermal and diffusive calculations [*Leighton and Murray*, 1966; *Mellon and Jakosky*, 1993] and the first observational evidence came from data acquired by the Gamma-Ray Spectrometer on the Mars Odyssey orbiter, which identified regions near the poles that were enriched in hydrogen [*Boynton et al.*, 2002]. Further evidence for the sub-surface water ice table was provided by the Mars Phoenix lander when trenches dug to a depth of 4 to 5 cm revealed bright material that was observed to sublimate during

the course of the mission [*Smith et al.,* 2009]. This was confirmed to be water ice when a sample of ice-cemented soil material from the bottom of a trench was heated by the Phoenix TEGA (Thermal and Evolved-Gas Analyzer) instrument and an endothermic peak was observed that was consistent with the melting of water ice. Figure 2.5 shows an image of subsurface water ice directly below the Phoenix lander which was captured by the Robotic Arm Camera. This subsurface ice was exposed when the Phoenix lander thrusters dispersed the overlying regolith during landing. The subsurface water ice that was identified at the Phoenix site consisted of both pore ice, located in the spaces between regolith particles, and nearly pure ice.

Experiments [*Hudson et al.,* 2009] and theoretical calculations [*Mellon et al.,* 1997] have shown that water can be actively exchanged between the atmosphere and the sub-surface through sublimation and deposition at the ice table surface. This process is expected to be controlled by the rate of diffusion of water vapour through the overlying surface regolith layer. While this mechanism is consistent with the presence of the subsurface pore ice, the emplacement of the nearly pure ice would have required a liquid (or brine) water phase [*Smith et al.,* 2009].

Figure 2.5. Subsurface water ice imaged under the Phoenix lander at the Mars Phoenix site [figure taken from *Smith et al*. 2009].

2.6 Mars Polar Ice Caps

Among the more distinct visual features on Mars are the polar ice caps which represent the largest reservoir of water on present day Mars. The north polar cap acts as the main source of atmospheric water vapour on Mars. Figure 2.6 shows images of the north polar ice cap taken from orbit by the Mars Reconnaissance Orbiter's Mars Color Imager (MARCI) instrument during the northern hemisphere late spring and summer seasons on Mars. The northern water ice cap is covered by a deposited carbon dioxide cap during the winter, but becomes exposed when the carbon dioxide sublimates back to the atmosphere during the spring and summer seasons. The exposed water ice cap then begins to sublimate and water enters the atmosphere in the vapour phase [*Haberle and Jakosky*,

1990]. The northern cap acts as a sink for water vapour during the cold seasons as water is deposited back to the cap in the form of ice and is then covered by the seasonal carbon dioxide cap. A similar but less dramatic pattern is observed at the south polar cap with water vapour being released during the southern hemisphere summer and redeposited during the colder seasons.

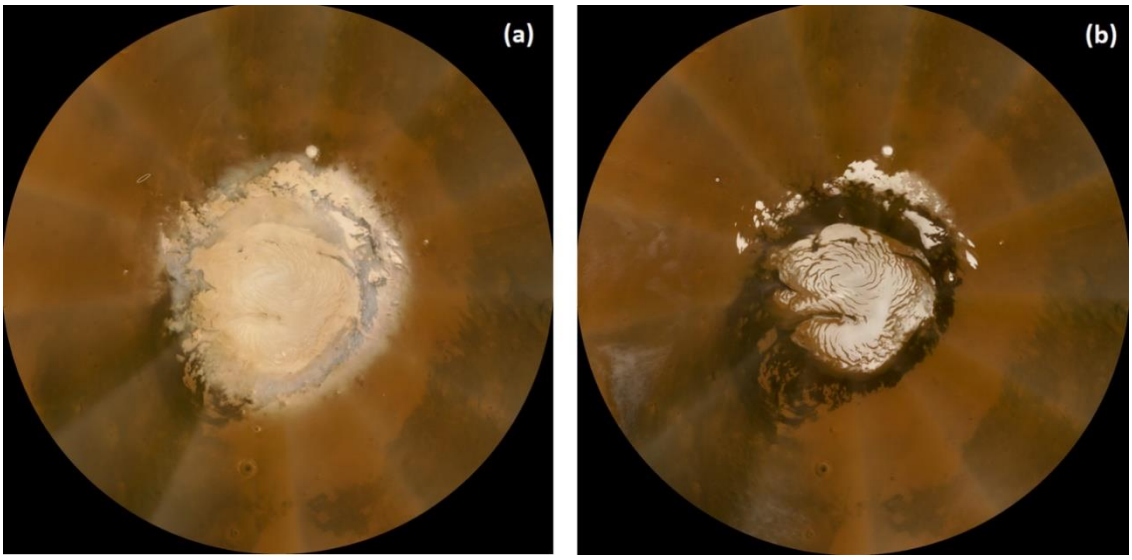

Figure 2.6. Images showing the seasonal evolution of the north polar ice cap on Mars. These images were captured from orbit by the Mars Reconnaissance Orbiter's Mars Color Imager (MARCI) on **(a)** 4 May 2008, corresponding to late northern hemisphere spring on Mars and **(b)** 20 September 2008, corresponding to late northern hemisphere summer on Mars [figures taken from *NASA/JPL*, 2008].

2.7 Water Ice Clouds and Precipitation

Clouds form when the air becomes saturated with respect to water and atmospheric water vapour molecules condense to form visible liquid water droplets or deposit as ice crystals. This condensation or deposition occurs on the surface of suspended aerosol particles (heterogeneous nucleation) [*Pruppacher and Klett*, 2012]. The Martian atmosphere contains abundant amounts of dust that can serve as cloud condensation nuclei [*Komguem et al.*, 2013].

Water ice clouds were first detected on Mars by the interferometer spectrometer on board the NASA Mariner 9 Mars orbiter [*Curren et al.,* 1973]. More comprehensive global mapping of high altitude water ice clouds has since been undertaken using spectroscopic and visual measurements from orbiters such as the Mars Global Surveyor (MGS) [*Pearl et al.,* 2001].

The Lidar (light detection and ranging) instrument on the Mars Phoenix lander provided the first vertically resolved measurements of dust and clouds above the surface of Mars. A regular pattern of cloud formation was detected each night within the planetary boundary layer beginning during the late summer season [*Whiteway et al.,* 2009]. Water ice crystals were observed to grow and precipitate through the atmosphere to the surface during the night where they eventually sublimated and re-entered the atmosphere in the vapour phase when temperatures warmed during the morning hours. Figure 2.7 shows a contour plot of the backscatter coefficient ($\times 10^{-6}$ m^{-1} sr^{-1}) derived from the Phoenix Lidar backscatter signal at a laser wavelength of 532 nm on sol 99 of the mission. The enhanced backscatter observed between a height of 3 and 4 km traces the structure of the clouds that passed above the Phoenix site. These clouds were found to form at an estimated

temperature of -62˚C which was consistent with water ice crystals [*Whiteway et al*., 2009]. The vertical streaks observed at the base of the cloud after 05:00 am (Mars local time) were indicative of water ice crystals precipitating from the cloud and then sublimating in the drier air below the cloud. These precipitation streaks were observed to reach the ground later in the mission, indicating that water was regularly exchanged between the atmosphere and the surface through a cycle of cloud formation, precipitation, and sublimation.

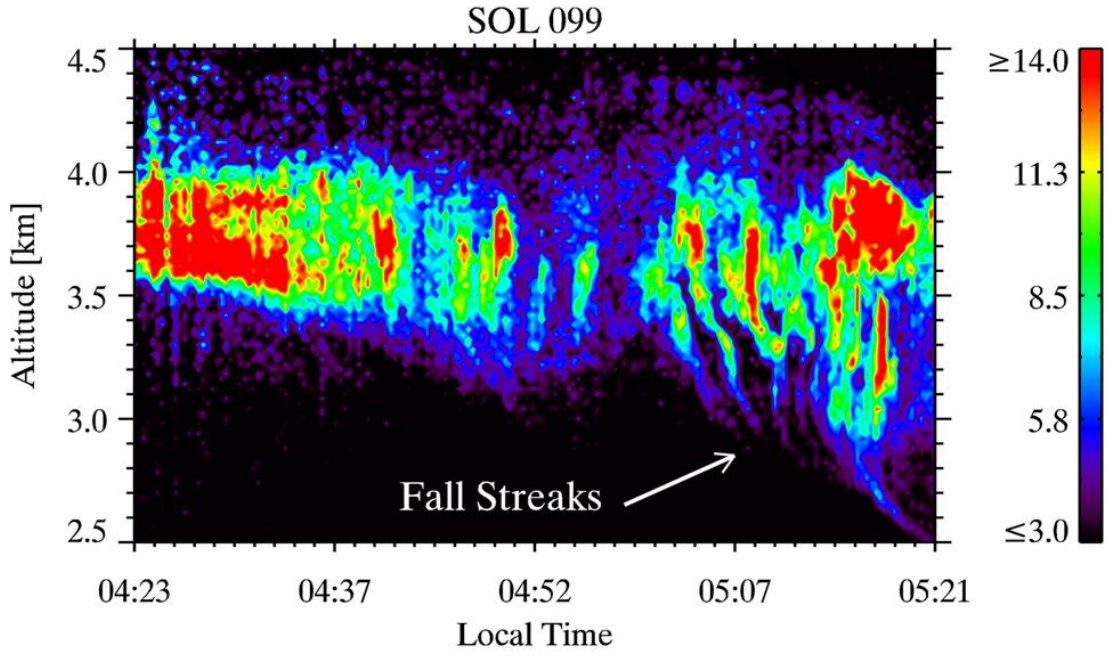

Figure 2.7. Lidar measurements of backscatter coefficient ($\times 10^{-6}$ m^{-1} sr^{-1}) showing water ice clouds and precipitation above the Mars Phoenix site during sol 99 of the mission [figure taken from *Whiteway et al.*, 2009].

2.8 Chemically Bound Water of Hydration

A mineral is said to be hydrated when molecules of water (H_2O) or hydroxyl (OH) are chemically bound within the crystal structure of the mineral. A variety of hydrated minerals have been detected on Mars including sulphates, phyllosilicates, zeolites, and chlorides [*Wray et al.,* 2009]. Many of these hydrated minerals are formed exclusively through long-term contact with liquid water and are therefore used to provide constraints on the climate history of Mars, which may have included warm and wet periods [*Ehlmann et al.,* 2009].

It has also been suggested that certain minerals on Mars can presently alter their hydration state by taking up atmospheric water vapour directly into their mineral structure or by losing water of hydration to the atmosphere. For example, the magnesium sulphate hydration transition between starkeyite ($MgSO_4 \cdot 4H_2O$) and epsomite ($MgSO_4 \cdot 7H_2O$) is expected to be thermodynamically favourable under current Martian surface conditions [*Chou and Seal,* 2007].

2.9 Deliquescence, Efflorescence, and Freezing Point Depression of Salts

Water-soluble particles such as inorganic salts are capable of absorbing water vapour from the atmosphere and forming a liquid solution. This process is known as deliquescence and occurs when the vapour pressure over the salt solution is less than the partial pressure of water vapour in the air [*Martin,* 2000].

Deliquescence is initiated when water vapour molecules are adsorbed onto the dry surface of a salt particle due to the polar attraction between the water molecules and the ions that make up the salt (see Sec. 2.12 for more on adsorption). If the relative humidity

of the air surrounding the particle increases, the amount of adsorbed water molecules on the surface of the particle will also increase until a critical point is reached where the concentration of adsorbed water is sufficient to break the ionic bonds of the salt particle and disturb the crystal lattice structure [*Harmon et al.*, 2010]. The point at which the salt particle is dissolved is commonly expressed in terms of the deliquescence relative humidity (DRH), where the relative humidity is the ratio of the partial pressure of water vapour to the saturation vapour pressure (equilibrium with respect to a flat surface of pure liquid water or water ice) at a given temperature multiplied by 100%. Deliquescence is generally observed to occur at values of relative humidity below 100%.

The addition of a non-volatile solute such as salt to a solvent such as water results in a reduction in the rate of evaporation of the solvent. This in turn leads to a lower vapour pressure over the salt solution as compared to the equilibrium (or saturation) vapour pressure that would exist over pure liquid water at the same temperature. The reduced vapour pressure over the salt solution drives the further uptake of atmospheric water vapour molecules and leads to further dissolving of the salt. An increase in the relative humidity will result in increased water uptake from the atmosphere. Water uptake will continue until the salt is completely dissolved in the solution and the solution has reached an equilibrium with the atmosphere such that the vapour pressure over the solution is equal to the partial pressure of water vapour in the air.

The reverse process, efflorescence, is the re-crystallization of the salt as liquid water is released back to the atmosphere when the ambient relative humidity is reduced below the DRH. Water molecules will evaporate from the surface of the solution and re-enter the atmosphere if the vapour pressure over the solution exceeds the partial pressure

of water vapour in the air. As water is evaporated, the solution becomes increasingly supersaturated with respect to the solid salt until a critical value of salt supersaturation is reached and the salt is completely recrystallized. The point at which this occurs is commonly expressed in terms of the efflorescence relative humidity (ERH) and typically occurs at a much lower relative humidity than the DRH. For example, the DRH of sodium chloride (NaCl) at 25˚C has been experimentally determined to be 75%, while the ERH of NaCl at the same temperature was found to be 43% [*Czisco and Abbatt*, 2000].

Figure 2.8 shows a summary of the deliquescence-efflorescence cycle for a typical inorganic salt. As the relative humidity increases around an initially dry salt particle, there are no immediate changes in the liquid water content of the salt (path A). When the relative humidity reaches a critical value (the DRH), the salt particle begins to take up water vapour from the atmosphere, dissolves, and forms a liquid solution (path B). Given enough time, the solution will reach an equilibrium with the atmosphere (the rate at which water molecules evaporate from the surface of the solution matches the rate at which water molecules condense from the air to the solution) and the uptake of water will cease. At this point the vapour pressure of the solution is equal to the partial pressure of water vapour in the air. Further increases in relative humidity will result in further uptake of atmospheric water vapour and increased growth of the liquid solution. When the relative humidity drops, water will begin to evaporate from the solution and re-enter the atmosphere as vapour (path C), however the salt will only completely recrystallize when the ERH is reached (path D).

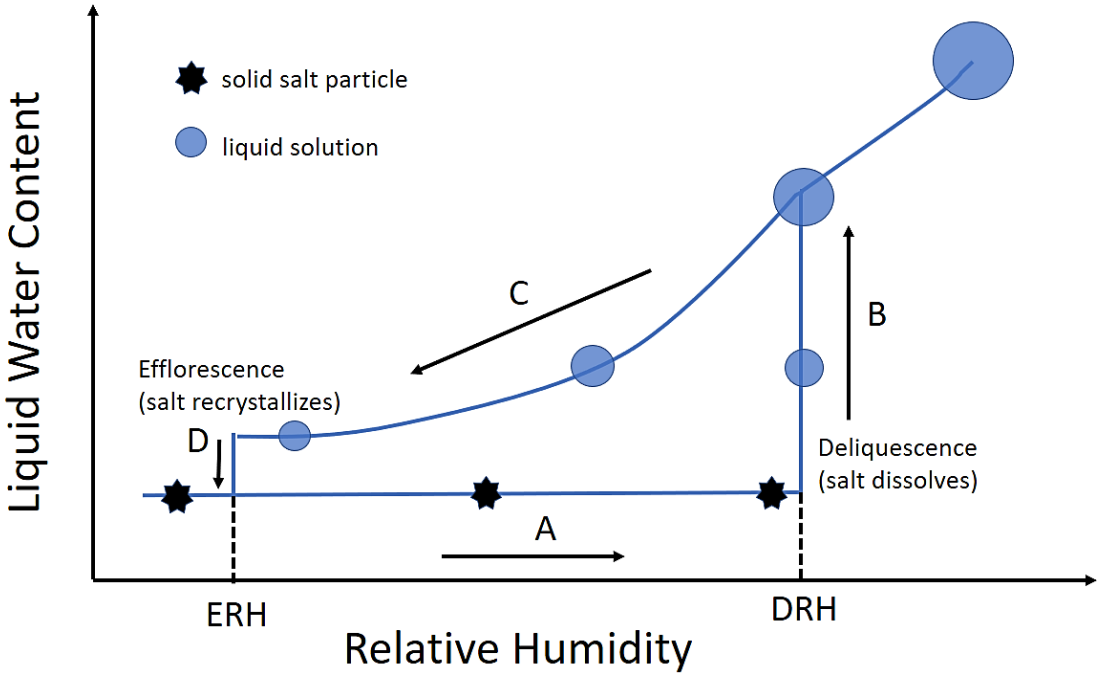

Figure 2.8. Diagram of the deliquescence and efflorescence cycle for a typical inorganic salt. An initially dry salt particle takes up water and forms a solution at the deliquescence relative humidity, but does not completely recrystallize until the efflorescence relative humidity is reached.

A further consequence of the lowered vapour pressure of a salt solution is a depression in the freezing point of the solution as compared to the freezing point of pure water [*Petrucci and Harwood,* 1993]. The freezing point is defined as the temperature at which the liquid and solid phases of a substance can coexist in equilibrium. It occurs at the temperature at which the saturated (or equilibrium) vapour pressure over the solid phase (e_i) is equal to the equilibrium vapour pressure over the liquid phase (e_s). This effect is illustrated in Fig. 2.9 which shows the vapour pressure over pure liquid water (red) as well the lowered vapour pressure over a typical salt solution (black). The equilibrium vapour pressure over pure water ice (blue) matches the equilibrium vapour pressure of pure liquid water at 0˚C, resulting in the well known freezing point for pure liquid water. On the other hand, the lowered equilibrium vapour pressure over the aqueous salt solution equals the equilibrium vapour pressure of pure water ice at a lower temperature, marked on the diagram as point Te. The solution remains in the liquid phase at temperature above Te and this results in freezing points of salt solutions that are substantially lower than the 0˚C-freezing point temperature of pure water.

The maximum freezing point depression for a salt solution is termed the eutectic temperature and is achieved when the concentration of salt in the solution is greater than or equal to the eutectic composition. For example, sodium chloride solution has a freezing point (eutectic) temperature of -21.2˚C with a eutectic composition of 23.3% salt [*Bodnar*, 1993]. Figure 2.10 shows the eutectic phase diagram for a typical inorganic salt solution and illustrates the possible phase transitions that the solution can undergo [*Clugston and Flemming,* 2000]. If the solution is diluted such that the concentration of salt is less than the eutectic composition (marked by the vertical dashed line), a mixture of water ice and

liquid solution will be present at temperatures above the eutectic temperature and below the freezing point of pure water (region A). At salt concentrations greater than the eutectic composition, the solution is said to be super-saturated with salt and will contain a mixture of solid salt and salt solution at temperatures above the eutectic temperature (region B). Below the eutectic temperature, the solution will freeze, and the result will be separated components of water ice and solid salt (region C).

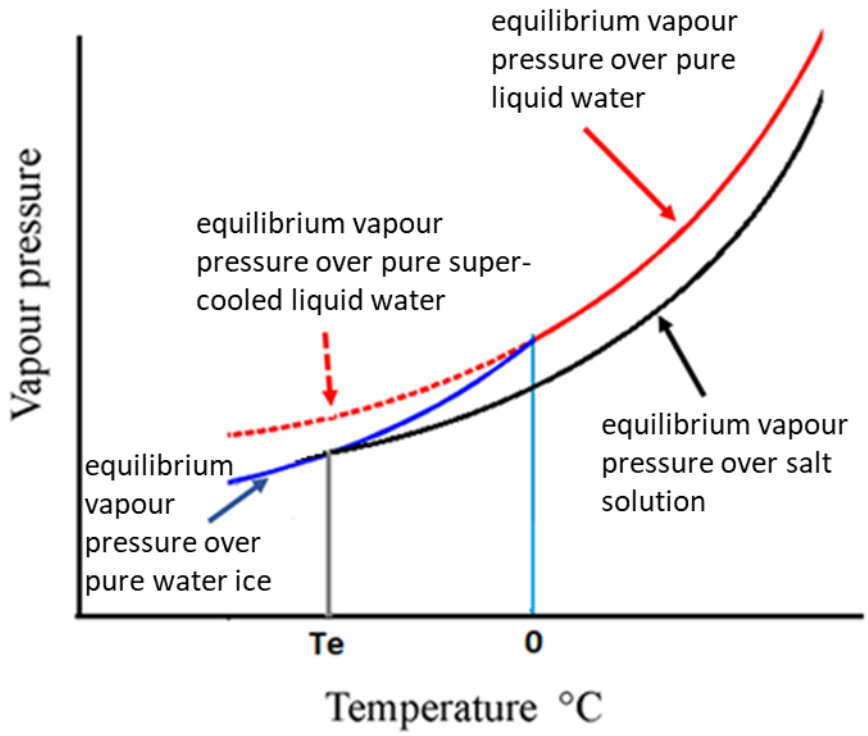

Figure 2.9. Diagram demonstrating the temperature equilibrium between pure liquid water and water ice and aqueous salt solution and water ice.

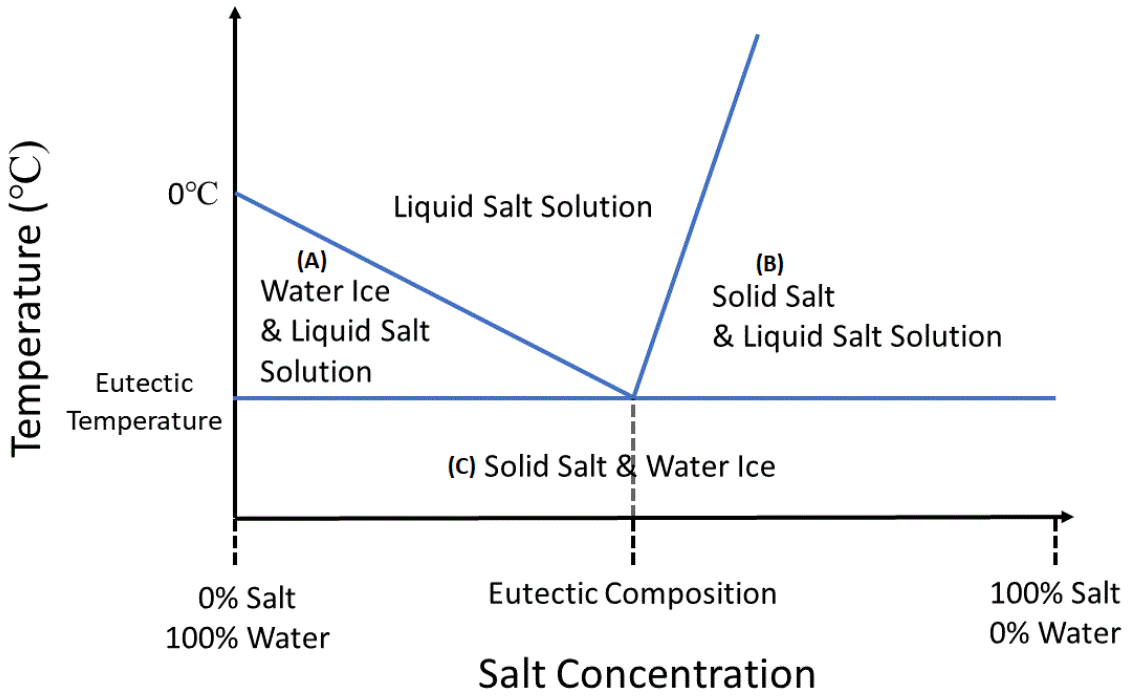

Figure 2.10. Eutectic phase diagram for a typical inorganic salt solution.

2.10 Perchlorate on Mars

Perchlorate salts are highly deliquescent chemical compounds that are composed of perchlorate ions (ClO_4^-) [*Urbansky,* 1998]. Solid perchlorates form neutrally charged salt molecules by ionically bonding with positively charged cations such as magnesium (Mg^{2+}), calcium (Ca^{2+}), and sodium (Na^+). Perchlorates often occur as hydrated minerals that contain chemically bound water within their crystalline mineral structure, but can also be stable in the anhydrous phase [*Gough et al.,* 2011]. Figure 2.11 shows a diagram of the basic chemical structure of magnesium perchlorate salt $Mg(ClO_4)_2$.

Perchlorate was first identified on Mars by the Wet Chemistry Laboratory (WCL) instrument on board the Mars Phoenix lander [*Hecht et al.,* 2009]. The WCL measured the abundance of inorganic anions and cations in scooped samples of surface regolith and identified ClO_4^- at quantities of ~0.6% by weight at the north polar Phoenix site [*Hecht et al.,* 2009]. Perchlorate was more recently detected in the surface regolith at equatorial Gale Crater by the Sample Analysis at Mars (SAM) instrument on the Mars Science Laboratory Curiosity rover [*Glavin et al*., 2013]. SAM consists of a mass spectrometer, a gas chromatograph, and a tunable laser spectrometer and measures the temperature at which different gases are evolved as scooped samples of surface regolith material are heated. All the samples analyzed by SAM have featured the release of oxygen between 100˚C and 600˚C which is consistent with oxychlorine molecules such as perchlorate. Perchlorate was also found within the Mars meteorite EETA79001 and it was concluded that this perchlorate originated on Mars [*Kounaves et al.,* 2014]. These multiple detections suggest that perchlorates are likely to be globally distributed on the surface of Mars.

While landed missions have either directly or indirectly detected the presence of perchlorate ions in the Martian regolith, the parent salt assemblages (the combination of perchlorate anion and metal cation as well as the hydration state) are still unknown. Attempting to constrain the exact type of perchlorate on Mars is important as different perchlorate salts will deliquesce at unique relative humidity values and will experience different freezing point depressions when in solution. To identify the parent salts at the Phoenix site, different known soil mixtures where analyzed using a laboratory version of the WCL instrument that was identical to the flight instrument [*Kounaves et al.,* 2014]. These measurements were then compared to the Phoenix WCL data and it was concluded that the soil samples measured at the Phoenix site contained a combination of calcium perchlorate $Ca(ClO_4)_2$ and magnesium perchlorate $Mg(ClO_4)_2$ at a ratio of approximately 3:2. The hydration state of the salts could not be identified using this method. In a different study, chemical modelling was applied, and it was concluded that the most abundant perchlorate salt at the Phoenix site was magnesium perchlorate hexahydrate $Mg(ClO_4)_2 \cdot 6H_2O$ with smaller quantities of sodium perchlorate dihydrate $NaClO_4 \cdot 2H_2O$ and anhydrous potassium perchlorate $KClO_4$ also present [*Toner at al.* 2014]. At Gale Crater, the pattern of O_2 and H_2O release from regolith samples heated by the SAM instrument has revealed that the most probable parent perchlorate salts at that site are hydrated forms of calcium perchlorate and magnesium perchlorate [*Archer et al.,* 2014].

On Earth, large amounts of perchlorate are artificially produced for use in rocket propellants and fireworks, however their natural occurrence is rare and they are only found in very dry environments such as arid deserts [*Trumpolt et al.,* 2005]. Several potential formation mechanisms have been proposed to explain the presence of

perchlorate on Mars. *Catling et al.* [2010] studied perchlorate formation in the Atacama Desert on Earth and proposed that perchlorate on Mars might be similarly formed through the gas phase oxidation of chlorine volatiles to perchloric acid. Photochemical modelling later demonstrated that the production of perchlorate via this gas phase formation process was likely insufficient to explain the quantities measured on Mars [*Smith et al.*, 2014]. This updated modelling study proposed an alternative gas-solid surface process involving the conversion of chloride to perchlorate. Other experimental work demonstrated that perchlorate can be photochemically produced on chloride bearing minerals without the presence of chlorine gas [*Carrier and Kounaves*, 2015]. In either case, the formation of perchlorate is likely to be an ongoing process which is occurring globally on Mars.

There is significant interest in perchlorates on Mars due to their ability to greatly depress the freezing point of water when in solution, as well as their ability to take up water vapour directly from the atmosphere (deliquescence) [*Chevrier et al.*, 2009]. Figure 2.12 demonstrates the highly deliquescent nature of perchlorate in a series of images taken during a warm summer day at York University in Toronto (25˚C and 65% RH). The sample of magnesium perchlorate hexahydrate rapidly absorbed water vapour from the atmosphere and formed a liquid solution in under 3 hours.

Figure 2.13 shows the eutectic phase diagram for magnesium perchlorate based on a combination of measurements and modelling [*Chevrier et al.*, 2009]. Magnesium perchlorate solution was calculated to have a minimum freezing point (eutectic) temperature of 206 K (-67˚C) at a eutectic concentration of 44% perchlorate by weight. MP4 and MP6 denote the stable hydration states of the perchlorate i.e. magnesium

perchlorate tetrahydrate ($MgClO_4 \bullet 4H_2O$) or magnesium perchlorate hexahydrate ($MgClO_4 \bullet 6H_2O$).

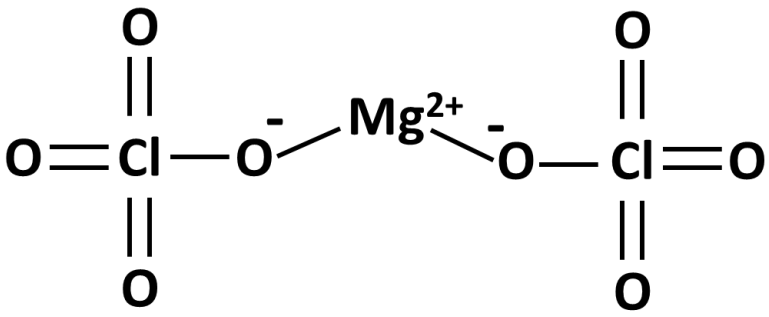

Figure 2.11. Diagram of the basic chemical structure of magnesium perchlorate salt.

Figure 2.12. Images of magnesium perchlorate hexahydrate undergoing deliquescence in ambient Earth conditions at York University. The sample container pictured here had a 1-inch diameter.

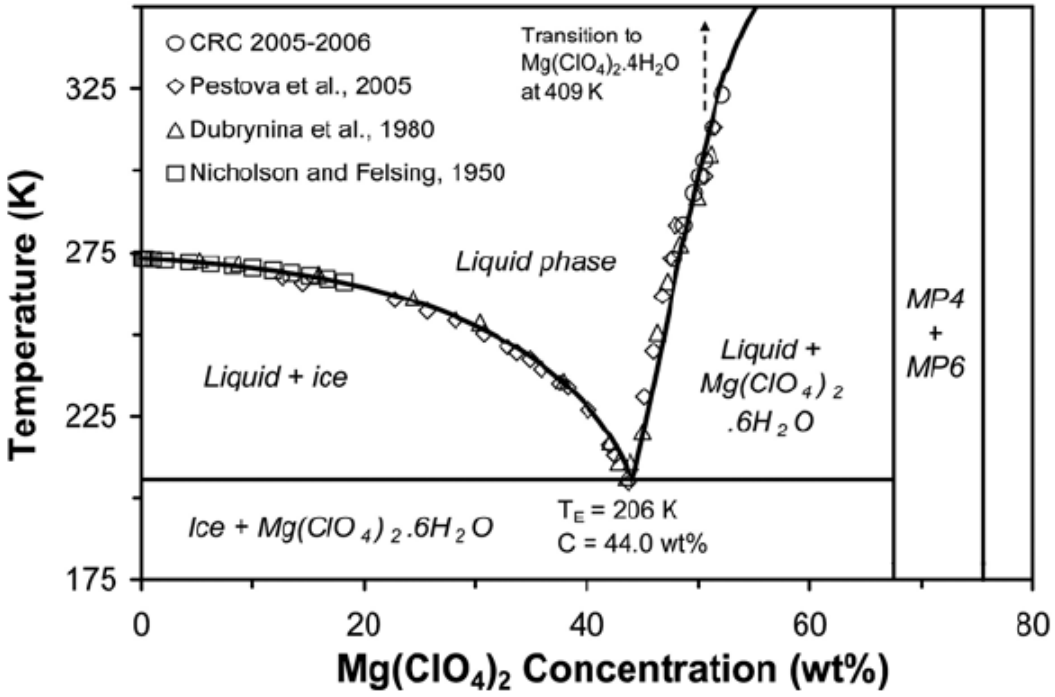

Figure 2.13. Magnesium perchlorate eutectic phase diagram [figure taken from *Chevrier et al.*, 2009].

2.11 Recurring Slope Lineae on Mars

One of the most significant recent discoveries on Mars has been the existence of surface features that have been termed recurring slope lineae (RSL). These are dark streaks that appear on steep Martian slopes. These dark, narrow features have been detected in images taken by the High Resolution Imaging Science Experiment camera (HiRISE) on board the Mars Reconnaissance Orbiter (MRO). RSL have a typical width of 0.5 to 5 m, are up to 40% darker than the surrounding surface material, and appear on slopes with an inclination of 25° or greater [*McEwen et al.*, 2011]. RSL have been observed to incrementally grow during warm seasons, fade during cold seasons, and reform on a seasonal basis. They have been found to occur at midlatitude and equatorial locations with little spatial connection to one another. Figure 2.14 displays a typical example of RSL streaks that have been imaged by the HiRISE camera [*McEwen et al*., 2014]

Recurring Slope Lineae have been interpreted as being a result of flowing (or seeping) liquid water [*Chevrier and Rivera-Valentin*, 2012], however a significant number of RSL are found near topographical highs, making groundwater or ice-based formation mechanisms very unlikely [*Chojnacki et al.,* 2016]. Orbital reflectance spectra measurements provided by the Compact Reconnaissance Imaging Spectrometer for Mars (CRISM) on MRO have detected the presence of hydrated salts such as magnesium perchlorate, sodium perchlorate, magnesium chlorate and magnesium chloride within several RSL locations [*Ojha et al.,* 2015]. This has led to the theory that RSLs may be the result of liquid salt brine formed through an atmospheric process such as deliquescence. Figure 2.15 shows a map of the global distribution of RSL on Mars that have been either

fully confirmed or partially confirmed [*Rummel et al.,* 2014]. The majority of RSL that have been detected thus far are found in the southern hemisphere of Mars between latitudes of 0°S and 60°S. The south favouring distribution of RSL may reflect topographical differences, as the northern hemisphere of Mars is significantly flatter than the southern hemisphere [*Smith et al.*, 1999].

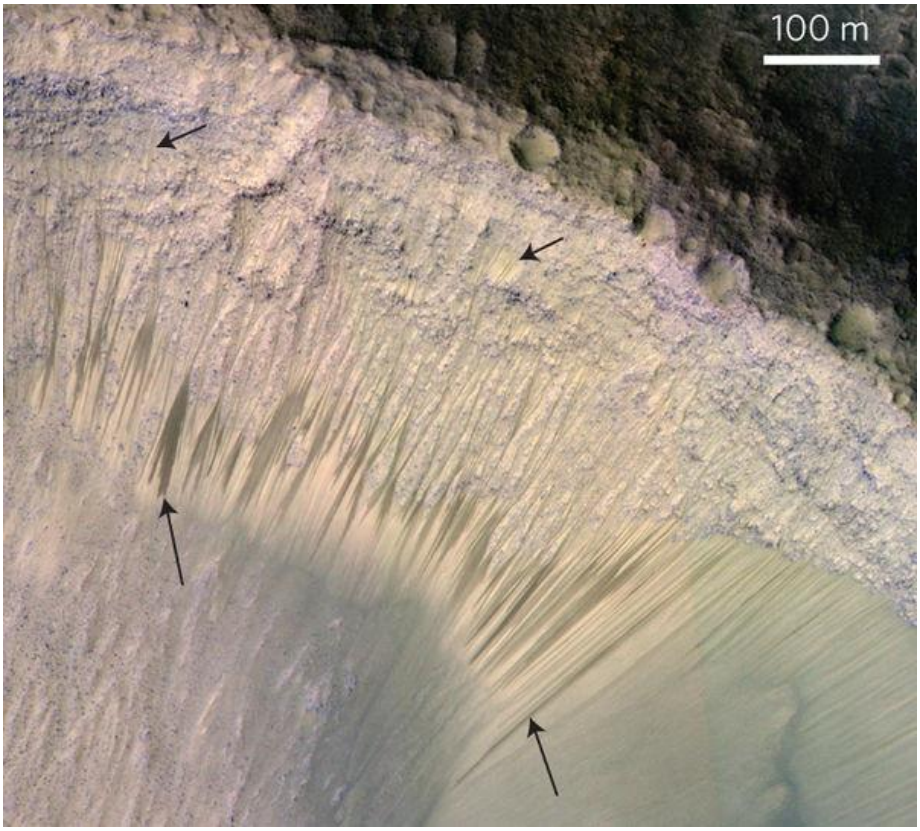

Figure 2.14. Recurring Slope Lineae imaged on the slope of a crater at Melas Chasma on Mars [figure taken from *McEwen et al.,* 2014].

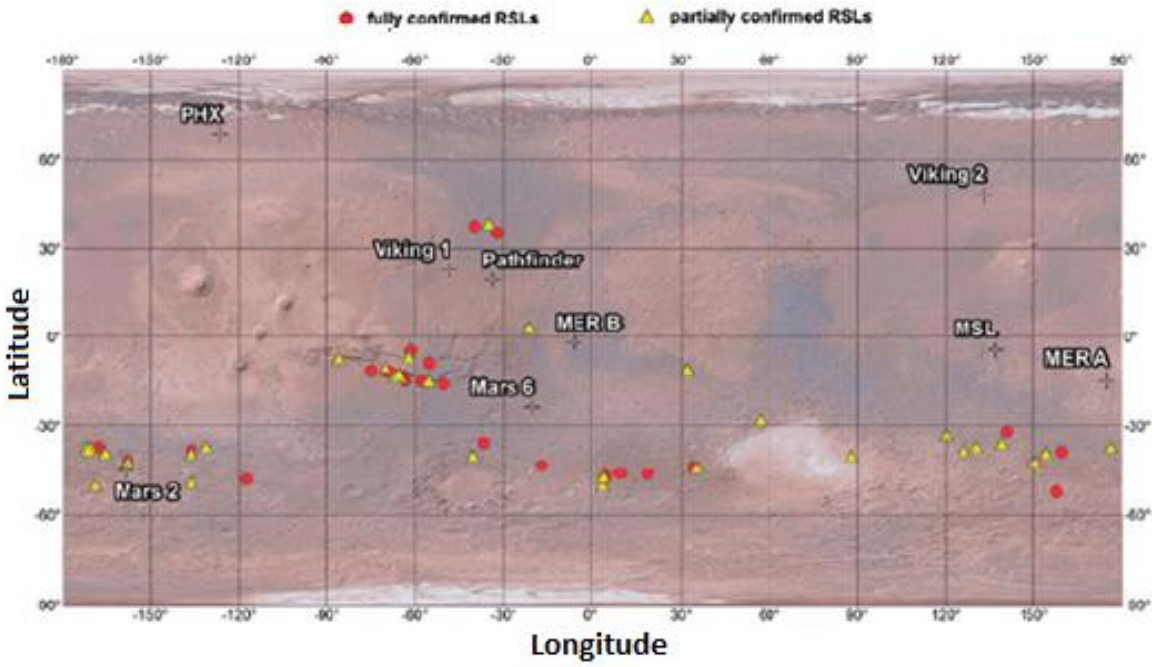

Figure 2.15. Global map of Mars showing the locations of fully confirmed (red) and partially confirmed (yellow) Recurring Slope Lineae sites [figure modified from *Rummel et al.*, 2014].

2.12 Adsorption

Adsorption refers to the adhesion of gaseous or liquid atoms or molecules (the adsorbate) to the surface of a solid (the adsorbent) [*Keller and Staudt*, 2005]. Unlike absorption, which refers to the dissolution of gaseous or liquid molecules in a liquid or solid over a specific range of temperatures and pressures, adsorption is a surface process which may theoretically occur over all temperatures and pressures.

Depending on the nature of the surface forces involved, adsorption may be classified as either physical adsorption (physisorption) or as chemical adsorption

(chemisorption). Physical adsorption involves van der Waals forces such as London dispersion forces and dipole-dipole interactions. These forces are relatively weak and result in the adsorbate molecules being loosely bound to the surface of the adsorbent. During physical adsorption, the adsorbate molecules are not subject to chemical reactions and the process is reversible (desorption) [*Keller and Staudt*, 2005].

The forces involved in physical adsorption always include attractive London dispersion forces and repulsive short-range forces [*Gregg and Sing*, 1982]. London forces arise when fluctuations in the electron distribution in an atom produce a temporary induced dipole moment that results in an electrostatic attraction with neighbouring atoms. The potential energy of the London forces can be expressed as $\varepsilon_D(r) = -Cr^{-6}$, where C is the dispersion constant associated with instantaneous dipole-dipole interactions and r is the distance between the interacting atoms. The short-range repulsive force is a consequence of the penetration between the electron clouds of the interacting atoms and the resulting potential energy can be expressed as $\varepsilon_R(r) = Br^{-12}$, where B is an empirical constant. The values of the constants C and B are dependent on the properties of the interacting atoms.

In addition to the dispersion forces, electrostatic forces will also be involved if either of the adsorbent surface or the adsorbate gas are polar in nature [*Gregg and Sing*, 1982]. Electrostatic forces play a significant role when polar adsorbate molecules such as water are involved. If the solid surface molecules are polar, an electric field will result which will induce a dipole in the adsorbate gas molecules. This interaction energy can be expressed as $\phi_P = -\frac{1}{2}a^2F$, where α is the polarizability of the adsorbate molecule, and F is the field strength at the centre of the molecule. If the adsorbate molecule is polar, an

additional interaction energy will apply. This energy can be expressed as $\phi_{F\mu} = -F\mu cos\theta$, where F is the field strength, μ is the dipole moment of the molecule and θ represents the angle between the axis of the dipole and the field. The overall sum of forces that may be involved during physical adsorption can therefore be expressed as

$$\phi_{TOTAL} = \phi_D + \phi_R + \phi_P + \phi_{F\mu}$$

where ϕ_{TOTAL} is the overall interaction energy between the adsorbate molecule and the adsorbent surface, ϕ_D and ϕ_R correspond to the dispersion force energies, and ϕ_P and $\phi_{F\mu}$ correspond to the electrostatic energies.

Chemisorption involves much stronger forces between the adsorbate molecules and the adsorbent surface [*Ruthven*, 2006]. It is an irreversible process wherein chemical bonds are formed between the adsorbate molecules and the adsorbent surface, resulting in the chemical alteration of the molecules that are involved. Chemisorption is a relatively slow process and results in a single monolayer of adsorbate coverage on the adsorbent surface. Chemisorption generally requires very high temperatures and is unlikely to play a substantial role at the surface of present day Mars, where the average temperature is -60˚C.

Unlike chemisorption, physical adsorption is a relatively rapid process that occurs at low temperatures. Depending on the characteristics of the adsorbate and the adsorbent, physical adsorption may result in monolayer adsorbate coverage, multilayer adsorbate coverage, or pore fluids which fill open pore spaces within the adsorbent structure. Physical adsorption is essentially an instantaneous process and therefore the kinetics are mainly limited by the diffusional transport of the adsorbate to the adsorption site.

The total amount of adsorbate that may adhere to a surface depends on the specific surface area of the solid adsorbent, the temperature of the surface, and the vapour pressure of the adsorbate molecules. Strongly adsorbing substances are generally very porous and feature large specific surface areas with many potential adsorption sites. Physical adsorption is observed to increase in response to either a decrease in the temperature of the adsorbent or an increase in the vapour pressure of the adsorbate molecules in the air (e.g. an increase in relative humidity in both cases). This can be explained by thermodynamic equilibrium considerations. If the vapour pressure of the adsorbed molecules is less than the vapour pressure of the adsorbate molecules in the gas phase, molecules will tend to adhere to the surface until an equilibrium is reached such that the rate of molecules being adsorbed by the surface is equal to the rate of molecules being desorbed from the surface back into the air [*Bolis*, 2013]. A decrease in the temperature of the adsorbed molecules or an increase in the vapour pressure of the molecules in the air will lead to a greater vapour pressure differential and drive further adsorption. At some point, all of the adsorption sites on the adsorbent surface will become occupied with adsorbate molecules and the adsorbent surface will become saturated (a monolayer will be formed). As the monolayer becomes denser, the adsorbed molecules can act as a weaker extension of the solid surface and attract further molecules from the gas phase. This results in adsorbate coverage that is multiple molecules thick (multilayer coverage) [*Gregg and Sing*, 1982]. As the distance from the adsorbent surface increases, the attractive forces decrease until a further increase in the relative humidity will no longer result in further adsorption.

2.13 Porous Minerals and Zeolites

Porous minerals are very effective adsorbents due to their large internal surface areas (specific surface area) and increased adsorption sites [*Rouquerol et al.,* 2013]. Minerals with pore diameters less than 2 nm wide are classified as microporous, while minerals with pore sizes between 2 and 50 nm are termed mesoporous. Porous minerals have unique selectivity properties as they will tend to trap and adsorb molecules with diameters that are smaller than the pore size of the mineral, while rejecting molecules that are larger than the pore size.

Zeolites are crystalline microporous aluminosilicate minerals that are composed of aluminum, silicon and oxygen [*Jha and Singh*, 2016]. The building blocks of zeolites are SiO_4 and AlO_4 tetrahedral units, where the SiO_4 carries a neutral charge while the AlO_4 is negatively charged. To compensate for this negative charge and maintain charge neutrality, zeolites incorporate positively charged cations such as Na^+, K^+, Ca^{2+}, and Mg^{2+} into their interior structure. This results in zeolites having a strong electrostatic field within their internal surface which allows them to strongly attract polar molecules such as water. In addition to this polar attraction, zeolites also feature pore diameters that make them highly selective towards the adsorption of water molecules [*Ruthven*, 2006]. Figure 2.16 shows a diagram of the basic structure of a zeolite mineral. Most naturally occurring zeolites are hydrated minerals that contain chemically bound water within their crystal mineral structure in addition to any loosely bound adsorbed water.

Most of the natural zeolites found on Earth are formed through the alteration of volcanic rocks and ash by fresh or saline ground water [*Erdem et al*., 2004]. Mars has had an extensive history of explosive volcanism [*Werner*, 2009] which would have produced

the minerals necessary for zeolite formation to occur in the presence of liquid water on early Mars. Evidence for zeolites on Mars has been provided by data from the Thermal Emission Spectrometer (TES) instrument on the orbiting Mars Global Surveyor [*Ruff,* 2004] as well the Compact Reconnaissance Imaging Spectrometer for Mars (CRISM) on the Mars Reconnaissance Orbiter (MRO) [*Ehlmann,* 2009].

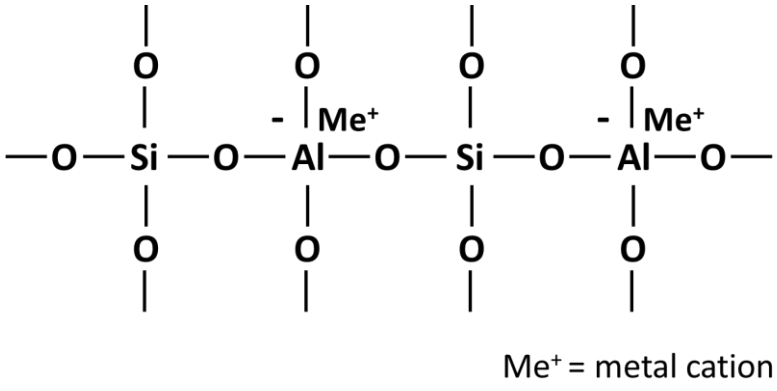

Figure 2.16. Diagram of the basic chemical structure of zeolites.

Chapter Three

Measurement and Analysis

3.1 Introduction

The experimental instrumentation and techniques presented in this chapter have served two purposes. The first was to develop a prototype and the methodology for a remote sensing lidar (light detection and ranging) instrument based on Raman scattering spectroscopy to detect surface-atmosphere water exchange and brine formation from the surface of Mars during a landed mission. This instrument was built on the heritage of the LIDAR instrument for the NASA Phoenix mission [*Whiteway et al*., 2008] that landed on Mars in 2008. The second goal of the project was to experimentally study the mechanisms of water exchange at the surface of Mars. This required the additional design and construction of an environmental chamber which could recreate the thermodynamic conditions and atmospheric composition on Mars. The chamber was optically coupled to the lidar instrument and the processes occurring within the chamber were investigated using Raman spectroscopy. The aim of this work was not to develop a flight ready instrument that meets the size and power requirements of a planetary mission, but rather to determine the overall feasibility of such an instrument while also advancing scientific knowledge through the experimental investigations. Figures 3.1 and 3.2 show a

photograph and schematic diagram of the final experimental setup which includes the Raman lidar and the environmental chamber.

Raman spectroscopy has yet to be applied to planetary exploration outside of Earth, however three separate Raman instruments are planned for upcoming missions. The NASA Mars 2020 rover (scheduled to land on Mars in February 2021) will feature a Raman instrument named SHERLOC (The Scanning Habitable Environments with Raman & Luminescence for Organics & Chemicals) with an excitation wavelength of 248 nm [*Abbey et al.*, 2017], as well as a 532 nm Raman component as part of the SuperCam instrument [*Perez et al.*, 2017]. The ExoMars rover, developed by the European Space Agency (ESA), is scheduled to launch to Mars in 2020 and will also carry a 532 nm Raman instrument named the Raman Laser Spectrometer (RLS) [*Rull et al.*, 2017]. The results of this experimental work will help to guide investigations made during these upcoming missions and will aid in the interpretation of data returned from the Raman instruments.

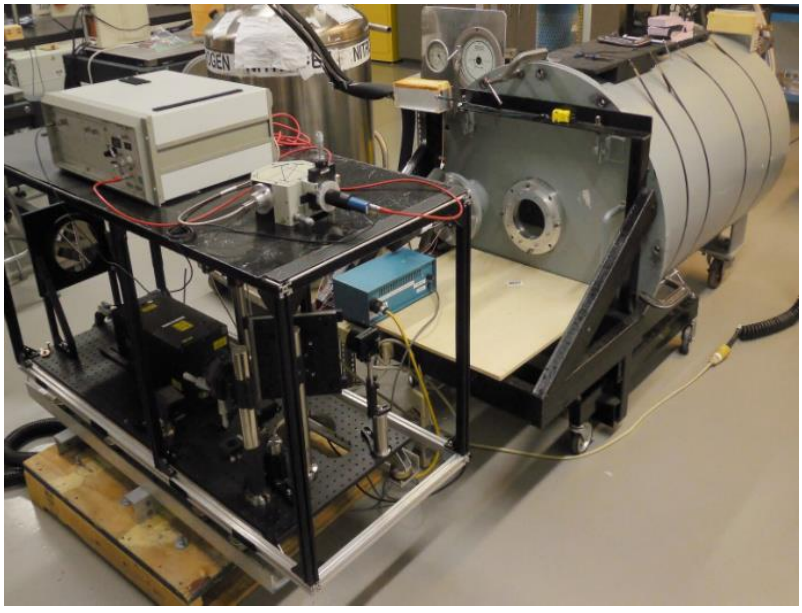

Figure 3.1. Photograph of the Raman lidar instrument and environmental chamber.

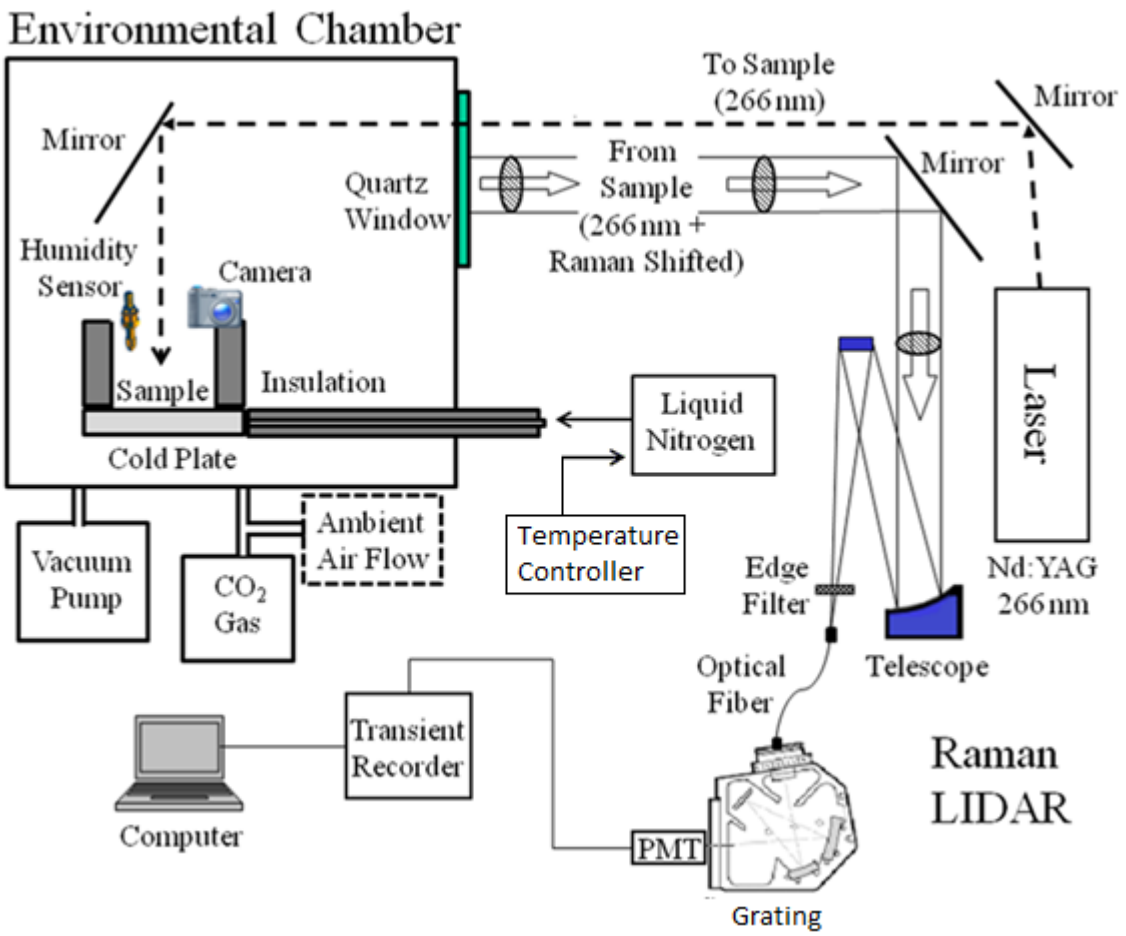

Figure 3.2. Schematic diagram of the experimental setup.

3.2 Raman Scattering Spectroscopy

3.2.1 Background

When a beam of monochromatic light encounters a sample of molecules, the incident light is either absorbed, transmitted, or scattered. Most of the scattered photons have the same wavelength as the incoming light, however a small portion are shifted in wavelength due to the molecular vibrations and rotations of the molecules that make up the sample [*Pelletier,* 1999]. The wavelength altered photons are said to be Raman shifted and the resulting spectrum of shifted light is termed a Raman spectrum. Raman spectra typically consist of several relatively sharp bands (Raman peaks) which are unique to the constituent molecules that make up the sample. This makes Raman spectroscopy an excellent qualitative tool for identifying and discriminating between different molecules. The strength of the peaks in a Raman spectrum are proportional to the concentration of a given molecule within the sample, therefore Raman spectroscopy can also be used to extract quantitative information. Raman spectra can be acquired from stand-off distances without the need to handle or prepare the sample, making it a well-suited technique for planetary exploration missions.

3.2.2 Raman Scattering

A photon may be absorbed by a molecule if the energy of an incident photon matches the energy difference between the ground state and an excited state of the molecule. Molecules can absorb energy and undergo rotational energy transitions when the molecule is excited by microwave or infrared radiation, vibrational transitions when excited by infrared or visible light, and electronic transitions when excited by ultraviolet

light. Unlike absorption, scattering does not require that the energy of the incident radiation match the energy gap between the ground and excited state, but rather occurs when molecules undergo transitions from the ground state to a 'virtual' state. This virtual state is not a quantum-mechanical stationary energy level, but instead represents a distortion of the electron cloud around the nuclei of the molecule. The virtual state is not stable, and the molecule immediately returns to a lower energy state by emitting a photon. The degree to which the electron cloud of the molecule can be distorted by the oscillating electric field of the incident light is referred to as the electron cloud polarizability.

If the scattering involves only the electron cloud distortion of the molecule, the energy of the emitted photon will be the same as the incident photons. This scattering does not involve a transfer of energy between the incident photons and the molecule and is termed elastic Rayleigh scattering. When nuclear motion is also involved in the scattering process, energy is exchanged between the molecule and the incident photons and the scattered photon will have an energy that differs from the incident photons [*Smith and Dent*, 2013]. This is termed inelastic Raman scattering. If the molecule transitions from the virtual state to a higher vibrational level than it began in, the scattered photon will have less energy than the incident photons and will be shifted to a longer wavelength. This is known as Stokes shifted Raman scattering. If the molecule returns to a lower vibrational level than it began in, the scattered photon will have more energy than the incident photons and will be shifted to a shorter wavelength. This is termed anti-Stokes Raman scattering. Only about 1 in 10^6 to 10^8 of the incident photons are Raman scattered, making it a relatively weak process when compared to the much more common Rayleigh scattering case. Figure 3.3 shows an energy level diagram of the elastic Rayleigh and

inelastic Raman scattering processes. At temperatures typical of Earth and Mars, most molecules will initially occupy the lowest vibrational energy level according to the Boltzmann distribution. Therefore, the Stokes scattering scenario will always dominate over the anti-Stokes case and the longer wavelength (lower energy) Stokes shifted light is usually measured in a Raman spectrum.

Raman spectra are plotted with the intensity of Raman scattering displayed on the y-axis and the wavelength, representing a shift in energy, on the x-axis. In order to normalize the Raman spectra for comparison with spectra that have been acquired using different excitation wavelengths, the x-axis is typically displayed in units of wavenumber (cm^{-1}) where the wavenumber shift is calculated as:

$$\Delta\omega\ (cm^{-1}) = \left(\frac{1}{\lambda_{0(nm)}} - \frac{1}{\lambda_{1(nm)}}\right) \times \left(10^7 \frac{nm}{cm}\right) \qquad (3.1)$$

where $\Delta\omega\ (cm^{-1})$ is the Raman shift in cm^{-1}, $\lambda_{0(nm)}$ is the laser excitation wavelength in nm and $\lambda_{1(nm)}$ is the Raman shifted wavelength in nm.

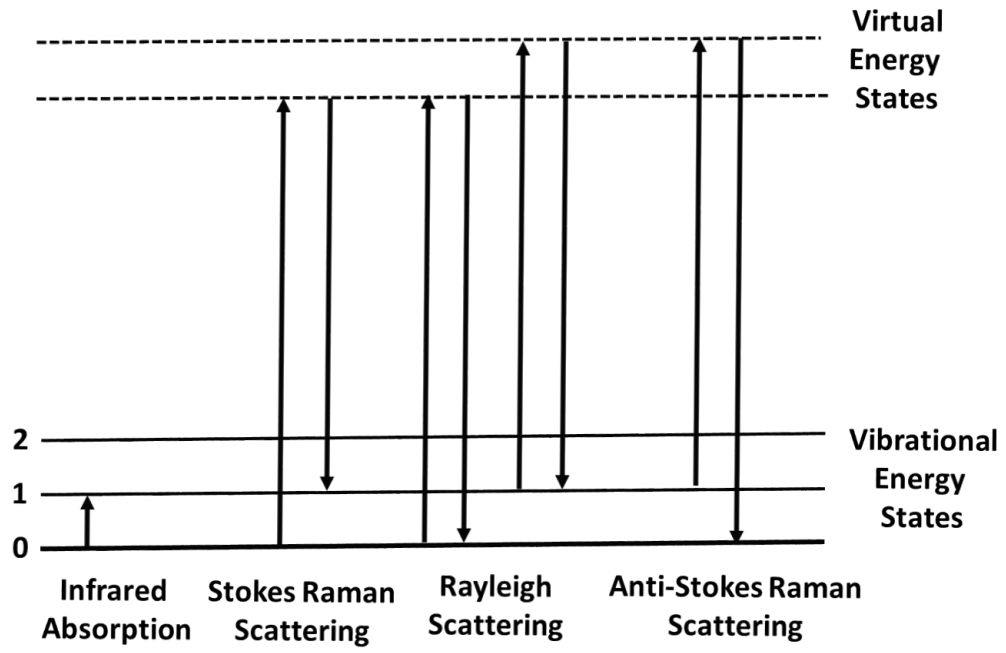

Figure 3.3. Energy level diagram demonstrating the processes of infrared absorption, Rayleigh scattering, Stokes Raman scattering, and anti-Stokes Raman scattering.

3.2.3 The O-H Raman Shifted Region

The stretching vibrational modes of water (H_2O) in the 2900-3800 cm^{-1} Raman shifted spectral range represent the main advantage to using Raman spectroscopy for the study of water. The Raman spectrum of water is a complex band composed of contributions from the symmetrical and asymmetrical stretching vibrations of the O-H bonds and intra- and intermolecular couplings between the water molecules [*Eisenberg and Kauzmann*, 2004]. The O–H stretching vibrations of water are strongly dependent on the hydrogen bond strength and this results in different phases of water having distinct

Raman spectra. Increases in the strength of hydrogen bonding (e.g. during the phase change from liquid water to water ice) typically results in the O-H stretch vibrational modes being shifted to lower wavenumber. Figure 3.4 shows the three modes of vibration for a water molecule.

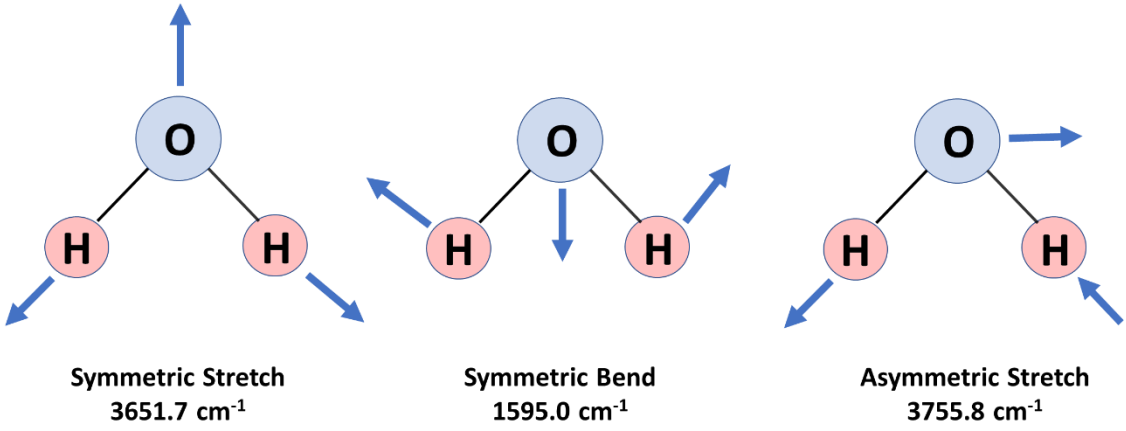

Figure 3.4. Diagram of the three modes of vibration for a water (H_2O) molecule and their theoretical band locations.

3.3 Raman Lidar

The first step in the project was the development of a Raman lidar instrument. The design of this instrument differs from typical Raman spectrometers in that it has the capability to perform range resolved atmospheric measurements as well as near-range surface measurements.

A lidar (light detection and ranging) system operates by emitting pulses of laser light into the atmosphere and detecting and recording the light that is scattered back to the instrument as a function of time. The speed of light is then used to covert the time resolved signal to distance. All lidar systems are composed of three main components: a transmitter, a receiver, and detection electronics. The acquisition of Raman scattering spectra also requires a means for suppressing the much stronger elastic backscattered light and for separating the collected light into its spectral components. This section provides an overview of the Raman lidar system and the method of operation.

3.3.1 Transmitter

The Raman lidar transmitter was based on a Nd:YAG laser (Quantel CFR-800) with a fundamental wavelength of 1064 nm, a repetition rate of 20 Hz, and a pulse duration of 10 ns. Crystals for 4^{th} harmonic generation were employed to produce the desired ultraviolet output wavelength of 266 nm. Figure 3.5 shows a photograph of the breadboard mounted Raman lidar components along with the superimposed path of the laser beam. 1-inch dielectric laser line mirrors (Y4 mirrors from CVI Laser Optics) were used to direct the 266-nm light pulses towards a 2-inch beam steering mirror. The steering mirror was housed in a gimbal mount which allowed the outgoing laser beam to be precisely directed

towards the target. The diameter of the laser beam was approximately 1 cm at the sample.

The use of the 266-nm ultraviolet excitation wavelength was primarily motivated by the higher sensitivity of the available photomultiplier detectors to this wavelength region, however this choice also provided two main advantages over longer wavelength options. In the case of both Raman and Rayleigh scattering, the intensity the scattered light is inversely proportional to the fourth power of the wavelength, therefore UV light generally produces a much stronger Raman signal (e.g. a factor of 16 increase in Raman scattering versus 532 nm visible excitation). A second benefit is that the Raman spectrum produced by 266 nm excitation lies entirely in the UV region and largely avoids the potential interference from fluorescence, which tends to occur in the visible spectral region.

The output laser pulse energy was controlled and was chosen to maximize the Raman scattering signal while avoiding heating of the sample material. Minimizing potential heating effects was vital, as a warming of as little as 1ºC to 2ºC could have dramatic effects on determining the onset of deliquescence or brine freezing. To ensure that the samples were not being heated by the laser, different sample materials were probed with varying levels of laser power. While the sample was irradiated by the laser beam, the temperature of the sample was simultaneously measured using a non-contact infrared temperature sensor from Etekcity (Lasergrip 630). When the temperature of the sample was observed to increase by more than 0.3ºC upon exposure to the laser, the laser power was reduced. Heating was most significant with the zeolitic chabazite material, which also exhibited the weakest Raman scattering signal. These effects were likely due to some of the incident UV light being absorbed by the sample. The heating experiments

resulted in a laser pulse energy of 15 mJ (300 mW of power) being applied for the magnesium perchlorate experiments presented in Chapter 4, and a laser pulse energy of 10 mJ (200 mW) being chosen for the experiments in Chapter 5 which included chabazite.

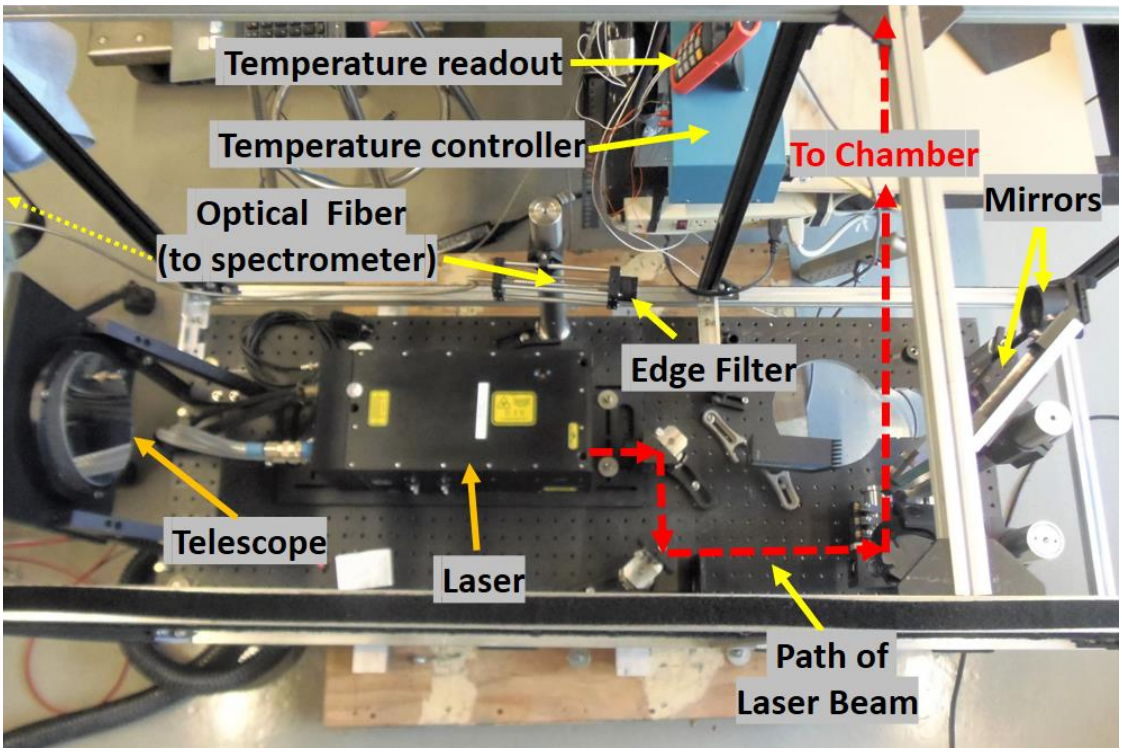

Figure 3.5. Overhead view of the Raman lidar optical arrangement and components. The path of the laser beam towards the target is superimposed in red.

3.3.2 Receiver and Spectrometer

Backscattered light from the target was collected using a 15-cm diameter off-axis parabolic telescope mirror. The light was passed through a 266 nm long-pass interference (edge) filter (Semrock, Inc.) to remove the much more intense elastic backscattered light

and was then focused into a 0.82 mm diameter silica optical fiber bundle. The edge filter was composed of multiple layers of dielectric coatings on a fused silica substrate which produced interference patterns that blocked all radiation at wavelengths less than 268 nm. The fiber cable was custom designed and consisted of 127 optical fibers which were fused at the input end and formatted into a slit line which was 70 µm wide and 8.38 mm long at the output end. The fiber was coupled to an Oriel MS125 grating with a 150-mm focal length, a focal ratio of F/3.7, and a 2400 grooves/mm grating with a 250-nm blaze. The spectrometer was adapted to accept the fiber cable at the input side, with the fiber itself functioning as the entrance slit, and a photomultiplier tube at the focal plane of a lens which was placed at the exit slit. The adjustable exit slit was set to a width of 70 µm to match the width of the fiber slit line.

The spectrometer grating angle was adjusted using a micrometer screw which was joined to the grating. Raman spectra were acquired by sequentially scanning the grating angle to measure the Raman scattering signal at a range of wavelengths. During the acquisition of Raman spectra, the grating was scanned at wavelength intervals of 0.25 nm which corresponded to a wavenumber shift of 35 cm^{-1} near the laser line and 29 cm^{-1} at 3600 cm^{-1} (in the O-H Raman shifted region).

3.3.3 Detection

A photomultiplier tube (PMT) detector generated electrical signals that were recorded using both photon counting and analog to digital conversion. The electronic signal from the PMT was acquired using a transient recorder (Licel) and the output was transferred to a Windows PC. At near ranges, the photon counting signal was found to be

highly sensitive to pickup noise from the laser, thus only the analog signal was used during the chamber experiments.

During the acquisition of Raman spectra, an integration period of 400 laser shots (20 s at 20 Hz) was used to measure the Raman backscatter signal at each wavelength. This integration period was chosen to strike a balance between reducing the statistical uncertainty in the signal while minimizing the time required for scanning and measuring a full Raman spectrum. When measurements were made at a single wavelength over time (e.g. Fig. 4.3), the integration time for each measurement was 3600 laser shots (180 s at 20 Hz).

The contribution from the laser pickup noise to the analog signal was determined by conducting a sequence of twenty 400 laser shot measurements with the receiver optical fiber blocked. The average contribution to the signal was 0.0462 mV, which was less than 10% that of the weakest Raman feature measured during the experiments. The laser noise measurements varied by a maximum of 0.0037 mV, thus the noise appeared as a very small additive contribution to the overall Raman scattering signal.

The raw Raman lidar data consisted of the measured backscattered signal as a function of the laser pulse time of flight (or equivalently range) for a given wavelength. Figure 3.6 shows typical examples of raw signal profiles for a Raman active wavelength (black) and a Raman inactive wavelength (blue). In the near-range chamber configuration, the Raman scattered light was evident in the raw data as a sharp signal peak originating from the sample. The signal measured from distances beyond the sample were averaged and subtracted from the Raman signal to correct for background radiation.

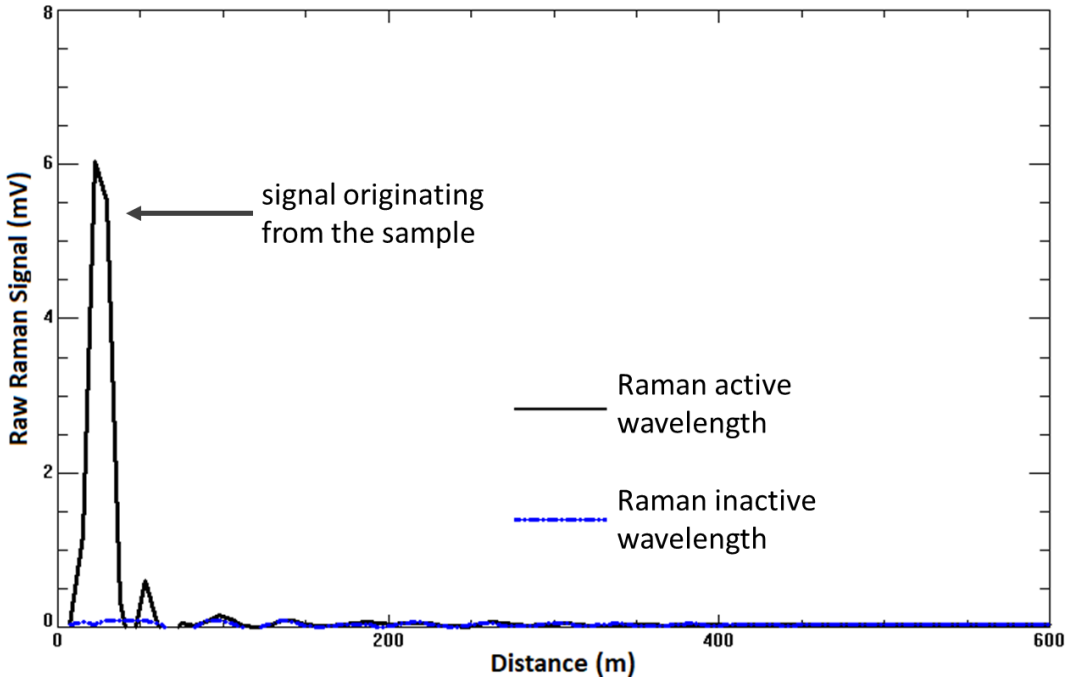

Figure 3.6. Examples of raw signal profiles measured by the Raman lidar.

Raman scattering spectra were created by sequentially compiling the background-corrected Raman scattering signal originating from the sample for each measured wavelength. Calibration of the Raman shift wavenumber axis (x-axis) was performed by detecting the well-known Raman shift of gaseous nitrogen and oxygen from the atmosphere prior to beginning each experiment.

The spectral resolution of the Raman system was determined by several factors including the slit widths, the spectrometer focal length, the groove density of the diffraction grating, the laser linewidth, and the wavelength scanning interval. The spectral bandpass of the system, corresponding to the wavelength distribution passed by the exit slit, was a function of the dispersion of the grating and the width of the entrance and exit

slits [*Workman and Springsteen*, 1998]. The bandpass of the Raman lidar system was calculated by applying the equation $BP = W \times R_d$, where W was the average width of the entrance and exit slits (70 μm) and R_d was the reciprocal dispersion of the spectrometer. For small angles of diffraction, $R_d = {}^{d}/_{(f \times m)}$, where d was the distance between successive grooves on the grating (1/2400 mm/groove), f was the focal length of the spectrometer (150 mm), and m was the order of diffraction (m = 1). Solving for BP yielded a bandpass of 0.20 nm for the Raman lidar system. In practice, the spectral resolution was further limited by the wavelength sampling interval (0.25 nm), the linewidth of the laser, system aberrations, and the natural linewidth of the Raman peaks.

The true instrumental spectral resolution of the Raman lidar was experimentally determined using the *ASTM Standard Guide for Testing the Resolution of a Raman Spectrometer* E2529-06(2014). This method utilized a measured Raman spectrum of calcium carbonate (calcite) to assess the spectral resolution of the Raman system. The Raman spectrum of calcite was measured using the Raman lidar (Fig. 3.7a) and a Gaussian fit was applied to the Raman peak located at a shift of 1085 cm^{-1} (Fig. 3.7b). Gaussian profiles provide an accurate approximation for the Raman spectral peaks of solid materials [*Bradley*, 2007]. The resolution of the instrument was then calculated by applying the following experimentally derived calibration relation which relates the spectral resolution of the Raman spectrometer, $S_{resolution}$, to the measured full width at half maximum of the 1085 cm^{-1} calcite Raman band (B_{w1085}) [*Bowie and Griffiths*, 2003]:

$$B_{w1085}(cm^{-1}) = 1.0209 \times S_{resolution} + 0.684 \qquad (3.2)$$

The full width at half maximum of the 1085 cm^{-1} calcite Raman band (B_{w1085}) was extracted from the Gaussian fit and was found to be 63.3 cm^{-1}. Rearranging Eq. 3.2 and

solving for $S_{resolution}$ yielded a measured spectral resolution of 61.3 cm^{-1} (or 0.46 nm) for the Raman lidar system. This spectral resolution was sufficient for the clear discrimination between the liquid water, water ice, and perchlorate hydrate spectral features found within the O-H Raman shifted region (Fig. 4.2) as well as all of the major Raman peaks in the spectra of magnesium perchlorate hexahydrate (Fig. 4.1), chabazite (Fig 5.1), and quartz sand (Fig 5.2).

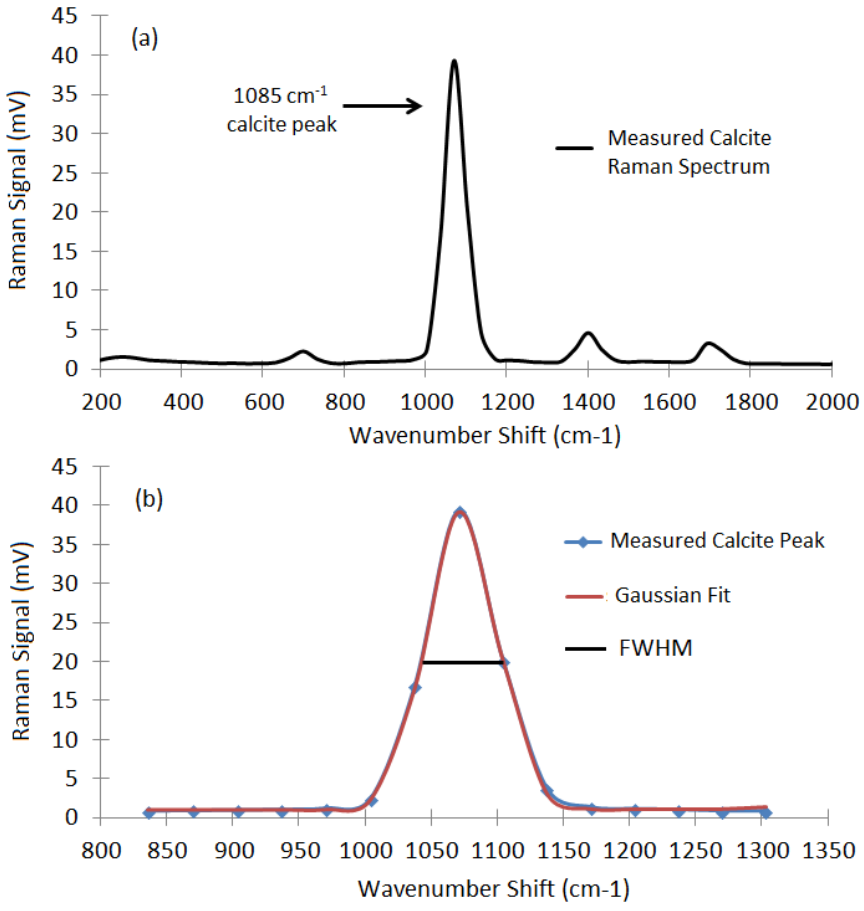

Figure 3.7. (a) Measured Raman spectrum of calcite (calcium carbonate). **(b)** Gaussian fit applied to the measured spectral peak at 1085 cm^{-1} and the calculated full width at half maximum (FWHM).

3.3.4 Detector Linearity and Raman Signal Response to Varying Concentration

An experiment was conducted in order to assess the response of the PMT to varying signal levels and quantities of sample material. Four 1-milliliter solutions of distilled water (H_2O) and magnesium perchlorate hexahydrate ($Mg(ClO_4)_2 \bullet 6H_2O$) were prepared with concentrations of 0% (pure water), 30%, 60%, and 90% $Mg(ClO_4)_2 \bullet 6H_2O$ by weight. In each case, the Raman scattering signal was measured at Raman shifts of 940 cm^{-1}, 3450 cm^{-1}, and 2000 cm^{-1} which corresponded to the strongest Raman peak of the perchlorate ion, the strongest point in the liquid water O-H Raman spectrum, and a spectral region that was Raman inactive. Figure 3.8 displays the results of this experiment. As expected, the Raman signal from the inactive Raman region at 2000 cm^{-1} experienced no changes with varying perchlorate concentration. In the perchlorate ion case, the signal exhibited a linear response to changes in perchlorate concentration. The liquid water signal also experienced a linear increase in the Raman signal as the chemically bound water of hydration within the perchlorate salt crystalline structure dissolved and contributed to the total amount of liquid water. The percentage by mass of the water in $Mg(ClO_4)_2 \bullet 6H_2O$ was calculated to be 33% by dividing the mass of water in one mole of $Mg(ClO_4)_2 \bullet 6H_2O$ by the total molar mass. Thus, the hexahydrate contributed an additional 0.1 ml of water in the 30% concentration case, 0.2 ml at 60% concentration, and 0.3 ml at 90% concentration. These experiments demonstrated that changes in the Raman scattering signal are directly proportional to relative changes in sample concentration e.g. in the quantity of water taken up by surface material such as perchlorate or zeolites.

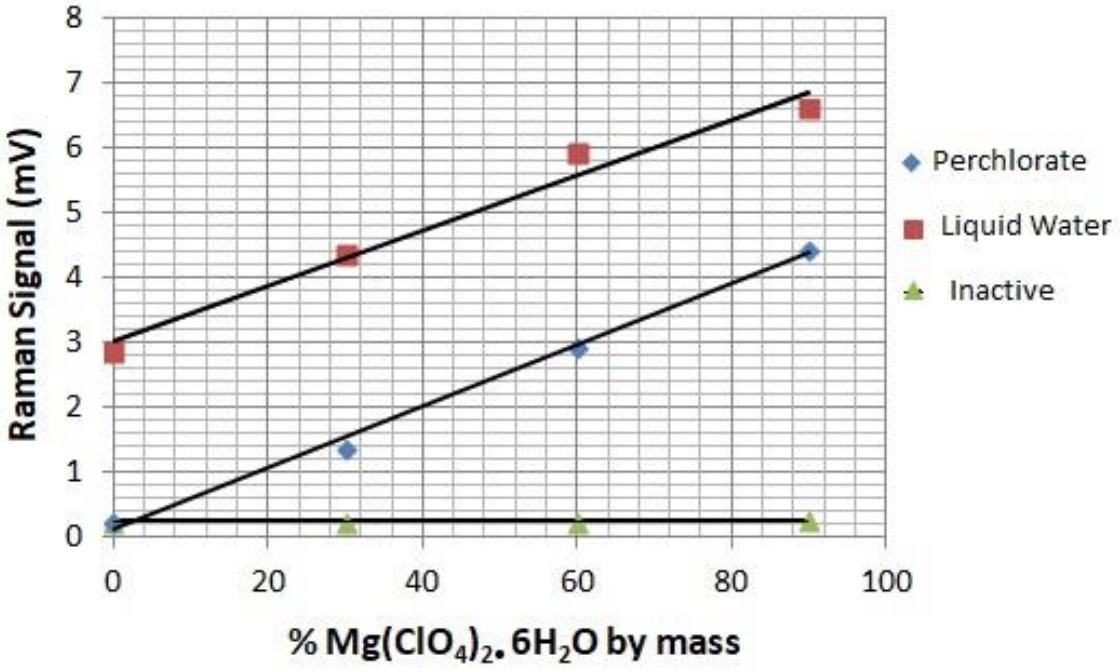

Figure 3.8. Plot showing the Raman signal response to varying concentrations of magnesium perchlorate hexahydrate in solution.

3.3.5 Uncertainty in the Measured Signal

When an incoming photon interacts with the photocathode of a photomultiplier tube, an electron is emitted through the photoelectric effect. The resulting photoelectron is then electrostatically accelerated and focused on to a series of electrodes called dynodes which greatly multiply the number of electrons through the process of secondary emission. The large number of electrons produced through this cascade process are then collected on an anode and the resulting electron current is passed to an operational amplifier and converted to a measured voltage.

Even if the radiation incident on the photomultiplier tube has a constant intensity, the number of photons striking the photocathode per unit time is fundamentally uncertain

due to the quantum nature of light. The number of photons arriving per unit time can be treated as independent, random events and follow a Poisson distribution. The corresponding number of photoelectrons emitted by the PMT photocathode per unit time is also Poisson distributed [*Liu et al.*, 2006] and it is this statistical variation in the number of electrons emitted per unit time (prior to amplification in the PMT dynode chain) that results in the uncertainty in the measured signal. For a Poisson process, the standard deviation of a measurement is equal to the square root of the mean count [*Bevington and Robinson*, 1993].

In the case of the analog data acquisition mode used during the experiments in this dissertation, the uncertainty was computed by first converting the measured voltage, V, to a value of current using $I_0 = {}^{V}/_{(R \times G)}$, where I_0 was the signal current produced by the incident light at the photocathode of the PMT, $R = 50\Omega$ was the op-amp feedback resistance, and $G = 5.5 \times 10^5$ was the gain of the PMT. The signal to noise ratio was then calculated as $SNR_{shot\ noise} = {}^{I_0}\Big/\sqrt{2e\ I_0\ \Delta f\ \#shots}$, where $e = 1.6 \times 10^{-19} C$ was the electron charge, $\Delta f = 20\ MHz$ was the bandwidth of the measurement system, and $\#shots$ was the number of laser pulses in a given measurement [*Hamamatsu*, 1998]. Lastly, the error in the voltage measurement was computed as $V_{error} = {}^{V}/_{SNR_{shot\ noise}}$. In the measurements displayed in this dissertation, the shot noise contribution was smaller than the size of the plotted data points e.g. for the results shown in Fig. 4.3, a measured Raman signal of 1 mV had an associated uncertainty of 0.01 mV.

3.3.6 Earth Atmosphere Testing of the Lidar System

In order to test the instrumental performance, the Raman lidar was initially operated in a vertical viewing configuration. This mode of operation was capable of performing range-resolved atmospheric measurements. Figure 3.9a shows a typical 10 minute-averaged vertical profile of elastic backscatter from the atmosphere (266.0 nm) measured by the Raman lidar above York University in Toronto. The y-axis shows the height above the system (expressed in km) and the x-axis displays the measured backscatter signal in terms of photons counted per second. The enhancement in the backscatter signal between 4.0 and 5.5 km indicates the presence of a cloud layer. For comparison, figure 3.9b shows a 10-minute averaged vertical profile of inelastic Raman backscatter from atmospheric nitrogen (283.6 nm).

Figure 3.10 displays the spectrum of vertically integrated Raman-shifted backscatter from the atmosphere that was measured on July 20, 2012 above York University in Toronto, Canada. This graph shows the measured Raman signal (expressed in photons counted per second) as a function of wavelength (nm). For comparison, the x-axis is also shown in terms of the wavenumber Raman shift (cm^{-1}). Raman peaks were observed at 277.5 nm (a Raman shift of 1556 cm^{-1}), 283.6 nm (2331 cm^{-1}), and 294.7 nm (3657 cm^{-1}), indicating the presence of atmospheric oxygen, nitrogen, and water vapour respectively [*Inaba and Kobayasi*, 1972]. This figure demonstrates both the qualitative as well as quantitative nature of the Raman technique. The unique Raman peak locations allowed for the identification of the molecular constituents in the atmosphere, while the intensity of each peak was proportional to the concentration of each constituent in the air. Table 3.1 shows the relative molecular composition of the atmosphere of Earth, as well

the theoretically calculated shift that results from Raman scattering by each molecule, expressed in both wavelength (nm) and wavenumber shift (cm^{-1}). For simplicity, the x-axis of the Raman spectra presented in the following chapters of this dissertation are expressed only in terms of the wavenumber shift (cm^{-1}).

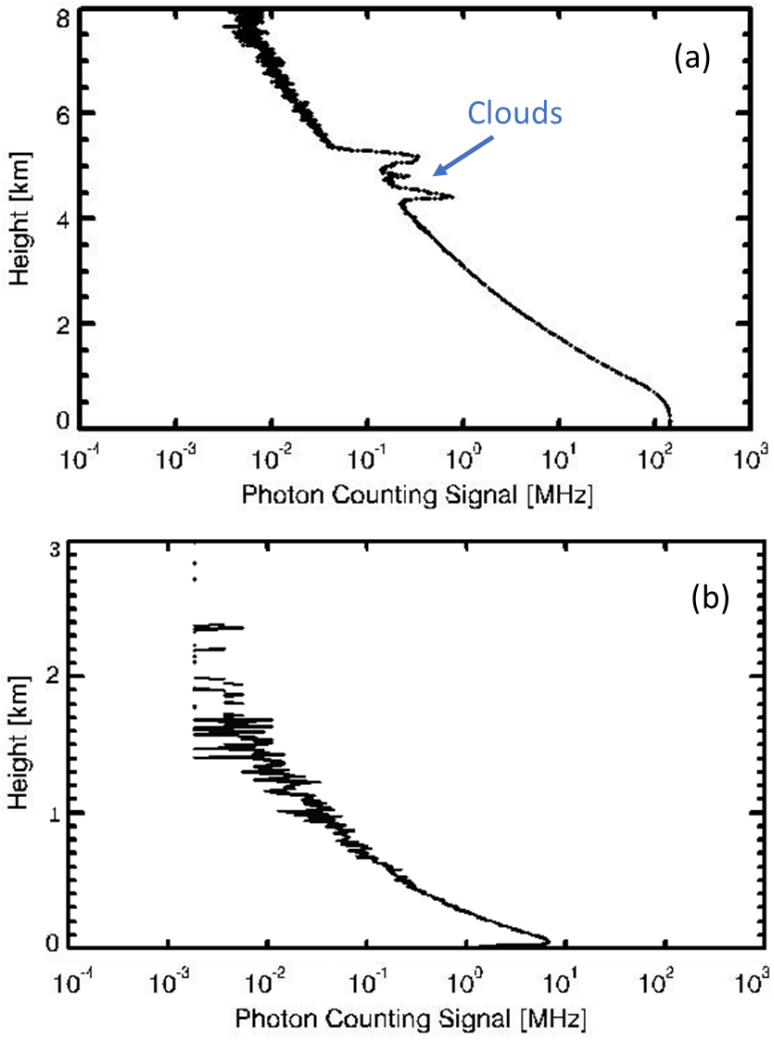

Figure 3.9. 10-minute averaged vertical profiles measured by the Raman lidar above York University in Toronto, Canada of **(a)** elastic atmospheric backscatter and **(b)** Raman-shifted backscatter from atmospheric nitrogen.

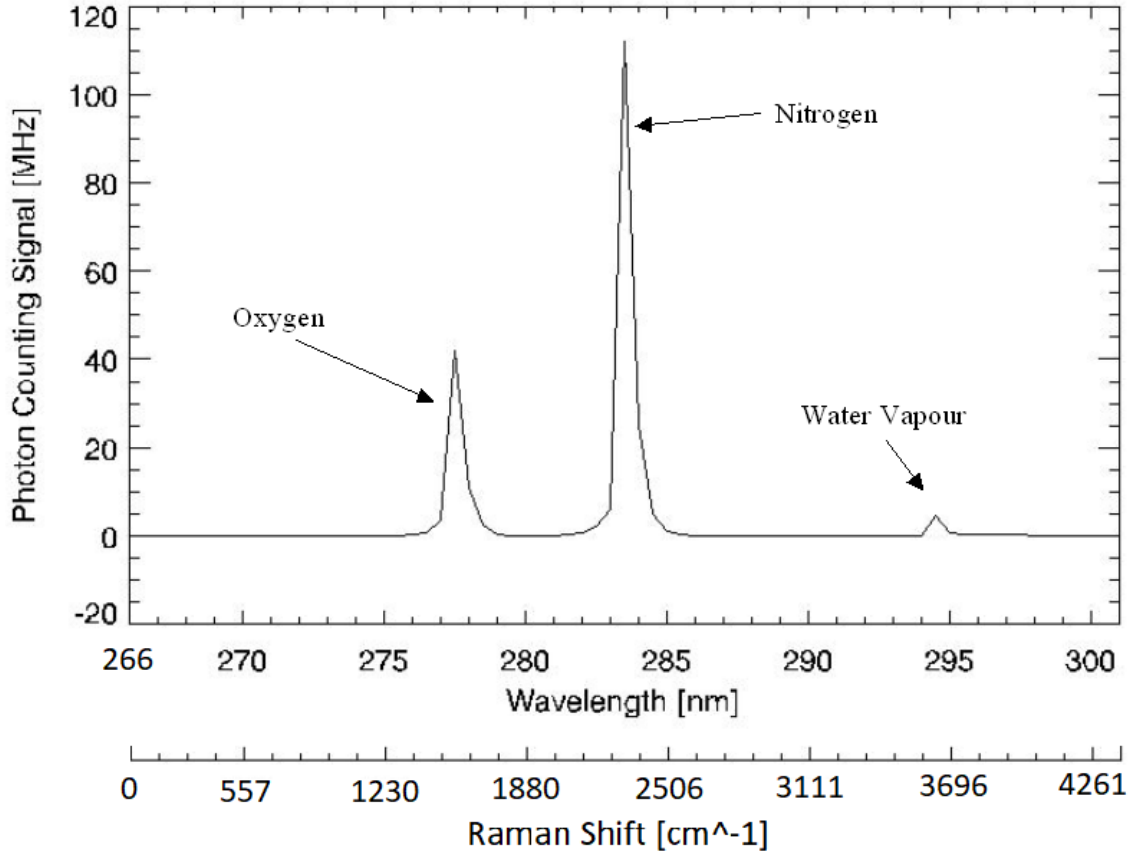

Figure 3.10. Spectrum of Raman-shifted atmospheric backscatter measured on July 20, 2012.

Molecule	Raman Shift (wavenumber)	Expected Return Wavelength (266 nm output)	Atmospheric Composition
Nitrogen	2330.7 cm^{-1}	283.6 nm	78%
Oxygen	1556.4 cm^{-1}	277.5 nm	21%
Water Vapour	3657.0 cm^{-1}	294.7 nm	Variable 0% to 4%

Table 3.1. Expected Raman shift and concentration of the molecular constituents in the Earth atmosphere.

3.4 Environmental Chamber

An environmental chamber was developed to recreate the thermodynamic conditions and atmospheric composition found at the surface of Mars. Figure 3.11 shows a photograph of the lidar and environmental chamber orientation in the lab. The chamber featured a 6-inch diameter quartz window which allowed the ultraviolet laser light from the Raman lidar to enter the chamber and probe a sample of Mars surface material simulant which was placed on a temperature-controlled sample plate. The main components of the chamber are documented in the following sections.

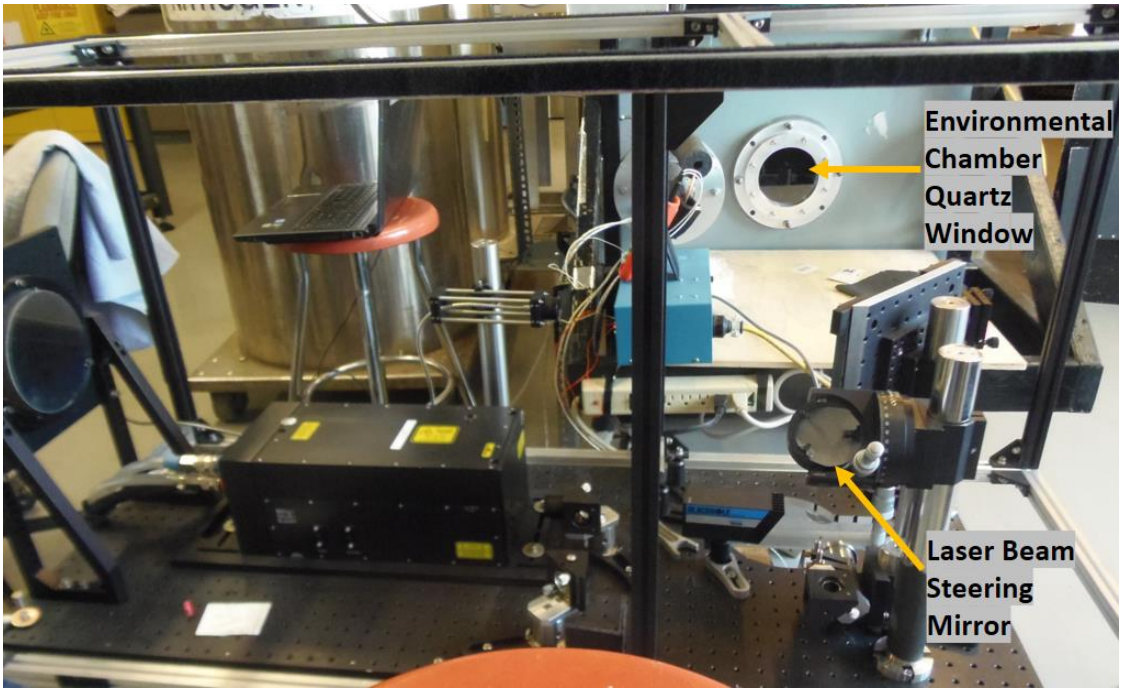

Figure 3.11. Side view of the Raman lidar demonstrating the geometric orientation with respect to the environmental chamber window.

3.4.1 Temperature Measurements and Control

The sample material was placed on an aluminum sample plate which measured 6-inches by 6-inches by 3-inches (Fig. 3.12). The sample plate was in direct thermal contact with a custom made cold plate that consisted of 0.25-inch copper tubing tightly fastened between two 6-inch by 6-inch plates of aluminum sheet metal. Gas-tight tube fittings (Swagelok) were used to run the copper tubing from the cold plate to a solenoid valve located outside the chamber. The sample plate was insulated with extruded polystyrene, the copper tubing was insulated with polyethylene pipe insulation and all connection points were tightly bound with polyethylene insulation tape. These insulating materials provided a water vapour diffusion barrier and prevented thermal transfer from the liquid nitrogen plumbing to the inside of the chamber. This ensured that the sample plate was the coldest surface inside the chamber and prevented water vapour from condensing on any locations other than the sample plate. The insulated cold plate and sample plate assembly was tightly packed into the base of a mirror mount which also housed a 20-cm by 20-cm mirror that was angled at 45º to the surface of the sample plate. This mirror was in alignment with the chamber window and served the dual purpose of directing the incoming laser beam down to the sample and redirecting the scattered light back out to the lidar instrument.

Temperature measurements were performed using 3-wire platinum resistance temperature detectors (RTDs) (Omega model #RTD-SA1) which were fixed to the surface of the sample plate (Fig. 3.13). RTDs operate by exploiting the fact that pure metals experience a well known, repeatable change in resistance at different temperatures. An excitation current was supplied to the platinum RTD element which was in direct contact

with the sample plate, the voltage was measured, and the resistance was obtained and converted to a value of temperature. The supply of excitation current, the voltage measurement, and the temperature conversion were all handled automatically using a handheld RTD input thermometer (Omega model #HH804). The 3-wire configuration allowed for the resistance of the lead wires to be subtracted for increased accuracy, resulting in a quoted RTD accuracy of ±0.15ºC at 0ºC and ±0.35ºC at -100ºC. The RTDs were calibrated by ensuring that the temperature at which a thin layer of distilled water ice was observed to melt was 0ºC. Two RTDs were fixed to the sample plate to provide surface temperature measurements, with one mounted on either side of the sample material (Fig. 3.13).

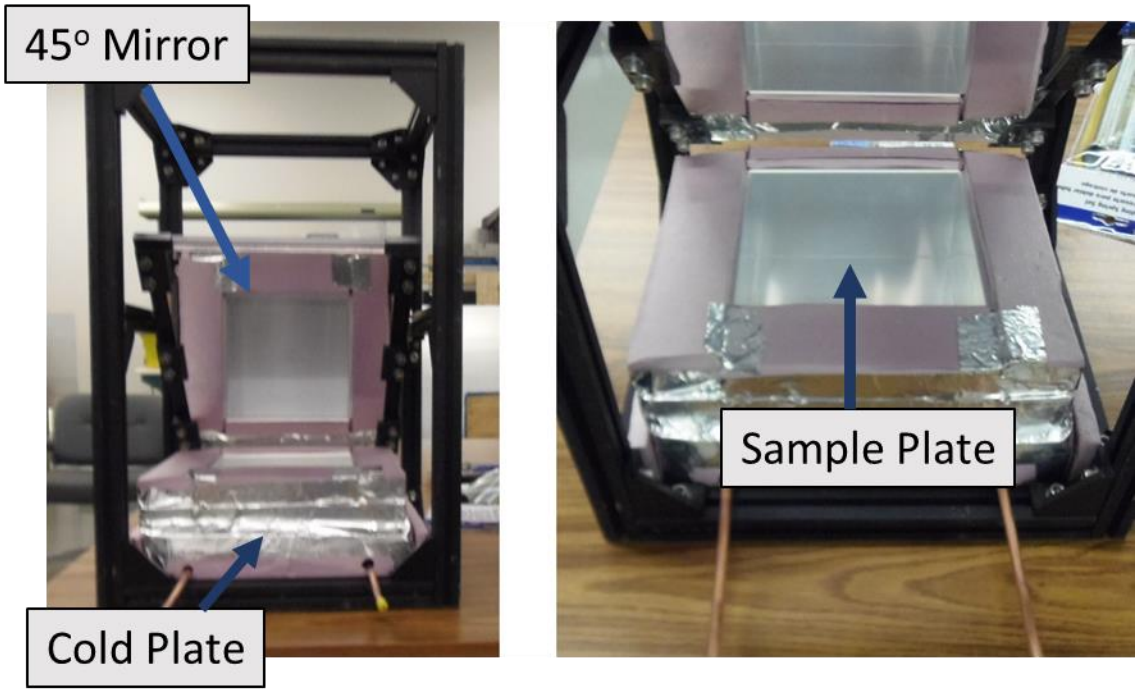

Figure 3.12. Photograph of the insulated cold plate and sample plate housed within the mirror mount.

Control of the sample plate temperature was achieved using liquid nitrogen and employed a cyogenic dewar tank, an RTD, a proportional–integral–derivative (PID) controller (Love Controls 1600 series), and a solenoid valve. Figure 3.14 shows a diagram of the temperature control feedback loop. Temperature control was initiated when the desired setpoint temperature of the sample plate (corresponding to the resistance of the RTD) was entered into the PID controller. The PID controller regulated the flow of liquid nitrogen to the sample plate (via the solenoid valve) and aimed to minimize the difference (or error) between the user selected setpoint temperature and the true temperature of the sample plate which was measured by the feedback RTD (Fig. 3.13). The PID controller used a combination of proportional, integral, and derivative control to reduce temperature fluctuations and overshooting in order to smoothly approach the setpoint temperature. PID control can be expressed mathematically as [*Visioli*, 2006]:

$$u(t) = K_p e(t) + K_i \int_0^t e(t)dt + K_d \frac{d}{dt} e(t) \qquad (3.3)$$

where *u(t)* was the applied correction to the error (in this case proportional to the amount of liquid nitrogen that flowed to the cold plate), *e(t)* was the error (in this case the difference between the setpoint temperature and the true measured temperature), and K_p, K_i, and K_d were the non-negative gain coefficients of the proportional, integral and derivative terms. The proportional term responded to the present error, the integral term to the accumulated error, and the derivative term to the rate of change of the error. The Love Controls 1600 series controller automatically determined the gain coefficients using the standard Ziegler-Nichols PID control algorithm [*Ziegler and Nichols*, 1942]. This is a recursive method in which K_i and K_d were initially set to zero and K_p was gradually increased until the output had stable, repeating oscillations. K_i and K_d were then adjusted

to minimize the amplitude of the oscillations. The correction from the PID controller was applied to an electromechanical solenoid valve in the form of an electric current. The solenoid valve consisted of an electric coil and a movable ferromagnetic core (the plunger). The applied current resulted in a magnetic field which exerted a force on the plunger and opened an orifice, thus allowing liquid nitrogen to flow from the dewar tank to the sample plate.

The temperature control system was designed to automatically supply the optimal amount of liquid nitrogen needed to maintain a particular temperature, however some manual control was also applied to reduce potential overshooting of the temperature. This was necessary due to the inherent limitations of the Ziegler-Nichols method as well as the lag between the time that the liquid nitrogen was released from the dewar tank and the time that it reached the cold plate and reduced the temperature. The temperature of the sample plate experienced a typical cyclical temperature variability of ±0.3ºC when set to a given temperature.

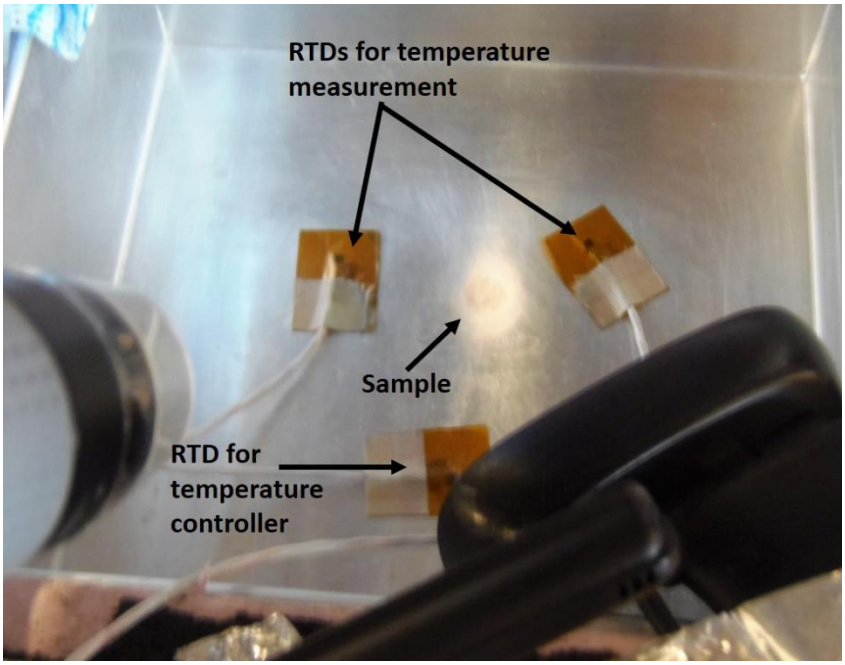

Figure 3.13. Arrangement of temperature sensors on the sample plate relative to the sample material.

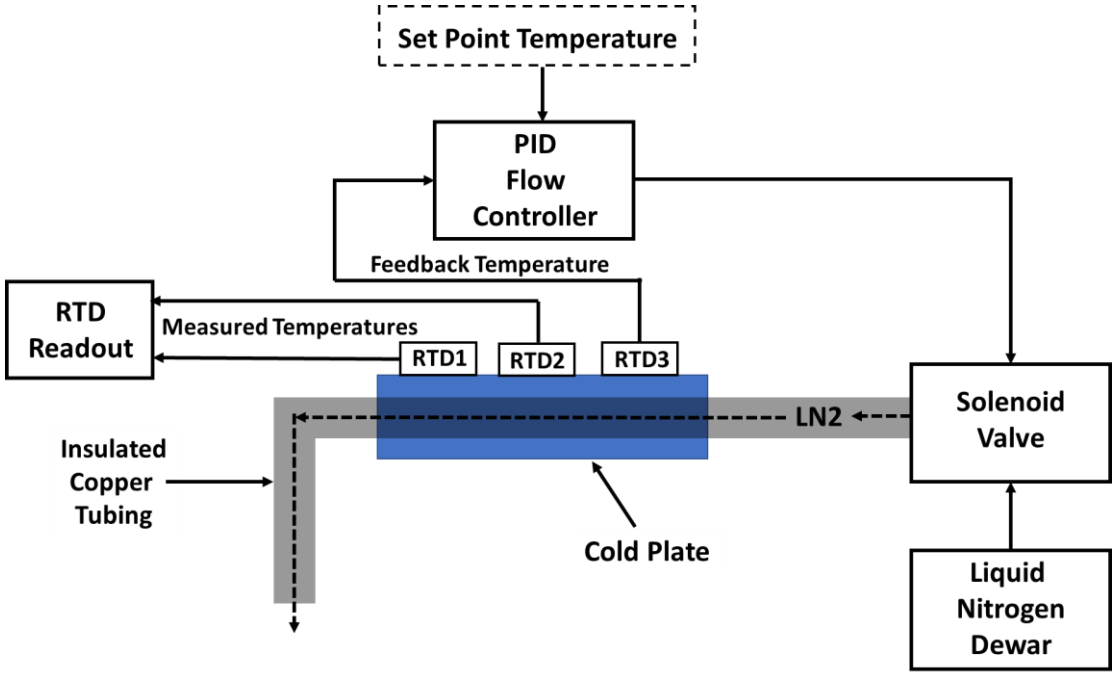

Figure 3.14. Diagram of the temperature control feedback loop.

3.4.2 Atmospheric Pressure and Humidity Measurement

The atmospheric pressure inside the chamber was set and maintained using a dry scroll vacuum pump (Varian TriScroll 300) which operated at a pumping speed of 300 liters/minute. A gas inlet valve at the rear of the chamber provided a means for introducing external air to the chamber interior.

The experiments of Chapter 4 were focused exclusively on studying the deliquescence of perchlorate samples, therefore achieving the correct water vapour partial pressure inside the chamber was the main priority, with the total pressure and overall atmospheric composition being secondary goals. During these experiments, the desired water vapour partial pressure was acquired by decreasing the total pressure in the chamber until the required frost point temperature was achieved. This coincidentally resulted in a total pressure inside the chamber that matched the total pressure measured at the surface of Mars during the Phoenix mission. The vacuum pump was then continuously operated, and the water vapour partial pressure was maintained throughout the experiments by flowing a constant stream of ambient room air into the chamber.

Achieving the correct atmospheric mixture of carbon dioxide and water vapour was critical to the adsorption experiments carried out in Chapter 5, therefore the experimental setup was advanced to include the ability to control the flow of carbon dioxide into the chamber. The required water vapour partial pressure was first achieved using the method described above. A valve was then used to simultaneously flow research grade carbon dioxide into the chamber from a gas cylinder until the total pressure inside the chamber was 800 Pa. This mixed air flow was continuously maintained during the experiments while the vacuum pump operated.

The atmospheric composition was not directly measured in the experiments; however, estimates are provided in Table 3.2 based on the known compositions of the carbon dioxide gas cylinder, the Earth atmosphere, and the amount of pressure that each contributed to the total pressure inside the chamber. For comparison, Table 3.2 also displays the known composition of the Martian atmosphere.

The total pressure inside the chamber was measured with a capacitance manometer (Edwards Barocel 600) which had an accuracy of 0.15% of the reading. Capacitance pressure sensors consist of a thin diaphragm and fixed capacitance electrodes. Variations in pressure deflect the diaphragm, altering the distance between the capacitance plates and resulting in a change in the measured capacitance that is proportional to the pressure change. The total pressure was also independently measured using an aneroid barometer (Wallace & Tiernan Pennwalt Precision FA160) which measured the expansion and contraction of an evacuated capsule in response to changes in the surrounding air pressure.

The atmospheric water vapour content inside the chamber was measured using a capacitive polymer sensor (Vaisala DMT152) which was mounted approximately 30 cm above the surface of the sample plate (Fig. 3.15). The sensor had a quoted accuracy of ±2ºC in frost point temperature over the range of -40ºC and -80ºC. Capacitive humidity sensors make use of the fact that the dielectric constant of polymer materials changes in response to changes in the atmospheric relative humidity around the sensor. Water vapour is absorbed by the polymer with increasing humidity and this results in a quantifiable increase in the capacitance of the sensor. The Vaisala sensor was bonded together with a platinum resistance thermometer which allowed the air temperature at the sensor to be measured simultaneously. The frost point temperature was automatically calculated by

the sensor using the humidity and air temperature measurements. During each experiment, the measured frost point temperature was further verified by visually observing the temperature at which frost formed on the sample plate. This step also ensured that the liquid nitrogen plumbing was properly insulated, and that water vapour was reaching the sample plate surface.

	Chapter 4 Experiments	Chapter 5 Experiments	Mars
Total Pressure	646 to 726 Pa	800 Pa	725 to 850 Pa *
% Carbon Dioxide	<1 %	93 to 96 %	96.0 %
% Nitrogen	78 %	3 to 6 %	1.9 %
% Argon	1 %	<1 %	1.9 %
% Oxygen	21 %	1 to 2 %	<1 %
Water Vapour Partial Pressure	2.1 Pa	0.5 to 2.1 Pa	0.1 to 2.1 Pa *
			* = measured at the Mars Phoenix site

Table 3.2. Atmospheric composition of the air inside the environmental chamber during the experiments in Chapter 4 and Chapter 5, and the known composition of the Martian atmosphere.

3.4.3 Visual Imaging, Lighting, and Optical Alignment

A digital microscope camera (Plugable USB 2.0) was used to capture visual images of the sample and the surrounding sample plate. The camera was fixed to the end of a flexible arm and was mounted to the side of the sample plate in order to not interfere with the incoming laser beam or outgoing scattered light. The microscope camera had a light emitting diode (LED) halo light source, however this did not provide adequate lighting to distinguish fine features like frost formation on the sample plate when the chamber was sealed. Two flexible LED light strips were installed to provide additional lighting. They were carefully positioned at angles that maximized the illuminated surface area, while minimizing glare due to reflections from the aluminum sample plate. The camera and lights were positioned far enough above the surface of the sample plate to ensure that there was no incidental heating of the sample from the imaging system. Figure 3.15 shows the arrangement of cameras and light sources around the sample plate.

A second camera (Logitech C270) was installed in the chamber to provide live images of the entire sample plate. This camera was used to optically align the Raman lidar system with the environmental chamber. The chamber was first aligned with the receiver of the lidar by focussing light from an LED flashlight through an optical fiber that was placed at the focal plane of the receiver system. This produced a distinct image of the fiber end face on the sample plate and the chamber was positioned so that the fiber image overlapped the sample material. The lidar transmitter was then aligned with both the chamber and the receiver by steering the laser beam so that the sample material, the fiber image from the receiver, and the transmitted laser beam spot all overlapped on the sample plate.

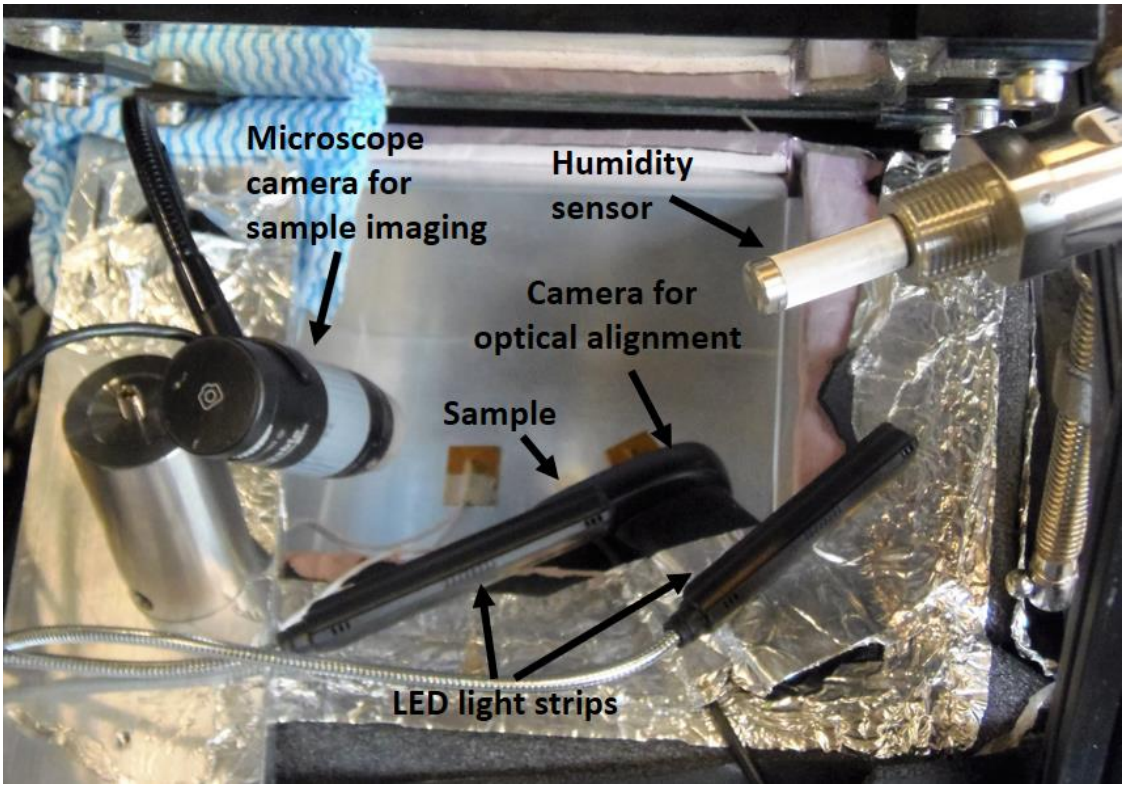

Figure 3.15. Arrangement of the humidity sensor and the camera and lighting system around the sample plate.

3.4.4 Feedthroughs

An electric feedthrough was required to enable the transfer of electrical power into and out of the sealed chamber. This was provided using male and female DB-subminiature (DB-25) connectors which were permanently fixed to a vacuum-tight aluminum flange on the front of the chamber. These connectors were interfaced with removeable connectors that had a mating male/female DB-25 connector on one side and 25 individual solder cup pins on the opposite side. The required electric wiring was soldered to the pins

on either side of the environmental chamber. These connections included three 3-wire RTDs for temperature measurement and control and three 3-wire spliced USB cables that were used for camera, lighting, and humidity sensor control. These connectors could be swapped out to allow for various electrical configurations.

A liquid nitrogen feedthrough was mounted on to the same aluminum flange. This consisted of two 0.25-inch Swagelok tube fittings that joined the copper liquid nitrogen plumbing on either side of the sealed chamber and allowed liquid nitrogen to flow into and out of the sealed chamber.

Chapter Four

Deliquescence, Freezing, and Efflorescence of Magnesium Perchlorate Hexahydrate Under Mars Conditions

4.1 Introduction

A major discovery of the NASA Phoenix Mars mission was the identification of perchlorate (ClO_4^-) in the surface regolith by the Wet Chemistry Laboratory (WCL) instrument [*Hecht et al*., 2009]. The Surface Stereo Imager (SSI) on Phoenix also identified spectral features consistent with hydrated perchlorate in the excavated trenches, suggesting that aqueous redistribution of perchlorates had likely occurred [*Cull et al*., 2010]. Analysis of the Phoenix WCL data [*Kounaves et al.,* 2014] indicated that magnesium perchlorate hexahydrate $Mg(ClO_4)_2 \bullet 6H_2O$ was likely to be one of the dominant parent salts found at that site and that finding was further supported by chemical modelling studies [*Toner et al*., 2014]. More recently, the Sample Analysis at Mars (SAM) instrument on the NASA Curiosity Rover detected the presence of perchlorate in Gale Crater [*Glavin et al*., 2013], suggesting that it is globally distributed. Reflectance spectra measurements made by the Compact Reconnaissance Imaging Spectrometer for Mars (CRISM) instrument on the Mars Reconnaissance Orbiter (MRO) have also identified magnesium perchlorate in Recurring Slope Lineae (RSL), dark streaks which appear seasonally on steep Martian slopes [*Ojha et al.,* 2015].

Perchlorate salts are of great interest for studies of Mars due to their high affinity for water vapour (deliquescence) as well as an ability to greatly depress the freezing point of water when in solution [*Chevrier et al*., 2009; *Renno et al.*, 2009]. This has intriguing biological implications since liquid brines could potentially provide a habitable environment for living organisms [*Davila et al*., 2010]. Additionally, it has been speculated that these salts may play a significant role in the hydrological cycle on Mars [*Hecht et al*., 2009] and are also possibly involved in the formation of RSL streaks [*Chojnacki et al*., 2016].

A crystalline salt is said to deliquesce when it absorbs water vapour directly from the atmosphere and forms an aqueous solution. This process is triggered when the ambient relative humidity increases above a certain critical value that is characteristic to the salt [*Martin et al*., 2000]. Above this deliquescence relative humidity (DRH), aqueous solution is the thermodynamically favored phase, while below this threshold the crystalline solid phase is favoured. The reverse process, efflorescence, is the recrystallization of the salt as liquid water is released back to the atmosphere when the ambient relative humidity is reduced below the DRH.

Previous experiments have examined the deliquescence properties of single particles of perchlorate using a Raman microscope and environmental cell. *Gough et al*. [2011] studied the deliquescence of perchlorate over the temperature range of 0^{o}C to -50^{o}C and found that their experimental results agreed with the calculations of *Chevrier et al*. [2009]. Specifically, $Mg(ClO_4)_2 \bullet 6H_2O$ was found to deliquesce at 55% relative humidity at -50^{o}C. While this previous work on microscopic samples demonstrated that perchlorate deliquescence should be thermodynamically favoured under certain Martian

conditions, other experimental results have indicated that the process is not rapid enough to allow for a substantial amount of bulk deliquescence during the Martian diurnal cycle [*Fischer et al*., 2014]. There also exists some question as to the exact nature of the eutectic temperature of the magnesium perchlorate-water system with previously measured freezing point depressions ranging from -68^{o}C [*Pestova et al*., 2005] to -57^{o}C [*Stillman and Grimm,* 2011]. It has even been suggested that magnesium perchlorate brines could remain as a super-cooled liquid throughout the entirety of the coldest Martian nights [*Toner et al*., 2014b]. This has important implications since brine freezing would impose a limit on the lifetime of any liquid water solutions formed by deliquescence on Mars.

The following experiments have addressed these questions by subjecting bulk samples of magnesium perchlorate hexahydrate to the thermodynamic conditions found at the Phoenix Mars landing site and detecting the uptake of water using laser Raman scattering. Another purpose of the experiments was to develop the methodology for a Raman lidar (light detection and ranging) instrument to study surface-atmosphere water exchange and brine formation from the surface of Mars during a landed mission. Lastly, the experimental results were combined with the output from a general circulation model (GCM) of Mars to determine the global and seasonal distribution of liquid perchlorate brines on the surface of Mars.

4.2 Experimental Method

When a beam of monochromatic light encounters a sample, a fraction of the scattered light is uniquely shifted in wavelength according the vibrational and rotational energy levels of the molecules it interacts with. This is called Raman scattering and it allows for the discrimination of the molecular composition of the sample. A Raman lidar instrument based on this concept was developed for this study. It was built on the heritage of the lidar instrument on the NASA Phoenix Mars mission [*Whiteway et al.*, 2008, 2009] and was capable of performing range-resolved atmospheric measurements as well as probing the near-range surface. The radiation source was the fourth harmonic output of a Q-switched Nd:YAG laser emitting pulses at a wavelength of 266 nm, a repetition rate of 20 Hz, and an energy of 15 mJ. In the near-range mode, the light was directed a distance of 2 meters toward a sample located inside an environmental chamber and the resulting backscatter was collected with a telescope. A detailed description of the Raman lidar is provided in Chapter 3 of this dissertation.

An environmental chamber was used for recreating the thermodynamic conditions at the surface of Mars as measured during the Phoenix mission. The sample was placed on a plate that was temperature controlled using liquid nitrogen and feedback from platinum resistance thermometers. The chamber was filled with ambient room air and the total pressure was decreased to a value for which the partial pressure of water vapour was 2.1 Pa (-55°C frost point temperature), and maintained throughout the experiment. This value of water vapour pressure is consistent with daytime measurements by the Thermal and Electrical Conductivity Probe (TECP) on the Phoenix mission [*Zent et al.*, 2010]. The total pressure required in the chamber was 726 Pa and this coincidentally matched the

surface pressure measured during the second half of the Phoenix mission [*Taylor et al*., 2010]. The liquid nitrogen plumbing was carefully insulated with polyethylene material to ensure that any water condensation occurring in the chamber was restricted to the sample plate. The water vapour content was monitored using a Vaisala capacitive sensor (DMT152) and confirmed by determining the temperature at which frost forms on the sample plate (adjacent to the patch of perchlorate) as indicated by a change in intensity of visual images. Repeated cycling of the temperature above and below the frost point demonstrated that the frost point remained consistent to within 0.5°C over the course of 5 hours. A camera provided a continuous visual record of the sample from inside the chamber while the laser Raman lidar measurements were acquired.

4.3 Measurements

4.3.1 Raman Scattering Spectra

Raman spectroscopy is a well-developed non-destructive technique used for molecular sample identification and quantification. When monochromatic laser light interacts with a sample of molecules, a small portion of the scattered photons are uniquely shifted in wavelength according to the vibrational and rotational energy levels of the molecules within the sample. This inelastic scattering results in a unique Raman spectrum for each molecule. Raman spectroscopy is presently viewed as a high priority technique for planetary exploration, with the first space-bound Raman instruments planned for both the NASA 2020 and ESA ExoMars rovers [*Wiens et al.,* 2016; *Abbey et al*., 2017; *Lopez-Reyes et al*., 2013]. A Raman spectrum consists of a plot of the measured signal amplitude of the Raman scattered light as a function of the shift in wavelength, or wavenumber

(cm^{-1}). Raman spectra are plotted in such a way that the laser excitation corresponds with a wavenumber shift of 0 cm^{-1}. Figure 4.1 shows the measured Raman spectrum of dry magnesium perchlorate hexahydrate. The unique series of peaks at wavenumbers less than 1500 cm^{-1} are attributed to the perchlorate ion Raman vibrational modes [*Patel et al*., 1983], while the peak near 3500 cm^{-1} is due to chemically bound water of hydration.

Raman spectroscopy has proven to be a highly effective technique for discriminating between different states of water [*Durickovic et al*., 2011] due to the O-H stretching band of water, located in the Raman shifted spectral region between 2800 cm^{-1} and 3800 cm^{-1}. This sensitivity of the O-H band is demonstrated in Fig. 4.2, which shows measured Raman spectra of liquid water at 5°C, water ice at -15°C, and dry magnesium perchlorate hexahydrate. The vertical line indicates the location of the spectral feature at 3150 cm^{-1} used for the experiment described in Sec. 4.3.2.

A sample of magnesium perchlorate hexahydrate acquired from Caledon Labs (#4770-1) was subjected to the water vapour pressure, background pressure, and temperatures measured at the Phoenix landing site. The samples had a sub-mm depth and a roughly 5 mm diameter, consistent with the median size of perchlorate patches identified at the Phoenix site [*Cull et al*., 2014].

While the temperature was lowered and subsequently raised, the Raman scattering signal at a wavenumber shift of 3150 cm^{-1} was continuously monitored. This spectral feature falls outside of the chemically bound water of hydration peak in the magnesium perchlorate hydrate (Fig. 4.2), but well within the broader liquid water and ice ranges. Any changes in the signal at wavenumber 3150 cm^{-1} will correspond only to a relative change in liquid or ice water content. This feature was also chosen in order to exploit the

strong contrast in liquid water and water ice sensitivity. Full spectra encompassing the entire Raman spectral range were acquired at key points during the experiment.

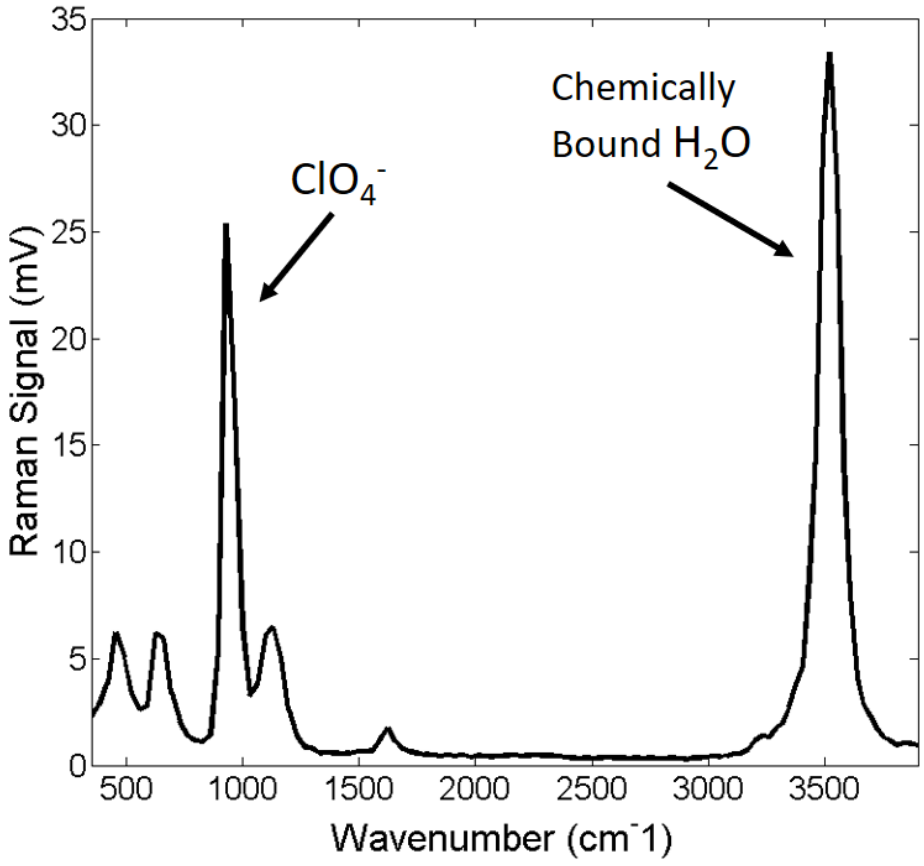

Figure 4.1. Raman spectrum of dry magnesium perchlorate hexahydrate measured by the Raman lidar. The peaks at wavenumbers less than 1500 cm^{-1} are attributed to the perchlorate ion Raman modes while the peak near 3500 cm^{-1} is due to chemically bound water of hydration.

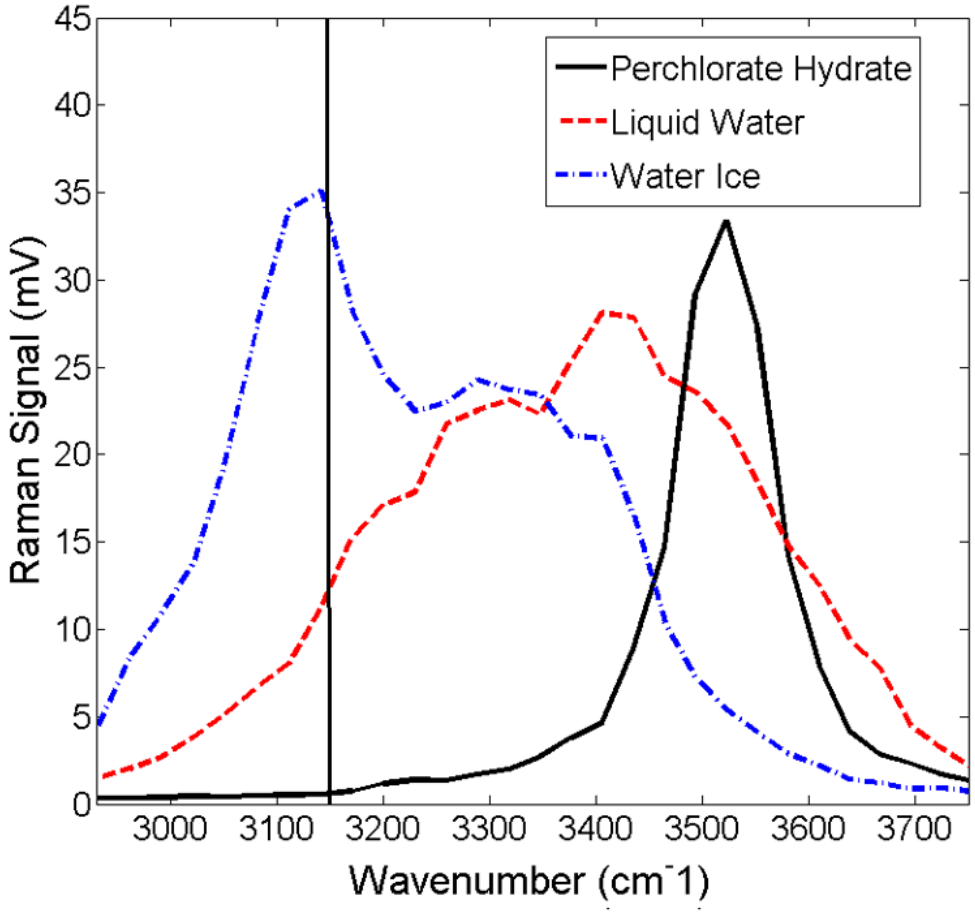

Figure 4.2. Raman spectra of liquid water, water ice, and magnesium perchlorate hexahydrate over the O-H stretch region. The vertical line indicates the location of the spectral feature used to generate the experimental results presented in Fig. 4.3.

4.3.2 Detection of Deliquescence, Brine Freezing, and Thawing

In order to study the magnesium perchlorate phase changes that would occur during a diurnal cycle at the Mars Phoenix site, the temperature was decreased from -42°C to -80°C and then increased to -56°C at a rate consistent with the surface temperatures measured by the Phoenix MET instruments on Sol 95 (Mars solar longitude, L_s= 120°) of the mission [*Dickinson*, 2008]. This was the wettest time of the year at the Phoenix site [*Tamppari et al*., 2010] and ground frosts had been observed by this point of the mission [*Smith et al*., 2009]. The water vapour partial pressure inside the environmental chamber was maintained at 2.1 Pa (-55°C frost point temperature) while the total pressure was 726 Pa. The laser beam of the lidar instrument was directed entirely on the magnesium perchlorate hexahydrate sample and the Raman backscatter signal at the wavenumber shift of 3150 cm^{-1} was recorded throughout the experiment to track changes in the liquid and ice water content.

Figure 4.3 shows the 3150 cm^{-1} Raman scattering signal and the temperature of the sample plate, which was measured directly adjacent to the perchlorate sample, as a function of time. No significant changes in the Raman signal were detected as the temperature was initially decreased from -44°C, signifying that no water uptake had occurred and the perchlorate sample remained dry. A sharp increase in the Raman signal was first observed at the 80-minute mark, indicating the onset of water uptake by the perchlorate sample. It was found that water uptake began to take place several degrees above the -55°C frost point temperature, with initial deliquescence occurring at -51°C (60% relative humidity over ice). The rate of water uptake was significant on the time scale of minutes and increased as the temperature was lowered to the frost point

temperature. Frost was immediately seen to form on the sample plate around the sample as the temperature was decreased below the frost point temperature. The Raman signal ceased to increase approximately 70 minutes after deliquescence was triggered, indicating that there was no further uptake of water by the perchlorate sample at that point.

The onset of brine freezing was indicated in Fig. 4.3 by a second stage of signal increase that commenced only when the temperature was lowered below -67°C at the 200-minute mark. The signal increased over the next hour, indicating that the perchlorate solution was gradually undergoing freezing. The Raman signal again ceased increasing at the 260-minute mark, indicating that complete freezing of the perchlorate brine had occurred. As the temperature was subsequently increased, the sample remained frozen until a temperature of -62°C was reached, at which point the Raman signal decreased dramatically indicating the onset of melting. Within 60 minutes the signal had returned to the previous level that corresponded to aqueous solution, signifying that complete melting had occurred and the sample was once more entirely in a liquid brine state. Measurements are not shown when the temperature was increased back above the frost point as the sublimation of frost from the sample plate resulted in an unrealistic excess of water vapour over the sample.

Full Raman spectra (Fig. 4.4) were also acquired at points indicated in Fig. 4.3: point A (prior to water uptake), B (following deliquescence), and C (following brine freezing). A linear least squares-based unmixing algorithm was applied to the O-H stretch region of these spectra using the Raman measurements shown in Fig. 4.2 for pure magnesium perchlorate hexahydrate, pure liquid water, and pure water ice as the known end-members (a description of this algorithm is provided in Appendix A). The spectral

decompositions at points B and C are shown in Figs. 4.5a and 4.5b. It was found that the Raman scattering spectrum at point B was composed exclusively of perchlorate hexahydrate and liquid water, with no water ice component present. This indicates that there was no freezing of the aqueous perchlorate solution down to a temperature of -65°C. In contrast to this, the spectrum at point C was nearly exclusively composed of perchlorate hexahydrate and water ice signifying that freezing of the brine had occurred.

To gain further insight, visual images (Fig. 4.6) were taken prior to water uptake (point A), following deliquescence (B), and following freezing (C). The initial bright white dry perchlorate patch visibly faded as it took up water and formed a film of aqueous solution. As the eutectic temperature was crossed and the brine froze, the perchlorate sample appeared to increase in brightness. At the same time, both patchy and spotty frost formed on the plate around the sample once the temperature was decreased below the frost point temperature of -55°C.

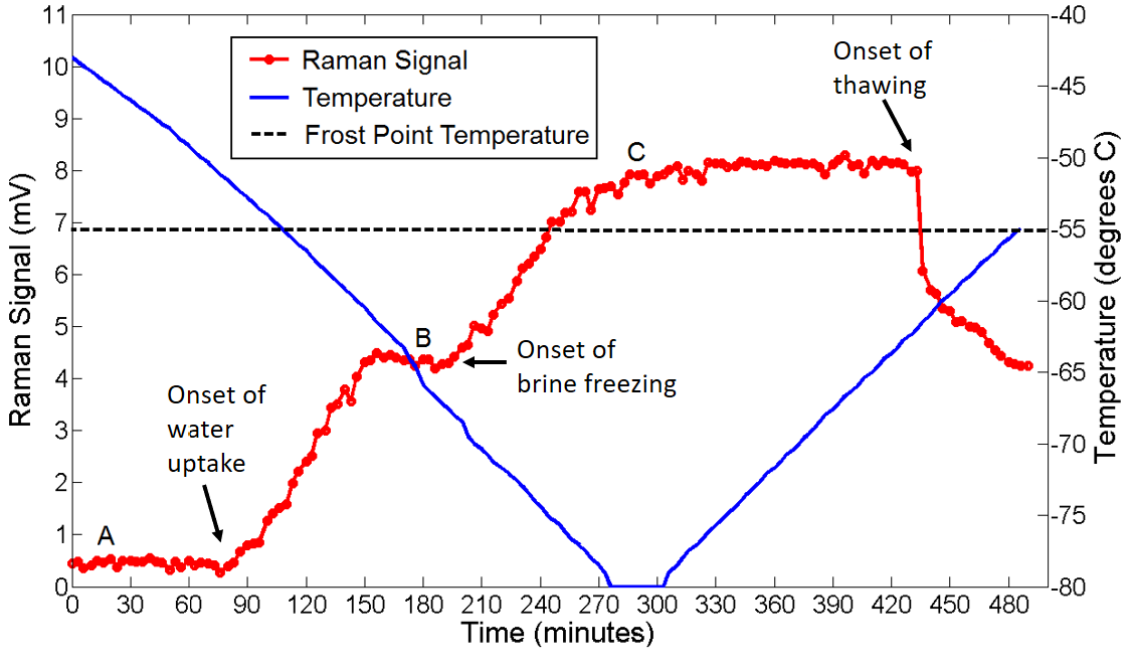

Figure 4.3. Measured Raman signal at a wavenumber shift of 3150 cm^{-1} as the temperature was lowered from -42°C to -80°C and then increased. Water uptake began at the 80-minute mark and ceased after 150 minutes. Freezing began at the 200-minute mark as the temperature was decreased below the eutectic temperature of -67°C. Melting occurred when the temperature was increased above -62°C at the 440-minute mark.

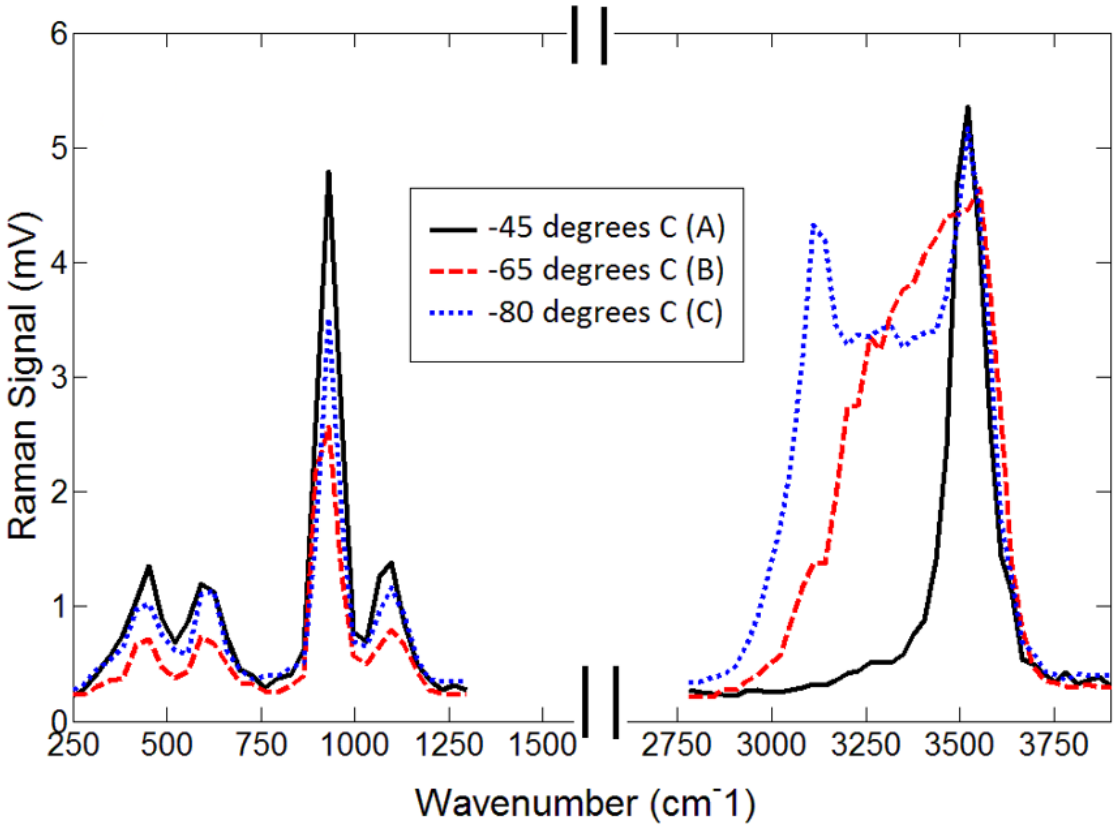

Figure 4.4. Spectra of magnesium perchlorate hexahydrate at various temperatures. The O-H stretch region broadened and increased in intensity as liquid water was taken up. As the solution froze, the characteristic water ice peak near a wavenumber shift of 3100 cm^{-1} became apparent.

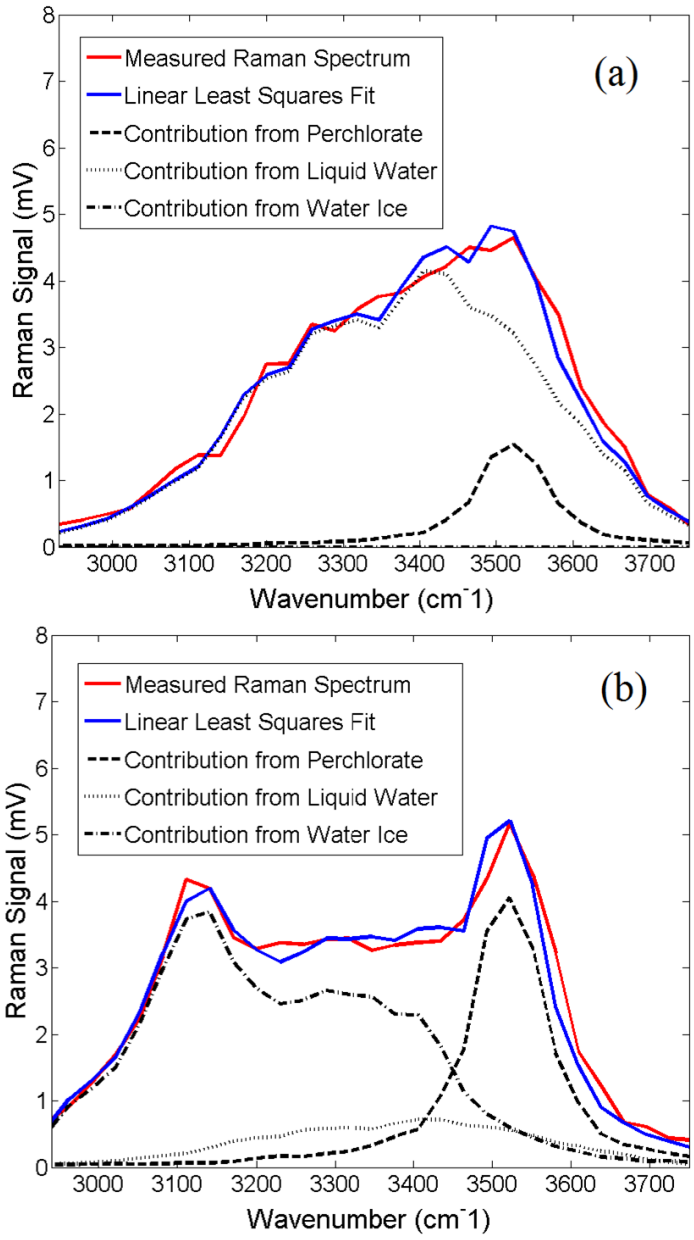

Figure 4.5. (a) Linear least squares fit of pure magnesium perchlorate hydrate, liquid water, and water ice Raman spectra applied to the spectrum at point B in Fig. 4.4 (following deliquescence). There was no contribution from water ice, and thus no freezing down to -65°C. **(b)** Fitting applied to the spectrum at point C in Fig. 4.4 (following brine freezing). The primary water ice and magnesium perchlorate hydrate composition is clear.

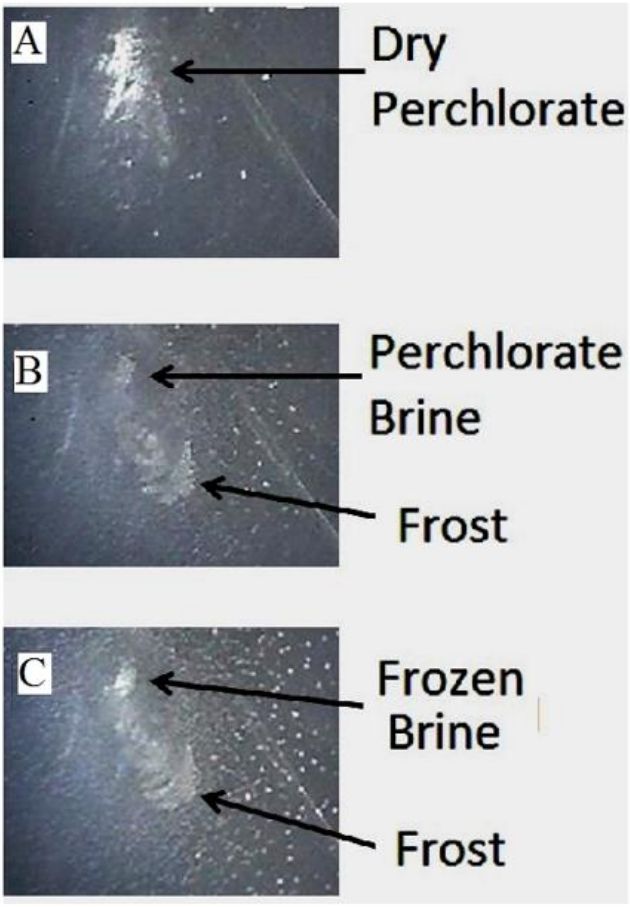

Figure 4.6. Visual images of magnesium perchlorate hexahydrate and the surrounding surface at points A, B and C. The perchlorate sample began to fade as water was taken up and aqueous solution formed (point B). As the brine froze at point C, the sample region appeared to increase in brightness. Frost was visible on the sample plate in panels B and C.

4.3.3 Deliquescence and Efflorescence at Temperatures Above the Frost Point

The goal of the second experiment was to study the efflorescence properties of magnesium perchlorate hexahydrate at the Mars Phoenix site. To achieve this, the temperature of the sample plate was decreased from -45°C to -53°C. The relative humidity over ice (RHi) for 2.1 Pa of water vapour at a temperature of -53°C is 77% which is well above the magnesium perchlorate hexahydrate deliquescence relative humidity of 60% found in the previous experiment. The temperature was held constant at -53°C for several hours while deliquescence occurred, and water was continuously taken up by the magnesium perchlorate sample. The temperature was not decreased below the frost point temperature during this experiment to avoid the influence of frost sublimation. The temperature was then increased at a rate consistent with the surface temperatures on the morning of sol 95 of the mission at the Phoenix landing site in order to observe the recrystallization of the magnesium perchlorate sample as water was returned to the atmosphere. The partial water vapour pressure in the chamber was again maintained at 2.1 Pa (-55°C frost point temperature) throughout the experiment, while the total pressure was 646 Pa. In contrast to the previous experiment which made use of the spectral feature at 3150 cm^{-1}, the Raman signal at a shift of 3250 cm^{-1} was monitored instead in order to take advantage of the higher sensitivity to liquid water at this wavenumber shift.

The results of this experiment are shown in Fig. 4.7 which clearly traces the changes in liquid water content over time. The entirety of the water uptake occurred at temperatures above the -55°C frost point, with deliquescence again beginning at -51°C (60% RHi). Water loss began to occur as the temperature was then increased back above the deliquescent relative humidity near the 350-minute mark. At a temperature of -42°C

(21% RHi), most of the liquid water had evaporated from the sample, however a very small amount was retained until complete efflorescence occurred at -36°C (10% RHi).

Complete spectra (Fig. 4.8a) were taken prior to water uptake (point A), following significant water uptake (B), and following complete efflorescence (C). The Raman peak in the O-H stretch region broadened as deliquescence occurred. Following efflorescence, the O-H peak sharpened and returned to the initial intensity. This indicates that the magnesium perchlorate sample remained in the hexahydrate state following a cycle of deliquescence and efflorescence, with none of the chemically bound water of hydration entering the water cycle. This is in agreement with the findings of *Robertson and Bish* [2011] who concluded that magnesium perchlorate hexahydrate is unlikely to undergo changes in hydration state under Martian conditions.

Visual images (Fig. 4.8b) show that the bright magnesium perchlorate hexahydrate patch (point A) faded as the sample absorbed water and formed aqueous solution (point B). As efflorescence occurred and water was returned to the atmosphere, the perchlorate sample recrystallized and the bright dry patch reappeared (point C).

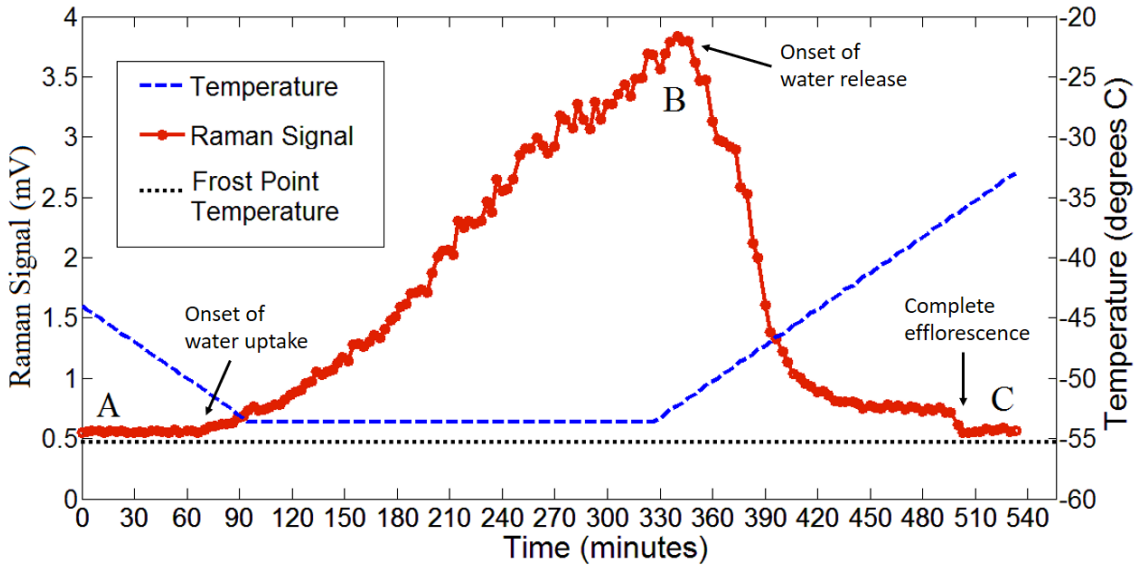

Figure 4.7. Measured Raman signal at a wavenumber shift of 3250 cm^{-1} while the temperature was decreased to -53°C (77% RHi) and then increased. Water uptake began at the 70-minute mark as the DRH was reached and deliquescence was triggered. Water began to be released at the 350-minute mark as the temperature was increased and efflorescence occurred.

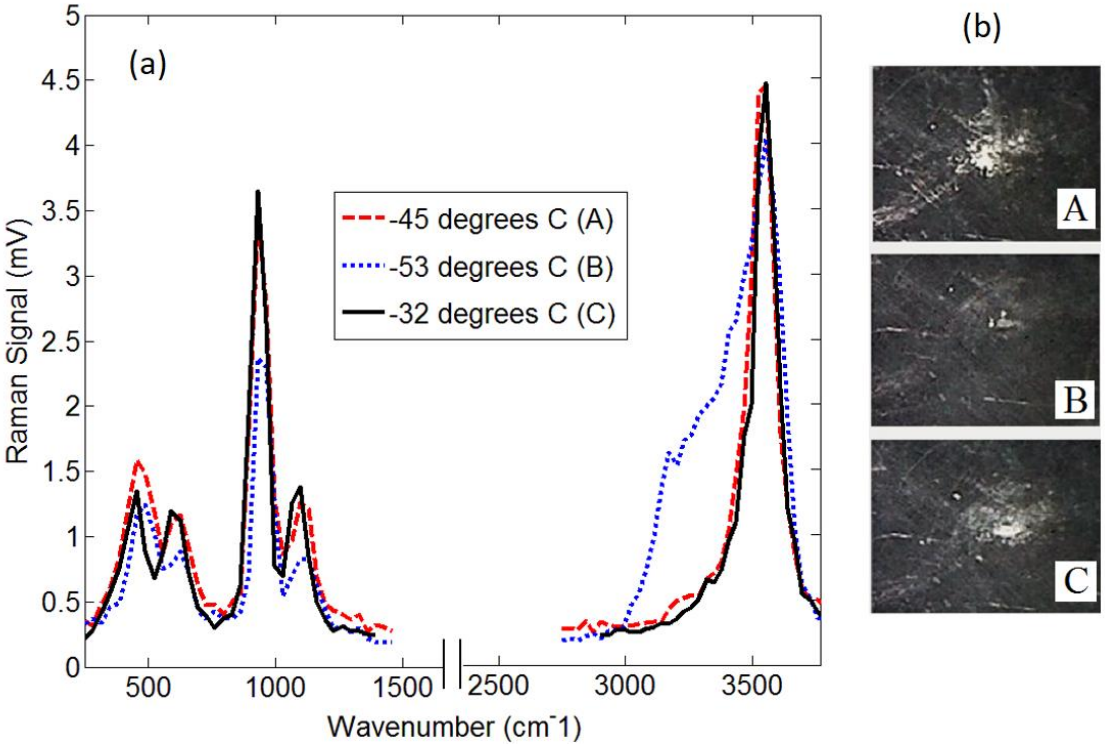

Figure 4.8. (a) Spectra of magnesium perchlorate hexahydrate at various temperatures. The O-H stretch region broadened in intensity as water was taken up by the sample. The O-H peak returned to the initial shape and strength following efflorescence, indicating that the magnesium perchlorate sample remained in the hexahydrate state. **(b)** Visual images of magnesium perchlorate hexahydrate deliquescence and efflorescence above the frost point. The bright perchlorate patch faded as water was taken up and later reappeared once efflorescence occurred.

4.4 Determination of the Global Distribution of Magnesium Perchlorate Brine Using a General Circulation Model

In order to determine the global and seasonal distribution of liquid perchlorate brine on Mars, the experimental results of Sec. 4.3 were combined with output from a General Circulation Model (GCM) of Mars which was developed at the Belgian Institute for Space Aeronomy (BIRA-IASB). This model was based on the Canadian Global Environmental Multiscale (GEM) model for weather forecasting on Earth [*Moudden and McConnell,* 2005]. It was operated on a spatial grid with a horizontal resolution of 4° latitude × 4° longitude (where the grid spacing at the poles was ~76 km and at equator was ~237 km) and with 103 vertical levels reaching from the surface to 150 km in height. It has been demonstrated that this GCM is able to accurately simulate the global distribution of temperature and water vapour abundance on Mars [*Neary and Daerden,* 2017]. The model was previously used to explain the formation mechanism and height of dust layers in the Martian atmosphere that were observed by the LIDAR on the Phoenix mission [*Daerden et al.,* 2015].

To generate the global analysis, the model was run for a full Martian year using a time resolution of 1 hour, and several simulated quantities were obtained at each time step. These included values of global surface temperatures and water vapour partial pressures which were converted to relative humidity at the surface using the water vapour pressure equations of *Buck* [1981]. In order to assess whether liquid brine formation was possible at a given time and location, two critical conditions for magnesium perchlorate deliquescence were required based on the experimental results of Sec. 4.3: (i) values of relative humidity over ice (RHi) that exceeded the magnesium perchlorate DRH of 60%

and (ii) surface temperatures that were above the magnesium perchlorate solution freezing temperature of -67°C. These calculations were carried out at every time step and grid location for the entire Martian year.

Figure 4.9 displays the latitudinal and seasonal distribution of locations where the two conditions for magnesium perchlorate deliquescence were satisfied (RHi greater than or equal to 60% and temperature greater than or equal to -67°C) based on the model output. This map was generated by summing the number of occurrences of deliquescence conditions being satisfied across all longitudes for a given line of latitude at each time step. The y-axis displays the geographical latitude on Mars, while the x-axis shows the time of year on Mars expressed in terms of solar longitude (Ls). The colour bar represents the percentage of time (or fraction of a latitude circle) that the deliquescence conditions are satisfied.

It was found that the conditions required for perchlorate deliquescence were met much more frequently at high northern latitudes. Brine formation was modelled to occur sporadically between 40°N and 60°N beginning around the northern winter solstice (Ls=270°), become wider spread (with occurrences between 25°N and 90°N) after the summer solstice (Ls=90°), and last until shortly before the autumnal equinox (Ls=180°). Occurrences were most frequent at the northernmost latitudes, nearest to the polar cap. Deliquescence conditions were less common at drier southern latitudes, with sporadic brine formation occurring between latitudes of 30°S and 70°S just before the southern spring equinox (Ls=150°). Deliquescence occurrences were more widespread in the southern hemisphere after the spring equinox, extending from 30°S to 90°S, before ending around the southern summer solstice (Ls=270°). The latitudinal location and duration of

the Phoenix mission is marked by a grey line on Fig. 4.9. Deliquescence conditions were found to be satisfied daily at the Phoenix site for up to 25% of the time starting around summer solstice and ending shortly before the end of the mission.

To determine whether perchlorate deliquescence could be responsible for the formation of Recurring Slope Lineae, Fig. 4.9 also shows the locations and times of year where RSL have been confirmed to form and grow [*McEwen et al.*, 2014; *Stillman et al.*, 2014, 2016; *Chojnacki et al*., 2016], marked as purple coloured boxes. RSL have been primarily found in three locations: at multiple southern midlatitude sites during the southern summer, at a single northern midlatitude location during the northern summer, and throughout the year at many sites near the equator in the southern hemisphere. The conditions required for deliquescence were found to be intermittently satisfied at the times of year and locations where the southern and northern midlatitude RSL have been found to form, indicating that the deliquescence of perchlorate may be able to play a role in their formation. On the contrary, no occurrences of deliquescence conditions being satisfied were found at latitudes between 25°S and 20°N over the entirety of the Martian year. The majority of RSL have been observed to occur close to the equator in the southern hemisphere, thus it is unlikely that most RSL are formed through the deliquescence of perchlorate salts unless a local mechanism exists for concentrating water vapour at these sites.

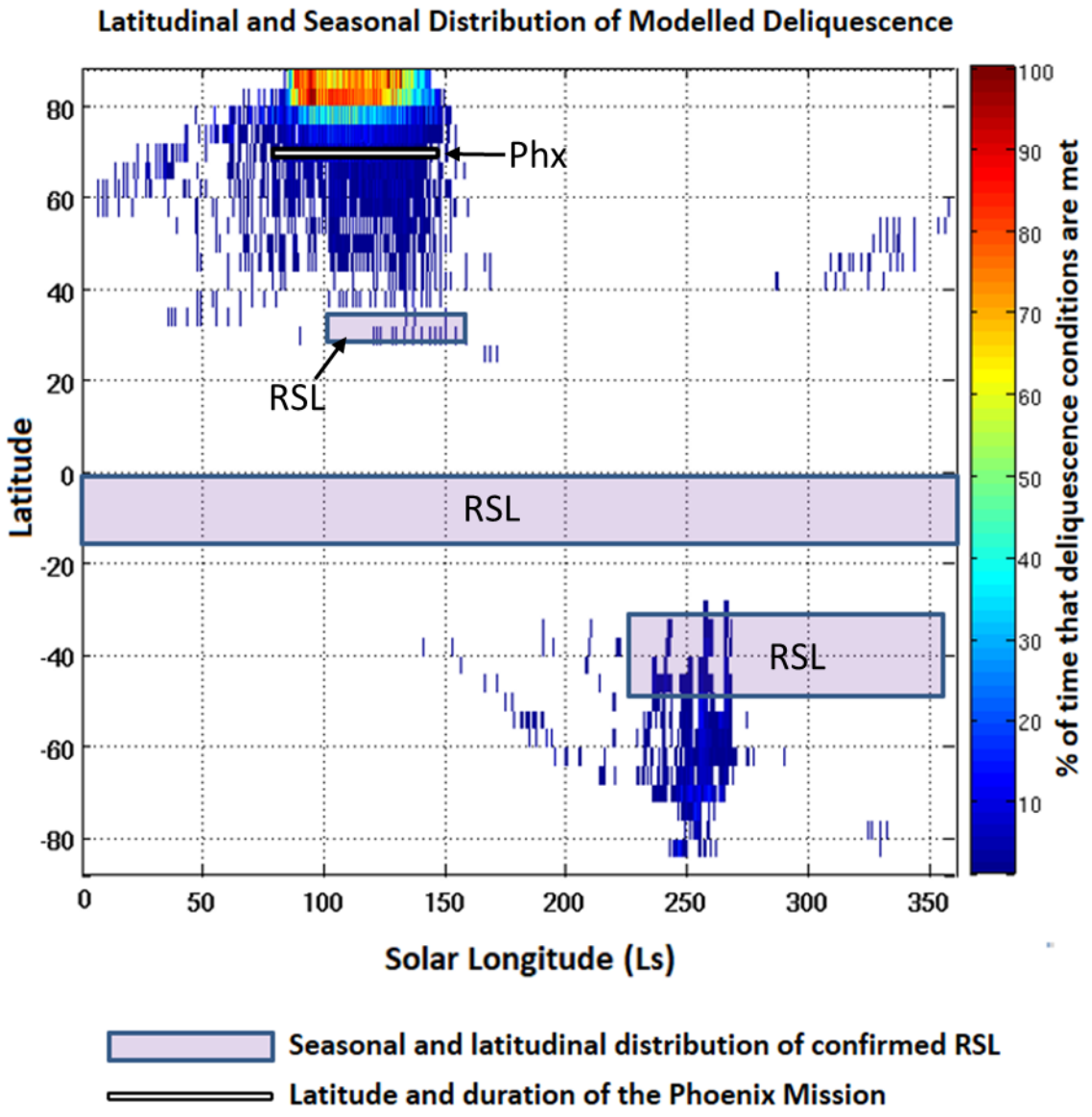

Figure 4.9. Latitudinal and seasonal distribution of locations where magnesium perchlorate deliquescence conditions were satisfied based on the Mars model output. The location and duration of the Phoenix mission and confirmed RSL sites are overlaid for comparison.

4.5 Discussion

4.5.1 Experimental Limitations

The experiments matched the temperature and humidity on Mars for the most crucial aspect of the study: deliquescence and efflorescence at temperatures above the frost point (-55ºC). At temperatures below the frost point, the water vapour pressure in the chamber was held constant and did not follow the decline that was observed near the surface at night during the Phoenix mission [*Zent et al.,* 2010]. Therefore, the results of the experiment at temperatures below the frost point are an identification of the freezing and thawing of the magnesium perchlorate brine solution, rather than a quantification of water uptake at night.

The terrestrial air used in the experiments differed from the primarily carbon dioxide atmospheric composition of Mars, resulting in a diffusion coefficient and thus flux of water vapour that is 30% greater in the experiment than would be expected at the surface of Mars [*Hudson et al*., 2007]. This resulted in an increase of water uptake by the same factor.

Further advancement of the experimental technique will be required to quantify the amount of water deposited per unit area. This will require a method for calibrating the measurement, such as comparison with Raman scattering from a known target.

4.5.2 Implications for the Mars Phoenix Site

The results of this work allow for the phase changes of magnesium perchlorate brine to be compared to the diurnal cycle in temperature measured at the Phoenix site on Mars. Water uptake by magnesium perchlorate hexahydrate would begin in the early Martian evening as the temperature decreased to -51°C and the deliquescent relative humidity was reached. This temperature occurred at a time of 6:30 pm on sol 95 during the Phoenix mission [*Dickinson,* 2008]. Resulting brine would exist as a liquid until the eutectic temperature of -67°C was reached 2 hours later at 8:30 pm. Freezing of the solution would occur over the next hour until the brine was completely frozen at 9:30 pm. The solution would remain frozen during the nighttime and early morning hours until the daytime temperature reached -62°C and thawing occurred at 5:00 am. Morning brine would exist until efflorescence was triggered when the temperature reached -51°C at 6:45 am. Most of the water on the surface would be given off to the atmosphere over the next hour and dry magnesium perchlorate hexahydrate would then exist until deliquescence was retriggered in the evening hours. Thus, liquid water magnesium perchlorate solutions could exist at the surface-atmosphere interface for up to 3 hours in the evening and 2 hours in the morning at the Phoenix site during the Martian summer. Potential processes occurring below the surface (e.g. at the surface regolith-ice table interface) are discussed in Sec. 7.2.3.

4.5.3 Deliquescence and Freezing of Perchlorate

When exposed to the water vapour pressure and temperatures found at the Phoenix landing site, magnesium perchlorate hexahydrate samples of the size found on Mars began to undergo deliquescence 4°C above the frost point temperature. Significant water uptake from the atmosphere began to occur within minutes, indicating that bulk deliquescence is likely to occur on present-day Mars. This demonstrates that perchlorate in the regolith can contribute to the Martian hydrological cycle by absorbing water and pre-emptively reducing the water vapour pressure prior to 100% relative humidity being reached during the evening. This finding is consistent with the pattern of evening decrease in atmospheric water vapour content which was measured by the TECP instrument at the Mars Phoenix site (Fig. 2.3). This result contradicts the findings of *Fischer et al.* [2014] which suggested that the kinetics of bulk deliquescence would be too slow for it to be a significant process on Mars.

The onset of magnesium perchlorate hexahydrate brine freezing was found to occur at -67°C, which is consistent with previously determined magnesium perchlorate eutectic temperatures [*Marion et al*., 2010; *Chevrier et al*., 2009]. Re-melting was observed to occur at a temperature of -62°C. The brine freezing was found to take over an hour to be complete. The slow kinetics of the freezing process would allow for the lifetime of liquid water perchlorate solutions on the surface to be extended during the nighttime hours, however this would largely be off-set by the hysteresis effect observed in freeze-thaw cycle, as re-melting does not occur until a temperature of -62°C is reached.

Figure 4.10 displays the experimental results from Sec. 4.3.2 superimposed on the eutectic phase diagram of magnesium perchlorate (see Sec. 2.10). The sample was

composed of 100% dry perchlorate as the experiment began at a temperature of -44°C (region A). As the temperature was decreased past -51°C and the deliquescence relative humidity was reached, the sample began to take up water vapour from the atmosphere and form a liquid solution, resulting in a mixture of liquid water and perchlorate and thus lowering the perchlorate concentration (region B). When the eutectic temperature of -67°C was reached, the sample began to freeze, resulting in a mixture of solid perchlorate and water ice (region C). While the exact concentration of perchlorate within the solution could not be determined during the experiment, it is likely that the concentration remained above the eutectic concentration of 44% by weight throughout the experiment, as freezing was not observed until the eutectic temperature was reached.

4.5.4 Implications for Recurring Slope Lineae

Modelled simulations of surface temperature and water vapour pressure at the surface of Mars were used to determine the global and seasonal distribution of perchlorate brine formation (Fig. 4.9). It was found that the most likely sites on Mars for hosting liquid solutions were pole-ward of 40°, both in the northern and southern hemispheres. Brine formation was much more frequent in the northern hemisphere, during the northern summer. At no point during the Martian year were the conditions required for perchlorate deliquescence satisfied between latitudes of 20°N and 20°S. Perchlorate deliquescence may therefore play a role in the formation of mid-latitude Recurring Slope Lineae, but it cannot explain the presence of RSL near the equator.

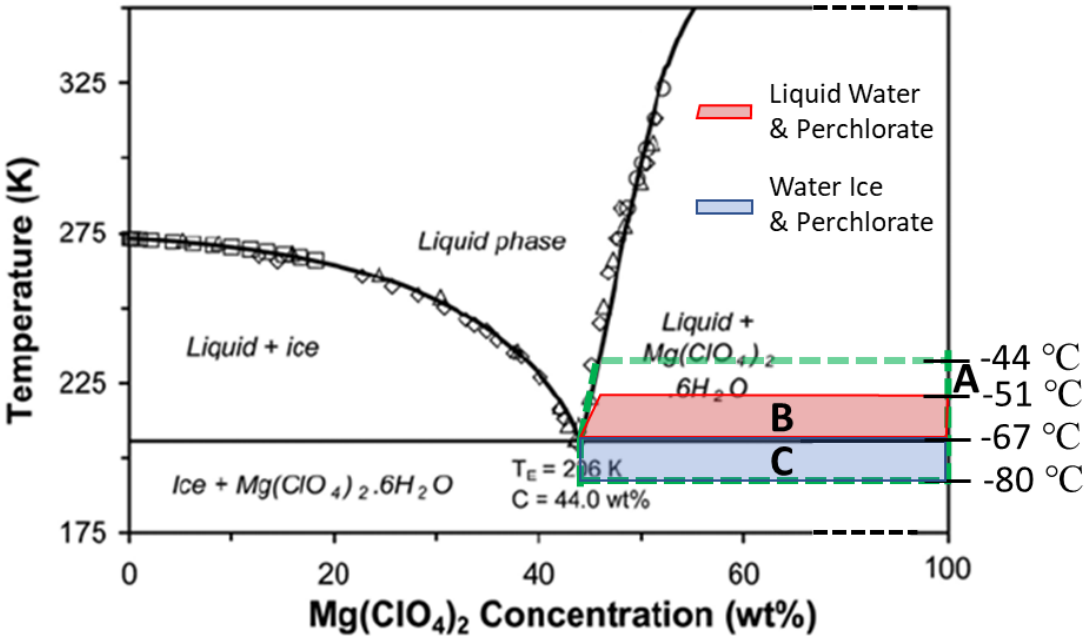

Figure 4.10. Experimental results of Sec. 4.3.2 superimposed on the eutectic phase diagram of magnesium perchlorate. The sample was composed entirely of perchlorate (point A) until the deliquescence relative humidity was reached at -51°C. The perchlorate concentration decreased as the sample took up water and began to form a liquid solution (region B). The sample froze below -67°C, resulting in a mixture of solid perchlorate and water ice. [Figure modified from *Chevrier et al.*, 2009].

4.5.5 Detection During a Landed Mission

It has been demonstrated that Raman spectroscopy provides an effective method for directly detecting the processes associated with surface-atmosphere water exchange on Mars. Specifically, the perchlorate ion Raman spectral features allowed for unambiguous detection of perchlorate salts, while the O-H Raman modes allowed for detection of the onset and relative amount of liquid water uptake and loss, and brine freezing and thawing. During a landed mission, monitoring of the O-H Raman signal over the course of a diurnal cycle would provide a clear indication of liquid brine film formation and freezing. These measurements could be acquired with a Raman lidar instrument from a stand-off distance without the need for sample preparation.

Chapter Five

Adsorption and Deliquescence Under Mars Conditions

5.1 Introduction

Sensors on board the NASA Phoenix Mars lander and the NASA Curiosity rover have provided measurements of relative humidity and temperature directly from the surface of Mars [*Zent et al.*, 2010; *Harri et al.*, 2014]. A striking feature common to both data sets was the observation that the atmospheric water vapour content near the surface decreased in the evening, often prior to 100% relative humidity (over ice) being reached, and then increased again during the daytime (Fig. 2.3). This indicates that a significant exchange of water is occurring between the atmosphere and surface of Mars on a diurnal time scale which cannot be explained by frost deposition alone. Current knowledge of Martian surface mineralogy suggests that the processes most likely responsible for this exchange are deliquescence of salts such as perchlorate [*Hecht et al.,* 2009] and/or the adsorption of water onto mineral grains [*Jakosky et al.,* 1997].

Chapter 4 demonstrated that the various phase changes involved in the magnesium perchlorate deliquescence/freezing/efflorescence cycle can be detected using Raman spectroscopy and that magnesium perchlorate can play an active role in the present Martian water cycle. The laboratory experiments presented in this chapter have built on those results by examining the process of adsorption as well as the deliquescence of

perchlorate salt mixed within an adsorbing regolith. The first objective of this work was to determine whether Raman spectroscopy could detect the adsorption of molecules on surface mineral grains and, if so, whether the adsorption of water could be discriminated from other forms of water such as perchlorate brine solution and mineral hydrates. The second aim was to conduct water exchange process studies related to adsorption and deliquescence by simulating the mineralogical composition and thermodynamic conditions found on Mars.

Physical adsorption of water is an easily reversible process in which vapour molecules become attached to regolith grains due to van der Waals forces between the dipolar water molecules and the mineral grains [*Mohlmann*, 2005]. This results in a thin film of liquid-like water forming on the surface of the grains. The presence of adsorbed water on Mars is intriguing as it raises the question of whether it could support microbial life [*Mohlmann*, 2005]. Modelling results also indicate that adsorption can play a substantial role in diurnal changes in atmospheric water vapour content that were observed at the northern high latitude Mars Phoenix site [*Rivera-Valentin and Chevrier,* 2015] and at equatorial Gale Crater [*Savijarvi et al.*, 2016]. The presence of adsorbed water at the Phoenix site was further supported by the cohesive nature of regolith samples that were investigated by the Mars Phoenix Lander Robotic Arm experiment [*Arvidson et al.,* 2009]. On a global scale, the implementation of an adsorbing regolith into a General Circulation Model of Mars was found to produce more accurate simulations of the global Martian water cycle [*Böttger et al.,* 2005].

Zeolites are naturally occurring hydrated aluminosilicate minerals that provide significant adsorption potential due to their large specific surface area. Zeolites have been

detected in the surface dust of Mars using the Mars Global Surveyor Thermal Emission Spectrometer [*Ruff*, 2004], in the regions surrounding the Mars Phoenix site by the OMEGA instrument on the ESA Mars Express orbiter [*Poulet et al.,* 2010], and at several additional Martian sites using the CRISM instrument on the NASA Mars Reconnaissance Orbiter (MRO) [*Carter et al.*, 2013]. While the specific types of zeolites on Mars is undetermined, chabazite $(Ca,Na_2,K_2,Mg)Al_2Si_4O_{12}\cdot 6H_2O$ is a commonly occurring natural zeolite and a likely candidate [*Mousis et al.,* 2016].

Various experimental studies have investigated the role of adsorption on Mars. *Zent et al.* [2001] studied the adsorption properties of Na-montmorillonite and found that the slow adsorption kinetics likely preclude a role for smectite clays in the diurnal water cycle. Similarly, *Janchen et al.* [2009] concluded that the adsorption kinetics of palagonite are likely too slow to affect the diurnal water cycle. *Janchen et al.* [2006] also studied the adsorption properties of pure clays and zeolites at Mars relevant water vapour pressures over the temperature range of -16ºC to 60ºC. By extrapolating to lower temperatures, it was concluded that these minerals can hold up to 2.5 to 25 percent by weight of water at a partial water vapour pressure of 0.1 Pa. *Beck et al.* [2010] studied the water adsorption properties of various minerals and found that ferrihydrite, an iron oxyhydroxide, most notably had rapid kinetics which may allow for an active role in the diurnal water cycle.

Deliquescence occurs when the ambient relative humidity increases above a certain critical value (the deliquescence relative humidity) that is unique to the specific type of perchlorate as well as the partial pressure of water vapour. The experiments reported on in Chapter 4 demonstrated that macroscopic magnesium perchlorate hexahydrate samples undergo deliquescence at 60% relative humidity over ice with 2.1

Pa of water vapour partial pressure. It was also determined that the resulting magnesium perchlorate solutions remained in the liquid phase until freezing occurred at -67°C. While perchlorates have now been studied under Martian conditions, experiments involving perchlorate/regolith mixtures are still lacking. It has yet to be determined if the deliquescence of perchlorate can explain dark RSL features given the low amounts of atmospheric water vapour on Mars or if the presence of adsorbed water on surrounding mineral grains can affect the deliquescence of perchlorate by providing a source of water.

5.2 Experimental Method

The Raman lidar and environmental chamber experimental setup was operated using the near-range configuration presented in Chapter 3. The environmental chamber was refined for the experiments carried out in this chapter to better simulate the primarily carbon dioxide atmosphere of Mars. The desired water vapour partial pressure inside the chamber was first set by flowing a continuous stream of ambient room air into the chamber. The chamber was then back-filled with a continuous flow of carbon dioxide gas and maintained at a total pressure of 800 Pa. This method resulted in an atmospheric composition inside the chamber that was between 93% and 96% CO_2 for all of the experiments carried out. The frost point temperature inside the chamber was measured with a Vaisala capacitive polymer sensor (DMT152) and was further verified by visually observing the temperature at which frost formed on the sample plate. Visual images of the sample and the surrounding sample plate were taken using a digital microscope camera which was placed inside the chamber.

The research grade natural chabazite used in all the experiments was acquired

from Ward's Science (#495935) and the quartz sand was acquired from Sigma Aldrich (#274739). Both were ground and sieved to a grain size range of 25 to 50 microns. The magnesium perchlorate hexahydrate used in the experiments of Sec. 5.3.3 was acquired from Caledon Labs (#4770-1). Each sample was placed under vacuum for 24 hours before the desired water vapour partial pressure was set. The atmospheric composition within the chamber was then left to equilibrate for 24 hours at room temperature before any measurements were taken. The samples all had a sub-mm depth and a roughly 10 mm diameter. The diameter of the sample was chosen to match the size of the laser beam. The thickness of the sample was chosen to minimize thermal transfer and gas diffusion effects which would be expected within a thicker sample. This ensured that the temperature of the sample material matched the temperature of the sample plate and the relative humidity within the sample material matched the atmospheric relative humidity surrounding the sample.

5.3 Measurements

5.3.1 Raman Scattering Spectra

Figure 5.1 shows the measured Raman spectrum of the zeolite chabazite at a temperature of 20°C in 800 Pa of carbon dioxide gas and a water vapour partial pressure of 1 Pa. The peaks at wavenumbers 480 cm^{-1} and 1100 cm^{-1} were attributed to the aluminosilicate structure of the chabazite [*Yu et al.*, 2001], while the peak near 3500 cm^{-1} was due to a combination of chemically bound water of hydration and physically bound adsorbed water. Figure 5.2 displays the Raman spectrum of quartz sand taken under the same conditions. The peak at 465 cm^{-1} was attributed to the symmetric Si-O-Si stretching-

bending mode of the quartz [*Kingma and Hemley.,* 1994] and the lack of features above 2900 cm^{-1} indicated that the sand contained neither chemically bound water of hydration nor adsorbed water. Figure 5.3 shows the Raman spectrum of magnesium perchlorate hexahydrate taken at the same conditions. The series of peaks at wavenumbers less than 1500 cm^{-1} were due to the perchlorate ion Raman vibrational modes, while the peak near 3500 cm^{-1} was due solely to chemically bound water of hydration [*Patel et al*., 1983].

Figure 5.4 displays normalized measured Raman spectra of liquid water at 5°C, water ice at -40°C, as well as the O-H spectral features of chabazite and magnesium perchlorate hexahydrate. The most prominent differences in the Raman spectral features were a broadening of the O-H peak between perchlorate hydrate and adsorbed water, and a further broadening between adsorbed water and liquid water. The spectrum of water ice included a distinct peak at 3150 cm^{-1}.

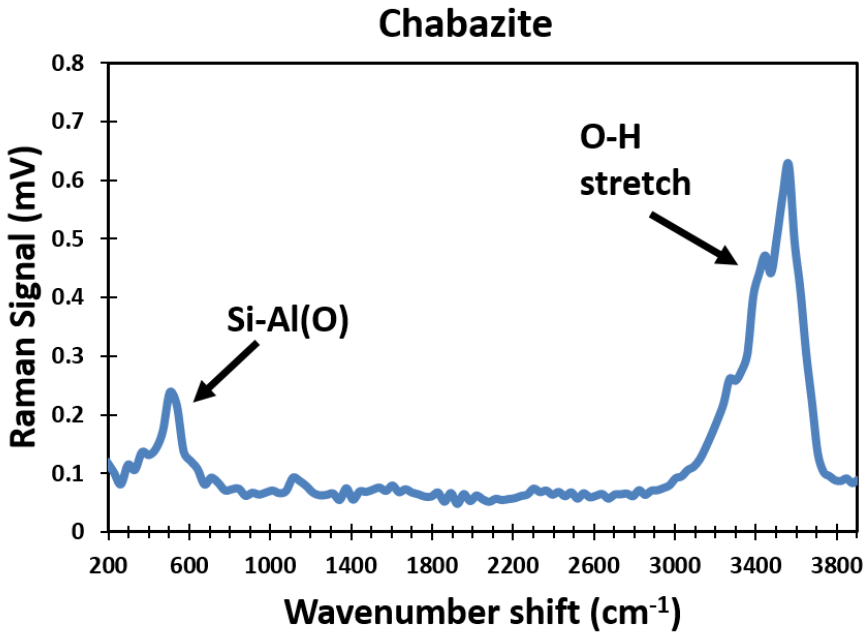

Figure 5.1. Measured Raman spectrum of chabazite with adsorbed water.

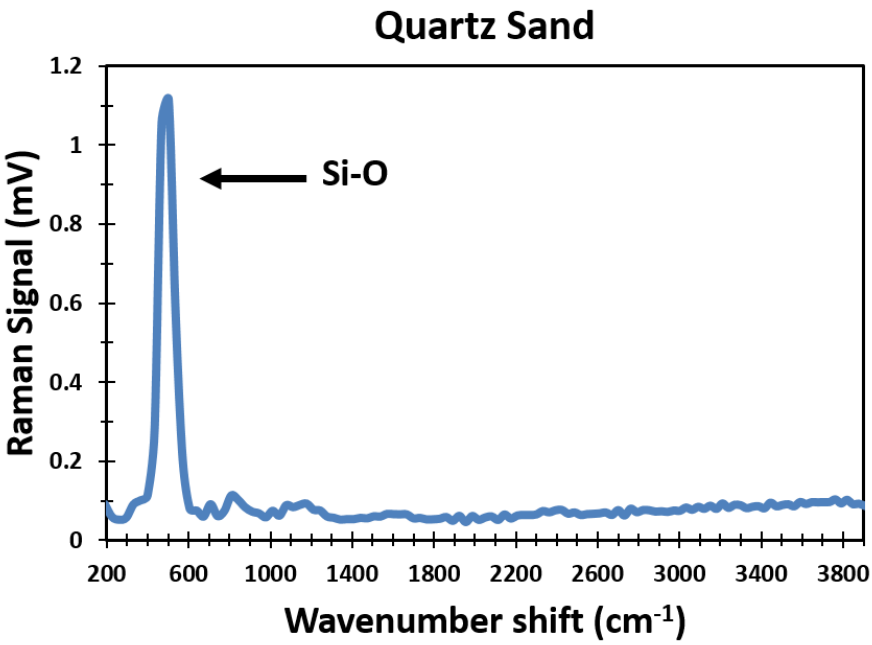

Figure 5.2. Measured Raman spectrum of quartz sand.

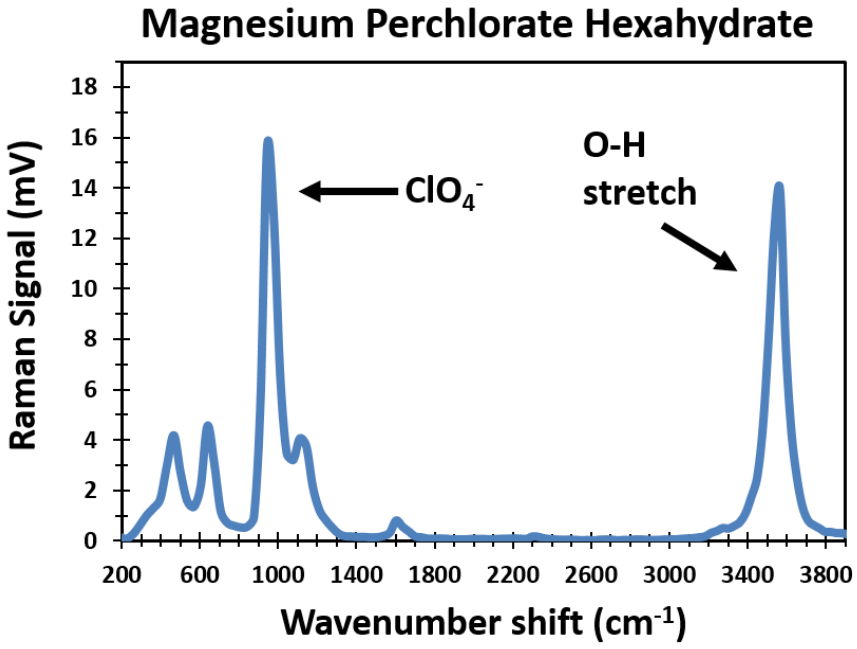

Figure 5.3. Measured Raman spectrum of dry magnesium perchlorate hexahydrate.

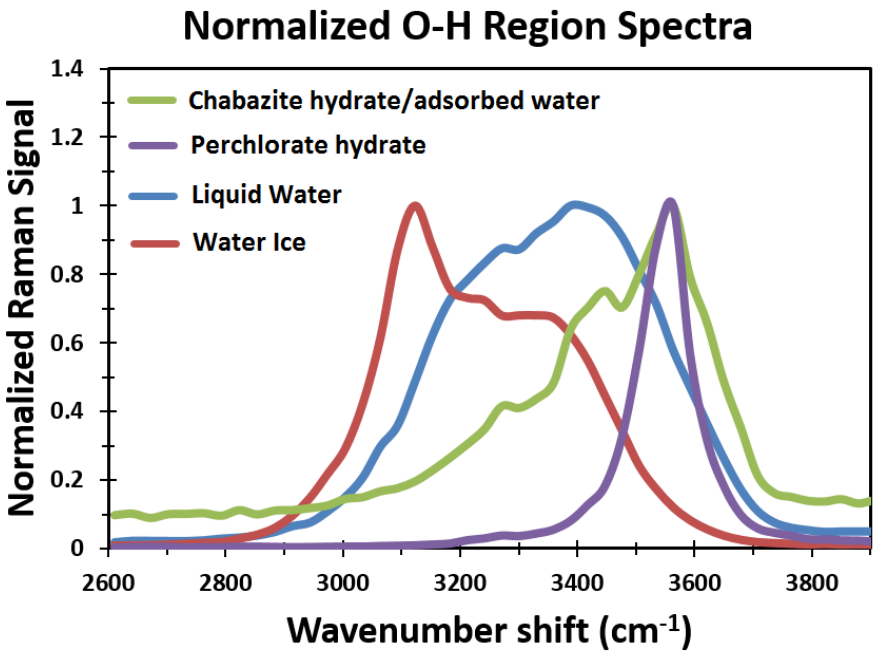

Figure 5.4. Normalized Raman spectra of liquid water, water ice, chabazite hydrate/adsorbed water, and perchlorate hydrate over the O-H stretch region.

5.3.2 Detection of Water and Carbon Dioxide Adsorption

To study the adsorption properties of chabazite, three experiments were carried out using the same zeolite sample. In the first experiment, the water vapour partial pressure inside the environmental chamber was set to and maintained at 4.0 Pa (corresponding to a frost point temperature of -50°C), in the second it was maintained at 2.1 Pa (-55°C frost point temperature), and in the third at 0.5 Pa (-65°C frost point temperature). The total pressure inside the chamber was 800 Pa in all three cases. For each experiment, the temperature of the sample plate was lowered in increments of 25°C (temperatures of 20°C, -5°C, -30°C, -55°C, and -80°C) and each temperature was

maintained for one hour. A Raman spectrum was recorded at the end of each hour, resulting in a total of 5 chabazite spectra for each of the three water vapour partial pressures. These experiments were focused on three main Raman spectral regions of interest: the silicate/aluminosilicate mineral region near 500 cm^{-1}, the O-H stretch Raman region above 2900 cm^{-1} which tracked changes in water content, and the Raman region at 1400 cm^{-1} which indicated the presence of adsorbed carbon dioxide [*Angell, C.*, 1973].

To determine the ability of Raman spectroscopy to detect the uptake of adsorbed water, spectra of chabazite measured at 4.0 Pa of water vapour partial pressure were first compared to those of quartz sand (SiO_2), a poorly adsorbing mineral, under the same environmental conditions. Figure 5.5a shows measured Raman spectra of quartz sand at temperatures of 20ºC, -5ºC, -30ºC, -55ºC, and -80ºC. The peak below 500 cm^{-1} corresponds to silicon-oxygen bonding. The Raman intensity of this peak remained unchanged at varying temperatures which was expected for spectral features corresponding to mineral structure. The O-H spectral region above 2900 cm^{-1} also showed no significant changes in the signal level, indicating that there were no changes in the adsorbed water content as the temperature was decreased. Figure 5.6a shows Raman spectra of chabazite taken over the same range of temperatures. As with the silicate peak of quartz sand, the aluminosilicate peak near 500 cm^{-1} remained unchanged throughout the experiment. In contrast to this, the Raman signal in the O-H region of the chabazite spectrum above 2900 cm^{-1} increased substantially as the temperature was lowered, indicating that the chabazite sample readily adsorbed water from the atmosphere. While frost formation on the sample was a possibility once the temperature of the sample plate dropped below the frost point temperature of -50ºC, the presence of water ice was not

identified in either set of Raman spectra. The surface area of the exposed sample plate was much larger than that of the sample and this resulted in frost forming in thin, spread out patches rather than directly on the sample. The lack of features in the Raman shifted region near 1400 cm^{-1} indicated that adsorbed carbon dioxide was also not present in either set of Raman spectra obtained during this experiment. Figures 5.5b and 5.6b show visual images of quartz sand and chabazite at temperatures of 20ºC, -30ºC, and -80ºC taken during the experiment with 4 Pa of water vapour partial pressure. In both cases, there were no changes observed in the appearance of the samples, indicating that the adsorption of water did not produce identifiable visual changes to the sample of chabazite.

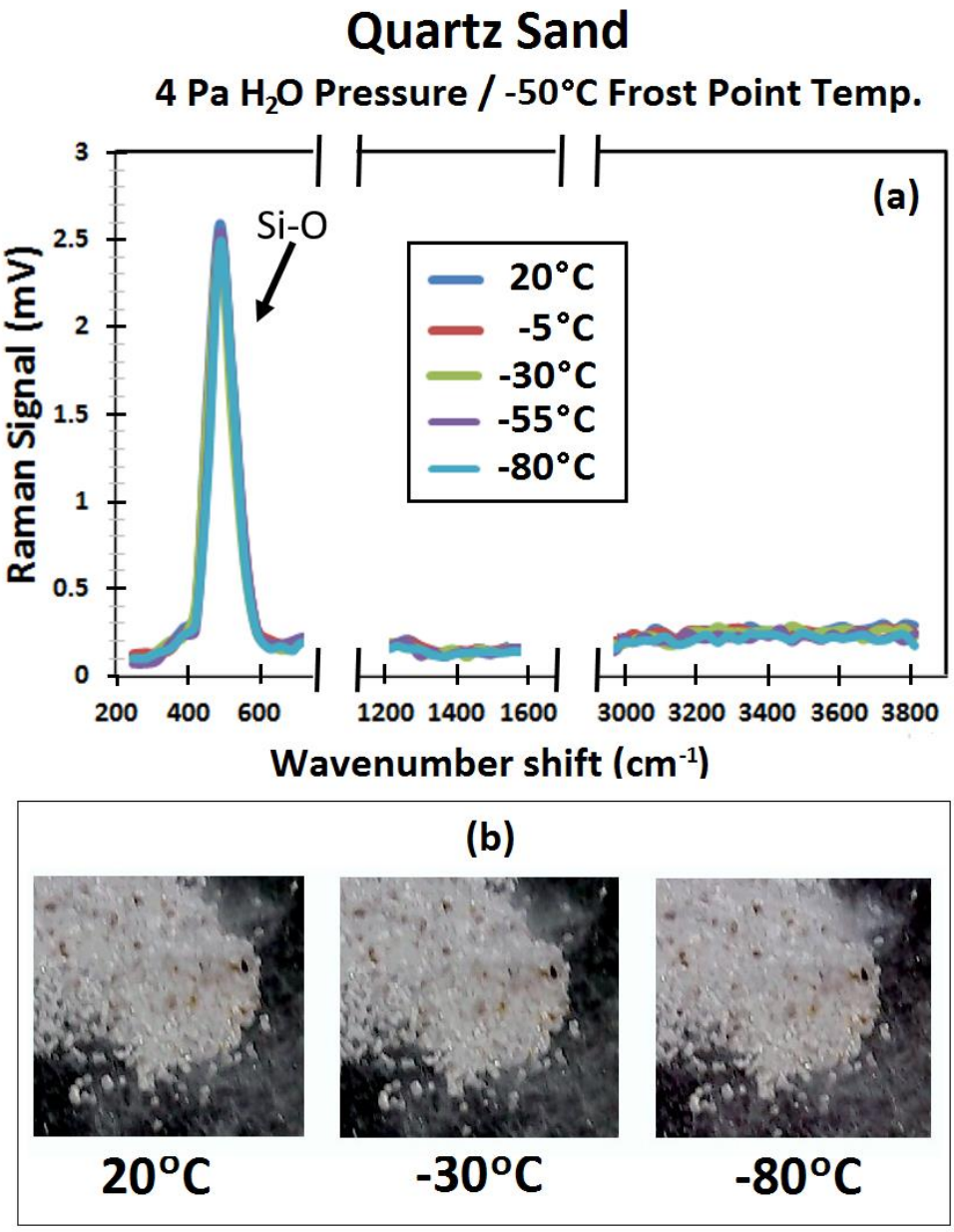

Figure 5.5. (a) Raman spectra of quartz sand over the temperature range of 20ºC to -80ºC. **(b)** Visual images of quartz sand at 20ºC, -30ºC, and -80ºC.

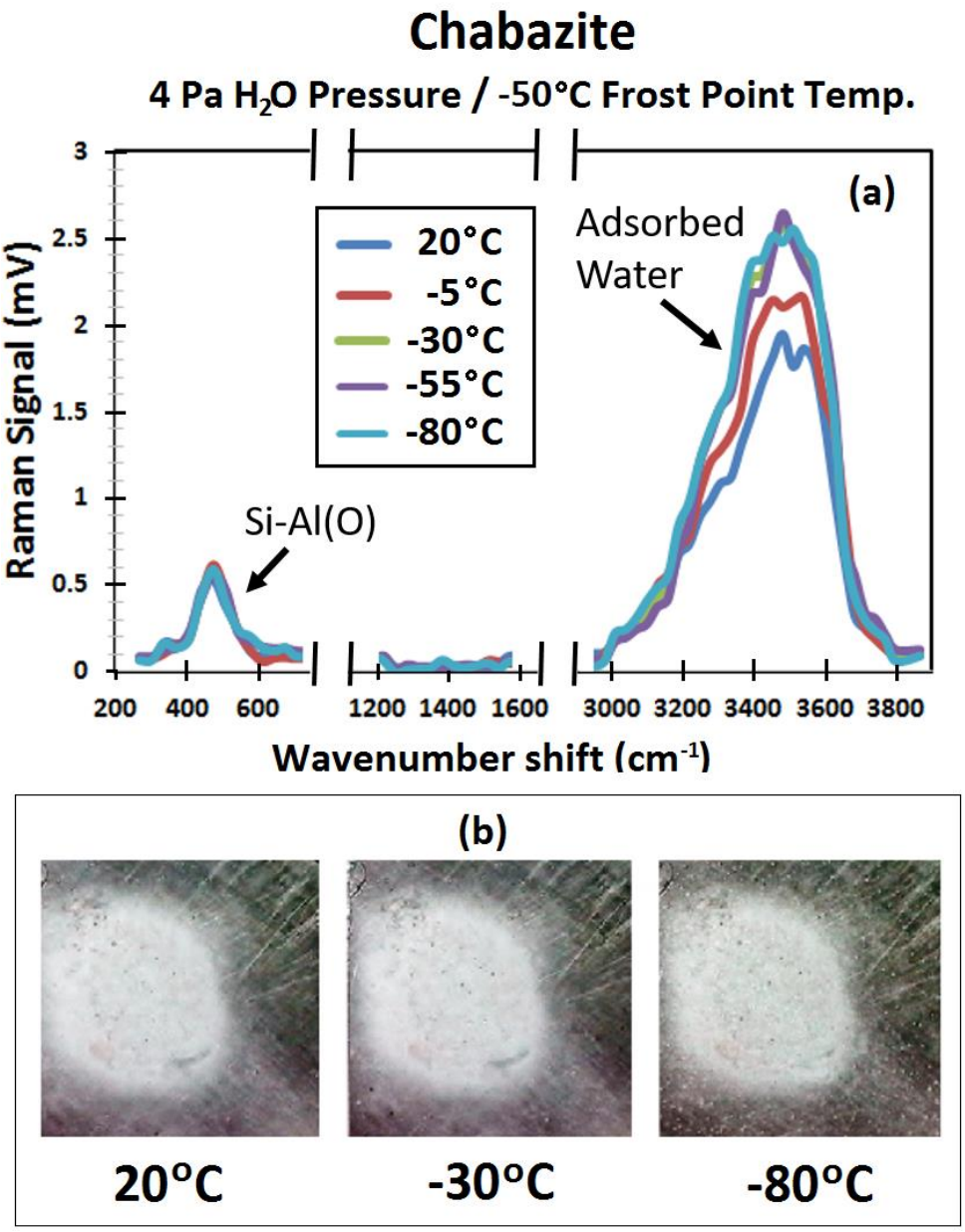

Figure 5.6. (a) Raman spectra of chabazite over the temperature range of 20°C to -80°C. The O-H stretch region increased in intensity between 20°C and -30°C, indicating that water was adsorbed by the sample. **(b)** Visual images of chabazite at the same temperatures.

Figures 5.7a and 5.7b show Raman spectra of the same chabazite sample measured at temperatures of 20ºC, -5ºC, -30ºC, -55ºC, and -80ºC for water vapour partial pressures of 2.1 Pa and 0.5 Pa respectively. These values of water vapour pressure were chosen to match daytime measurements with the original and updated calibrations of the Thermal and Electrical Conductivity Probe (TECP) on board the Mars Phoenix lander [*Zent et al.,* 2010; *Zent et al.,* 2016]. In both experiments, the aluminosilicate Raman peak near 500 cm^{-1} maintained the same intensity level over the full range of temperatures.

The O-H Raman region shows several interesting features. In both cases, the signal intensity increased with decreasing temperature, corresponding to increasing relative humidity. At each temperature, the O-H signal was stronger in the wetter 2.1 Pa case (Fig. 5.7a) than the drier 0.5 Pa case (Fig. 5.7b), indicating that more water had been adsorbed. In the 2.1 Pa experiment (Fig. 5.7a), increases in the Raman signal occurred between temperatures of 20ºC and -30ºC and the zeolite sample then became saturated with water as indicated by the lack of further signal increase in the -55ºC and -80ºC Raman spectra. This demonstrated that the adsorption occurred only at temperatures above -30ºC and the sample was then saturated with water at temperatures below -30ºC. In the 0.5 Pa experiment (Fig. 5.7b), increases in the Raman signal were observed between temperatures of 20ºC and -55ºC and no further changes were observed in the -80ºC spectrum. In this case, adsorption occurred at temperatures above -55ºC and the zeolite sample was saturated at temperatures below -55ºC. The adsorbed water Raman spectra did not display any evidence of freezing (by comparison with Fig. 5.4) throughout the experiments, indicating that it remained in a liquid-like state at temperatures down to -80ºC. This contrasts with perchlorate solution, which in the experiments of Chapter 4 was

found to freeze at the eutectic temperature. This was evidenced by a distinct water ice peak at 3150 cm^{-1} in the Raman spectrum (Fig. 4.4), which was not observed in the case of pure chabazite with adsorbed water (Fig. 5.7).

There was no evidence of CO_2 adsorption in the experiments with higher water vapour partial pressures of 4 Pa (Fig. 5.6a) and 2.1 Pa (Fig. 5.7a). However, when the temperature was lowered to -5^oC in the experiment with a water vapour partial pressure of 0.5 Pa, a distinct peak appeared in the Raman spectrum at 1400 cm^{-1} (Fig. 5.7b). This corresponded to CO_2 that had been adsorbed on the chabazite grains. To illustrate these changes more clearly, Figs. 5.8a and 5.8b show the ratio of the O-H and CO_2 Raman peaks to the invariant aluminosilicate peak over the range of five temperatures for the 2.1 Pa and 0.5 Pa cases.

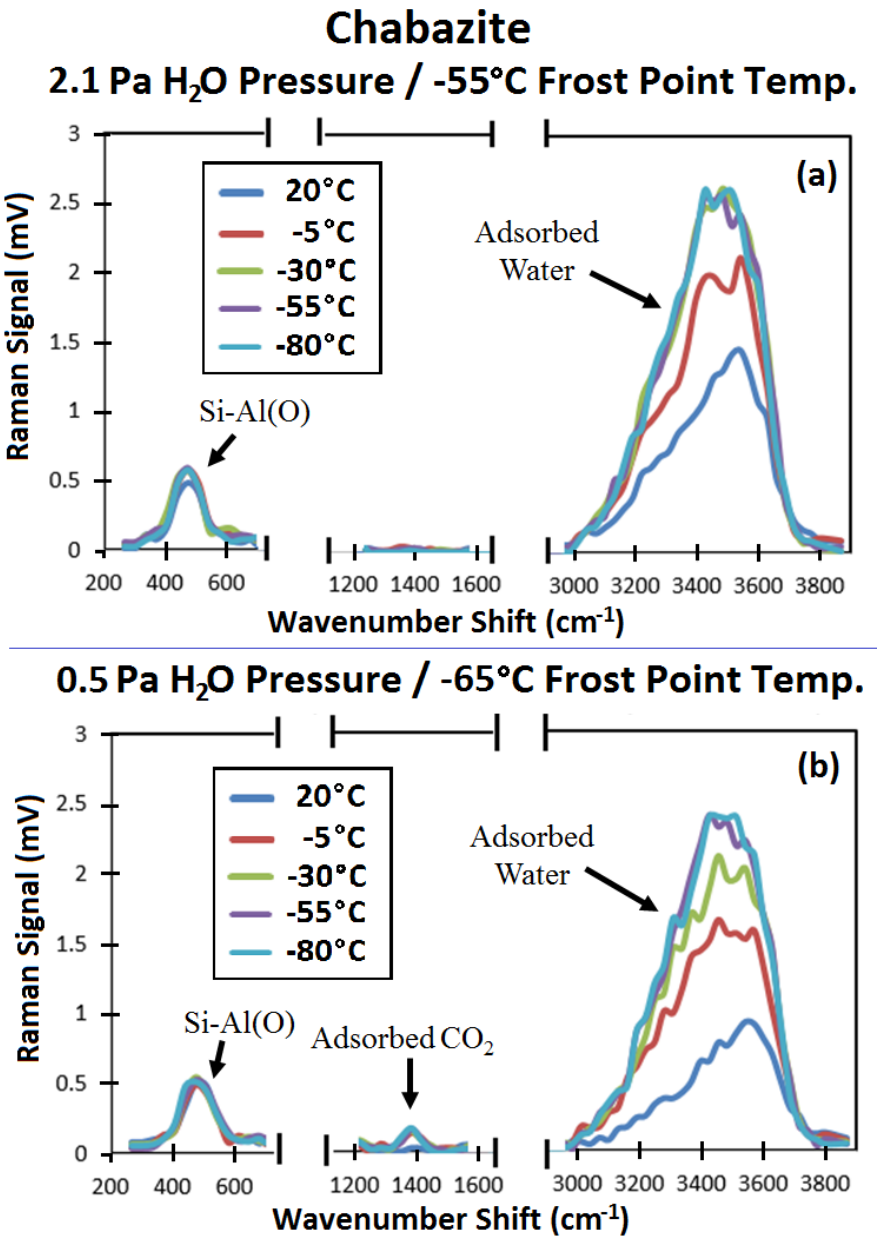

Figure 5.7. (a) Raman spectra of chabazite over the temperature range of 20°C and -80°C with a partial pressure of water vapour of 2.1 Pa. **(b)** Raman spectra of chabazite over the same temperature range with a partial pressure of water vapour of 0.5 Pa. Unlike the wetter case, a distinct peak appeared near 1400 cm^{-1} as the temperature was lowered to -5°C, indicating that carbon dioxide was also adsorbed.

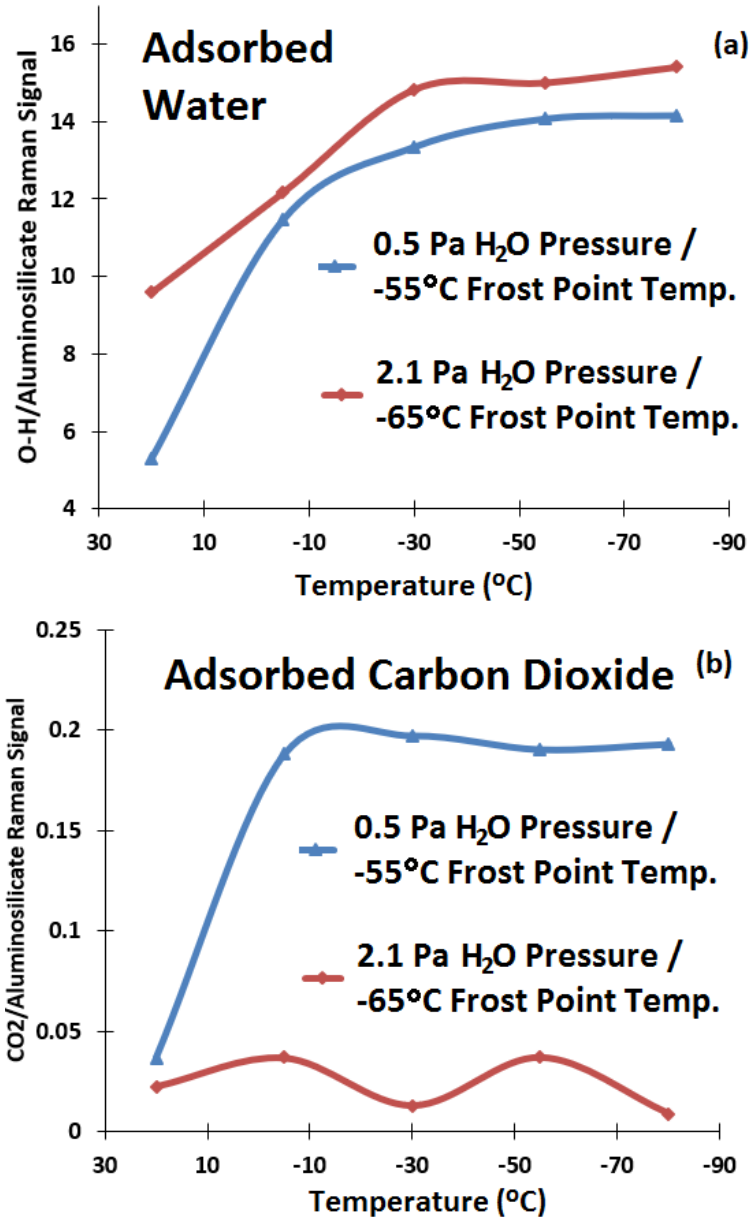

Figure 5.8. (a) Ratio of the O-H stretch peak to the aluminosilicate peak as a function of temperature. **(b)** Ratio of the CO_2 peak to the aluminosilicate peak as a function of temperature.

5.3.3 Combined Water Adsorption and Deliquescence

The goals of the second experiment were to examine the potential effect of adsorbed water on perchlorate deliquescence and to determine whether the deliquescence of perchlorate can produce the regolith darkening associated with Recurring Slope Lineae [*McEwen et al*., 2014] under Mars-relevant conditions. To achieve this, two distinct experiments were carried out using the same environmental conditions. One was conducted using a mixture of 95% chabazite and 5% magnesium perchlorate hexahydrate by weight in order to present an extreme case in which there was a significant amount of adsorbed water present on the surface mineral grains. The other used a mixture of 95% quartz sand and 5% magnesium perchlorate hexahydrate in order to present a case where the amount of adsorbed water was negligible. The water vapour partial pressure inside the chamber was maintained at 2.1 Pa (-55^{o}C frost point temperature) during these two experiments. This value of water vapour pressure was chosen so that the zeolite sample was saturated with adsorbed water at temperatures below -40^{o}C and thus ensured that any changes observed in the Raman signal below this temperature were due only to the deliquescence of perchlorate.

The mixture of quartz sand and magnesium perchlorate was examined first to provide a comparison case in which there was no adsorption of water. A Raman spectrum was first measured at 20^{o}C (Fig. 5.9a spectrum A). The temperature was then lowered to -44^{o}C (29% relative humidity over ice) and maintained for 2 hours to verify that there was no adsorbed water before a second Raman spectrum was acquired (Fig. 5.9a spectrum B). The temperature was then decreased from -45^{o}C to -53^{o}C at a rate of 1^{o}C per 10 minutes (similar to the rate of change observed in the evening at the Phoenix site) while the Raman

signal at a shift of 3250 cm^{-1} was monitored in order to track any changes in liquid water content (Fig. 5.11). This followed the method applied in Chapter 4 for pure magnesium perchlorate hexahydrate. After deliquescence was triggered, the temperature was maintained at -53°C (77% RHi) for 2 hours to allow for complete deliquescence of the perchlorate before a final Raman spectrum was measured (Fig. 5.9a spectrum C). The temperature of the sample plate was kept above the frost point temperature during this experiment to avoid the potential influence of frost and ensure that any observed changes were due only to deliquescence and adsorption. The experiment was then repeated using a 5% mixture of magnesium perchlorate hexahydrate and chabazite under the same environmental conditions (Fig. 5.10a and Fig. 5.11) to investigate whether adsorbed water would have an effect on deliquescence.

Figures 5.9a and 5.10a show Raman spectra of the perchlorate/sand and perchlorate/chabazite mixtures at 20°C (prior to significant water adsorption), -44°C (following maximum water adsorption), and at -53°C (following complete deliquescence) respectively. In both cases, the mineralogy Raman features below 1500 cm^{-1}, which were associated with the silicate/aluminosilicate and perchlorate ion bonding, remained unchanged. In the case of the perchlorate/sand mixture (Fig. 5.9a), no water adsorption was observed as the temperature was lowered from 20°C to -44°C (Fig. 5.9a spectra A and B), however the spectrum in the O-H region above 2900 cm^{-1} broadened significantly once deliquescence was triggered and a liquid perchlorate brine/sand mixture formed (Fig. 5.9a spectrum C). In the case of the chabazite/perchlorate mixture (Fig. 5.10a), water was adsorbed as the temperature was lowered from 20°C to -44°C (Fig. 5.10a spectra D and E) as indicated by a broadening of the O-H region. Once deliquescence was triggered, the

O-H region broadened further, indicating the addition of liquid perchlorate brine within the chabazite sample (Fig. 5.10a spectrum F). Visual images (Figs. 5.9b and 5.10b) were taken over the same temperature range. The bright perchlorate/quartz sand patch remained unchanged (Fig. 5.9b panels A and B) until the perchlorate underwent deliquescence at the 60-minute mark (Fig. 5.11), at which point the sample was observed to begin darkening. At the 180-minute mark, 2 hours after deliquescence was triggered, significant visual darkening of the sample had occurred (Fig. 5.9b panel C). Similarly, the perchlorate/chabazite mixture remained visually unchanged during water adsorption (Fig. 5.10b panels D and E), but had darkened substantially at the 180-minute mark, 2 hours after the deliquescence relative humidity was reached (Fig. 5.10b panel F).

Figure 5.11 displays the Raman signal at a shift of 3250 cm^{-1}, corresponding to changes in liquid water content, over time for both the perchlorate/sand mixture (green) and the perchlorate/chabazite mixture (red). In both cases, an increase in the Raman signal was found to begin at the 60-minute mark when the temperature was lowered to -51ºC and the magnesium perchlorate deliquescence relative humidity (DRH) of 60% was reached. This indicated that deliquescence was triggered at the same time in both samples, unaffected by the presence of adsorbed water. The DRH observed in these experiments was consistent with the results previously found in Chapter 4 for pure magnesium perchlorate hexahydrate. In the case of the perchlorate/quartz sand mixture, the 3250 cm^{-1} Raman signal reached a plateau at the 140-minute mark (80 minutes after the onset of deliquescence), indicating that deliquescence of the perchlorate within the sample had reached an equilibrium (the vapour pressure of the solution was equal to the partial pressure of water vapour in the air and the rate of water molecules entering the solution

matched the rate of water molecules evaporating from surface of the solution). This occurred much more rapidly in the case of the perchlorate/chabazite mixture, with equilibrium being reached at the 100-minutes mark (40 minutes after the onset of deliquescence). This was attributed to the presence of adsorbed water in the sample having formed a solution with the perchlorate and deliquesced water and thus reducing the time to reach an equilibrium.

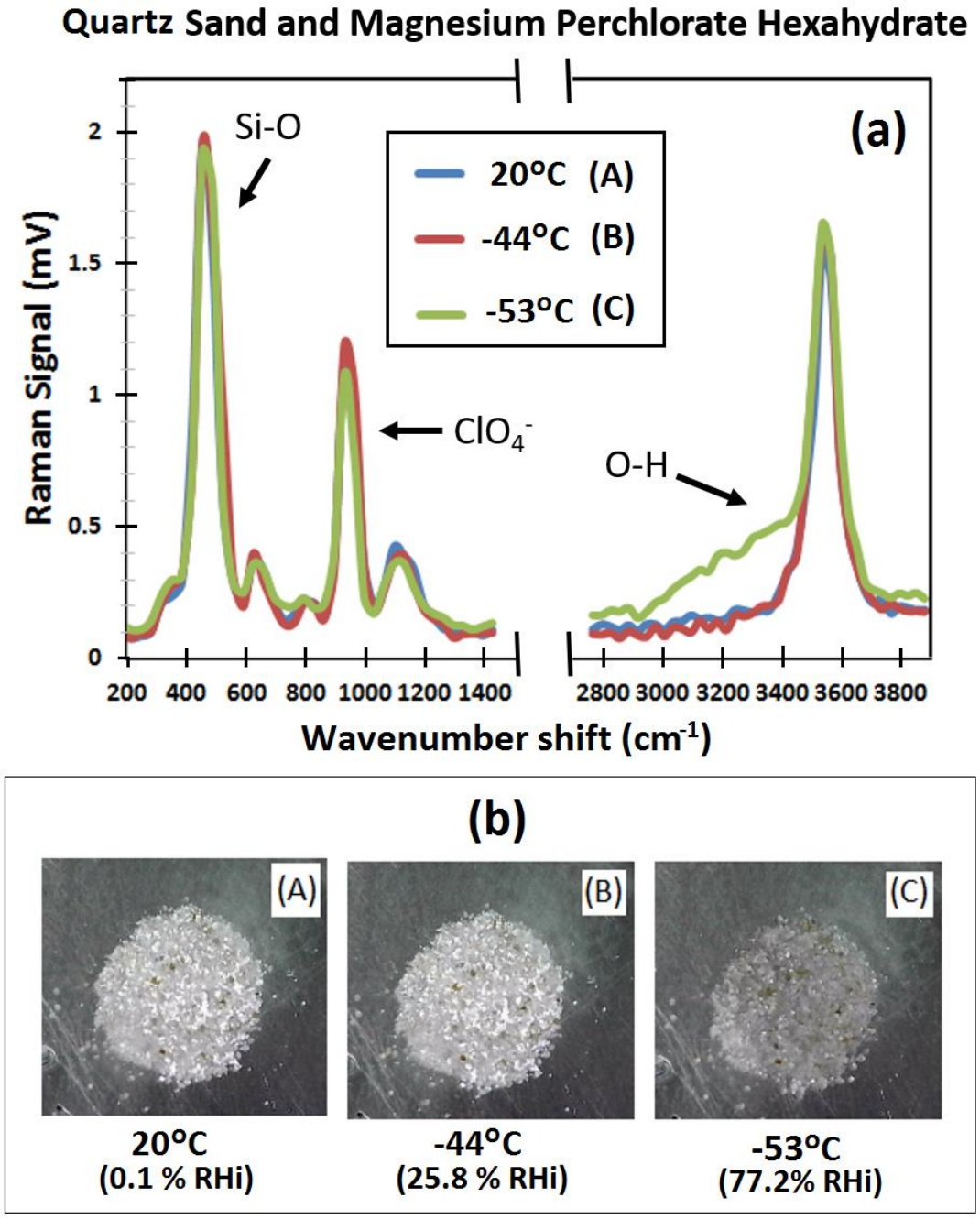

Figure 5.9. (a) Raman spectra of the quartz sand and perchlorate mixture at various temperatures. The O-H stretch region broadened in intensity only when the relative humidity was increased above the DRH and water was taken up by the sample. **(b)** Visual images of the mixture of quartz sand and perchlorate. Distinct darkening of the sample was visible once deliquescence occurred and liquid brine formed.

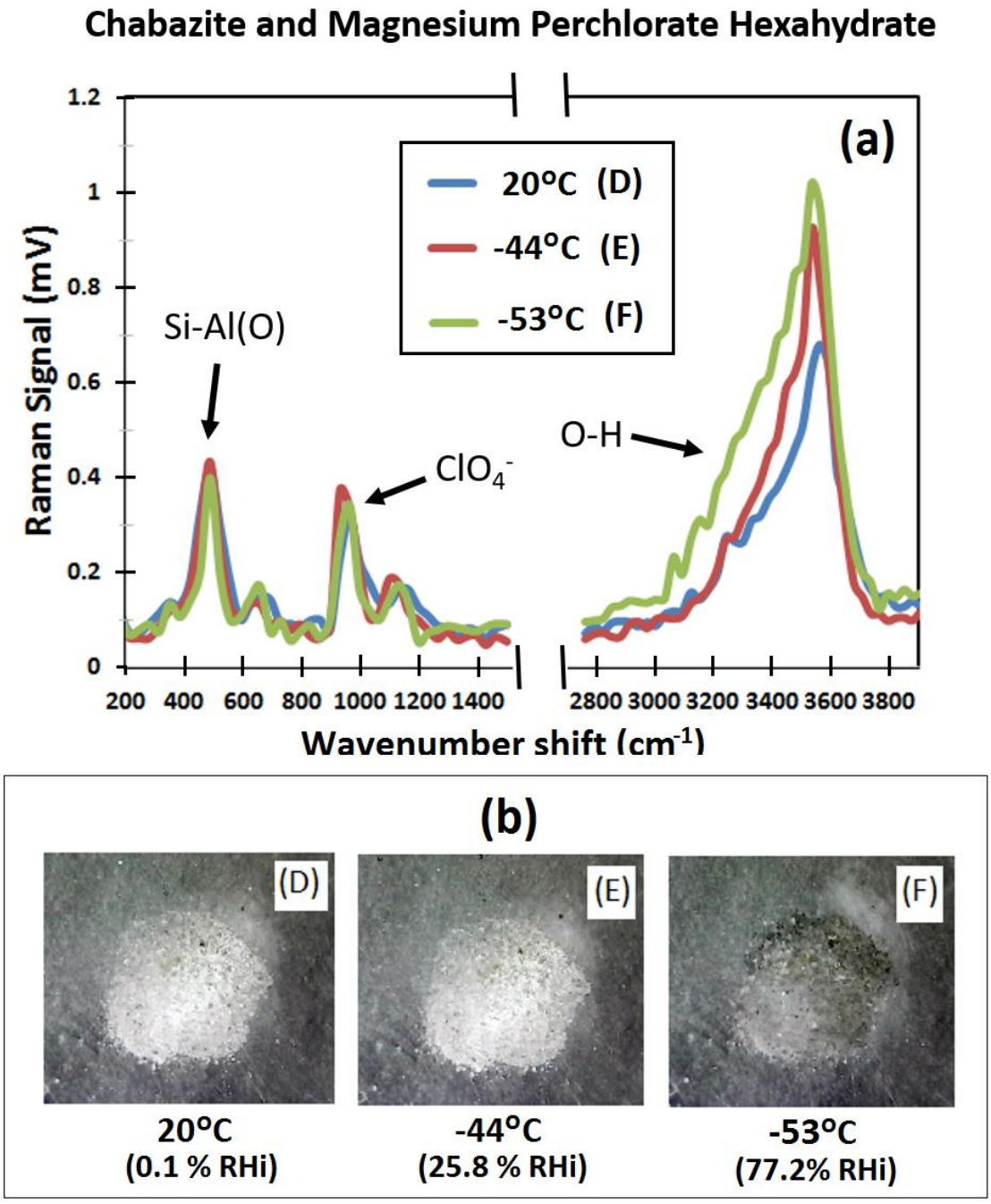

Figure 5.10. (a) Raman spectra of the chabazite and perchlorate mixture at various temperatures. **(b)** Visual images of the mixture of chabazite and perchlorate. There were no visual changes as water was adsorbed, but significant darkening was apparent following deliquescence.

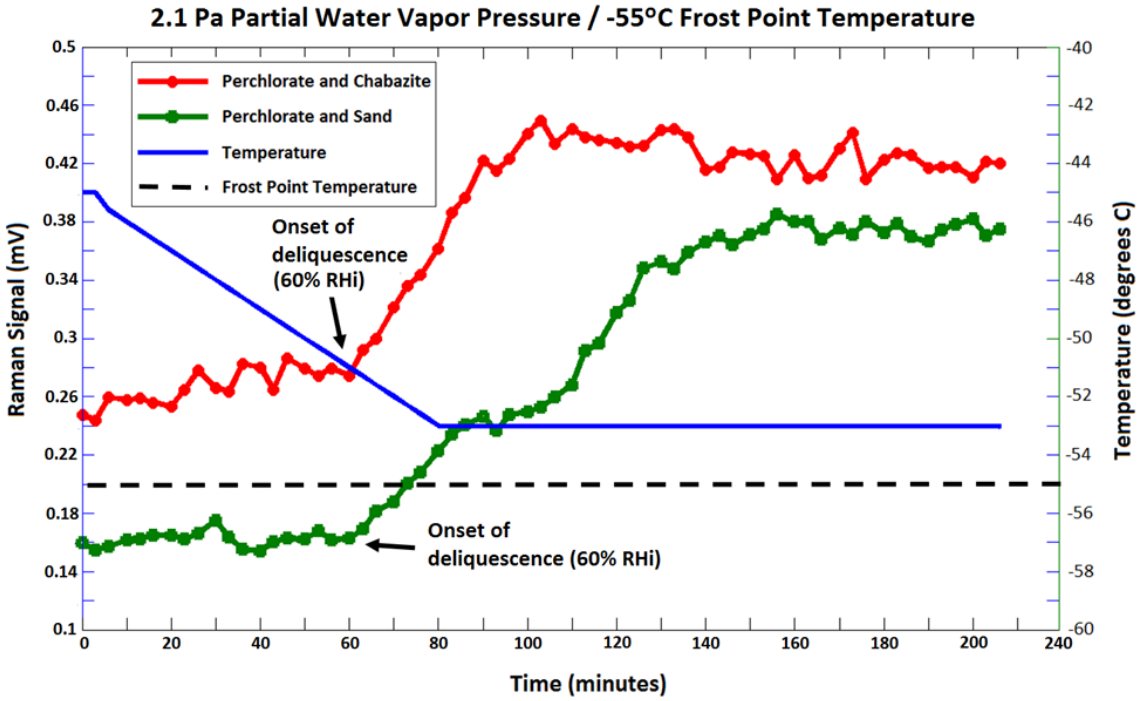

Figure 5.11. Measured Raman signal at a wavenumber shift of 3250 cm^{-1} for a perchlorate and chabazite mixture (red) and a perchlorate and quartz sand mixture (green) while the relative humidity was increased above the deliquescence relative humidity (DRH). In both cases, water uptake began at the 60-minute mark as deliquescence was triggered when the temperature reached -51°C (60% RHi).

5.4. Discussion

5.4.1 Adsorption of H_2O and CO_2

While each temperature of the chabazite sample in Sec. 5.3.2 (Figs. 5.6 and 5.7) was maintained for an hour, the O-H Raman signal typically reached a steady equilibrium value within 45 minutes of a new temperature being set. Thus, unlike previous experiments with clays and palagonites [*Zent et al*., 2001; *Janchen et al.,* 2009], the kinetics of water adsorption by zeolites was rapid enough to influence the diurnal water cycle on Mars.

The water vapour partial pressure of 2.1 Pa used in Sec. 5.3.2 (Fig. 5.7a) corresponded to the first published daytime humidity values measured by the Phoenix Thermal and Electrical Conductivity Probe (TECP) [*Zent et al.*, 2010]. In this case, the chabazite reached its adsorbed water capacity before reaching a temperature of -30ºC. Water adsorption by chabazite was unlikely to have a substantial effect on the diurnal water cycle with a daytime water vapour pressure of 2.1 Pa at that site since the modelled surface temperature rarely exceeded -25ºC during the Phoenix mission [*Zent et al.,* 2010]. The experiments in Chapter 4 demonstrated that deliquescence of perchlorate salt could instead play a major role under those conditions, a result which was further confirmed by the regolith-perchlorate mixture experiments of Sec. 5.3.3.

Experiments were also conducted with a water vapour partial pressure of 0.5 Pa, since that corresponded to the summer daytime humidity in the recalibrated TECP data [*Zent et al.*, 2016]. In this case (Fig. 5.7b), water continued to be adsorbed by the chabazite sample between temperatures of -30ºC and -55ºC. *Zent et al.* [2016] identified a daily "stability window" between 18:00h and 20:00h in which the water vapour pressure at the

Phoenix site decreased significantly as the temperature dropped from about -30ºC to -60ºC. This drop in the water vapour pressure was attributed to adsorption by the surface [*Zent et al,* 2016] and the experimental results reported here are consistent with that hypothesis, if zeolites were present at the site.

When the temperature and water vapour pressure were sufficiently low, carbon dioxide was also adsorbed by the chabazite sample (Fig. 5.7b), indicating that zeolites in the surface material can presently provide a reservoir of both adsorbed H_2O and CO_2. In the case of chabazite, the adsorption of water was found to restrict the adsorption of carbon dioxide, since adsorbed CO_2 was detected in the experiment with the lower water vapour pressure of 0.5 Pa, but not in the experiments with the higher water vapour pressures of 4 Pa (Fig. 5.6) and 2.1 Pa (Fig. 5.7a). This limiting effect had been suggested to occur on Mars based on energetic calculations [*Janchen et al.,* 2007], but was not previously observed experimentally for palagonite under Mars relevant conditions [*Zent et al.*, 1995]. This result leads to the question of whether carbonate can be formed in present Mars conditions due to the simultaneous adsorption of H_2O and CO_2 or the contact between atmospheric CO_2 and deliquesced water. These carbonate formation mechanisms have been observed under higher concentrations in Earth carbon sequestration applications [*Galhotra et al.,* 2009; *Giammar et al.,* 2005]. The study of this potential carbonate formation mechanism was beyond the scope of this dissertation, but should be the focus of further experimental investigations (see Sec. 7.2.1).

5.4.2 Darkening of Perchlorate-Regolith Mixtures and Recurring Slope Lineae

The dark streaks on surface slopes, referred to as recurring slope lineae (RSL), that are observed on Mars have recently been interpreted as flowing water [*Chevrier and Rivera-Valentin* 2012; *Chojnacki et al.*, 2016]. One of the leading hypotheses for the source of liquid water is deliquescence of perchlorate salts [*Ojha et al.,* 2015]. The experiments of Sec. 5.3.3 have demonstrated that small amounts of perchlorate mixed with surface regolith material (both quartz sand and zeolite) produce a significant uniform darkening of the soil mixture during deliquescence under present Martian conditions.

Dry formation mechanisms have also recently been proposed for the formation of RSL, including rarefied gas-triggered granular flows [*Schmidt et al.,* 2017]. Even if RSL are formed through dry processes (consistent with the modelling results of Sec. 4.4), the presence of liquid water brines is still extremely likely at other locations on Mars. This is especially true at high northern latitudes during the summer season, where surface temperatures are frequently above the eutectic temperature of perchlorates, the relative humidity often surpasses the deliquescence relative humidity of perchlorates, and there is abundant water ice near the surface [*Smith et al.,* 2009]. These liquid brine formation mechanisms have been demonstrated in previous laboratory studies [*Fischer et al., 2016; Chapter 4 of this dissertation*]. Visual imaging of regolith darkening combined with Raman spectroscopic measurements would provide powerful evidence for the presence of liquid water during a landed mission.

5.4.3 Detection During a Landed Mission

It was demonstrated that Raman scattering spectroscopy provides an effective method for directly detecting the processes associated with surface-atmosphere water exchange on Mars. Features within the Raman spectra at lower wavenumber shifts can be used to identify unique mineralogy, while the O-H spectral region provides a means for detecting hydrated minerals, adsorbed water, liquid perchlorate brine solution, and water ice.

Chapter Six

Conclusions

A stand-off Raman lidar system and environmental simulation chamber were developed at York University to study the processes associated with the surface-atmosphere exchange of water on Mars. Experiments have investigated the phase changes of perchlorate salts and the adsorption of water and carbon dioxide by zeolites under environmental conditions relevant to Mars. This dissertation concludes by re-examining the three essential questions that were posed in Chapter 1.

1. Can Raman scattering spectroscopy be used to detect and discriminate between the different processes and minerals that are associated with the exchange of water between the atmosphere and the surface on Mars?

The experiments presented in Chapters 4 and 5 have demonstrated that Raman spectroscopy provides an effective method for directly detecting the processes associated with surface-atmosphere water exchange on Mars. Specifically, Raman spectral features at lower wavenumber shifts allowed for the identification of unique mineralogy such as perchlorate ions and zeolite aluminosilicate features, while the sensitivity of the O-H Raman modes allowed for the detection and discrimination of hydrated minerals,

adsorbed water, liquid perchlorate brine solution, and water ice. During a landed mission, monitoring of the O-H Raman signal over the course of a diurnal cycle would provide a clear indication of liquid brine film formation and freezing and/or the adsorption of water by surface regolith grains. This would be a particularly powerful technique when combined with complementary measurements such as temperature, humidity, or visual imaging of the surface. These spectroscopic measurements could be acquired with a Raman lidar instrument from a stand-off distance without the need for sample preparation or manipulation.

2. Are the processes of salt deliquescence and surface regolith water adsorption currently contributing to the hydrological cycle on Mars? If so, can these processes explain observations made by instruments on landed and orbiting missions to Mars?

The experiments of Chapter 4 showed that when exposed to the water vapour pressure and temperatures found at the Phoenix landing site, magnesium perchlorate hexahydrate samples of the size found on Mars began to undergo deliquescence at a temperature 4˚C above the frost point temperature (60% RHi). Significant water uptake from the atmosphere began to occur within minutes, indicating that bulk deliquescence is likely to occur on present-day Mars. Similarly, the experiments presented in Chapter 5 found that samples of chabazite adsorbed water from the atmosphere when exposed to the water vapour partial pressure and temperatures found on Mars. The time required to reach equilibrium was on the order of one hour. These results demonstrate that perchlorates and

zeolites in the surface regolith can contribute to the Martian hydrological cycle by absorbing and adsorbing water from the atmosphere and pre-emptively reducing the atmospheric water vapour pressure prior to 100% relative humidity being reached during the evening. These results help to explain the evening decrease in near-surface water vapour pressure that has been measured at multiple sites on Mars.

3. Can water presently exist on Mars in phases other than ice and vapour? If so, where and when is this water found on the surface of Mars?

Chapter 4 demonstrated that the deliquescence of magnesium perchlorate can produce liquid water brine solution under conditions found at the north polar Mars Phoenix site during the northern hemisphere summer. These solutions could exist for up to 3 hours in the evening and 2 hours in the morning.

Chapter 5 showed that zeolites can adsorb water over a wide range of temperatures and water vapour partial pressures presently found on Mars. Thus, unlike perchlorate brine which can only form for a maximum of a few hours a day, adsorbed water is likely to be loosely bound to surface material at all times on Mars at locations where zeolites are present.

While Chapter 5 showed that the deliquescence of perchlorate mixed within regolith can produce distinct visual darkening of surface material, the modelling results of Chapter 4 demonstrated that deliquescence is most probable to occur at high northern latitudes during the summer season. Most RSL have been observed to occur at equatorial latitudes, and these cannot be explained as being a result of deliquescence at the surface.

Chapter Seven

Future Work

7.1 Instrumental Improvements

7.1.1 Raman Lidar

The Raman scattering lidar used in these experiments employed an Nd:YAG laser with fourth harmonic output at a wavelength of 266 nm. This wavelength produced excellent Raman scattering from salts such as perchlorates and carbonates but resulted in weaker Raman scattering from the quartz sand and aluminosilicate zeolite samples. Attempts at measuring montmorillonite clay and JSC Mars-1, a palagonite tephra, failed to yield a detectable Raman signal. This was most likely due to the presence of iron in these two samples, which is known to strongly absorb ultraviolet light. Further experimental studies should be conducted to determine the optimal laser wavelength for a planetary mission Raman instrument. Challenges include light absorption by the regolith material at ultraviolet wavelengths, interference in the detection of Raman scattering due to fluorescence at visible wavelengths, and poor detector efficiency at infrared wavelengths.

7.1.2 Environmental Chamber

During all of the experiments presented in this dissertation, the atmosphere inside the environmental chamber was maintained by a continuous flow of fresh gas entering the chamber. This resulted in the atmospheric water vapour content remaining constant for the entirety of a given experiment. While this scenario is accurate for temperatures above the frost point, near surface water vapour is observed to decrease during the night-time hours on Mars. A more realistic humidity cycle is required to precisely determine what happens during the night-time and early morning hours on Mars. For example, to investigate whether the processes of surface frost formation, deliquescence, and adsorption can compete and inhibit each other from occurring and to examine how the sublimation of frost during the morning hours might influence deliquescence and adsorption.

7.1.3 Quantification of Water Uptake with Raman Measurements

Quantifying the amount of water deposited per unit area would be a crucial next step. This would require a means for calibrating the measurement such as comparison with Raman scattering from a known target. For example, it was found in the experiments of Chapter 5 that the Raman signal from the quartz sand substrate did not change as the Raman signal from the deliquesced water was increasing (Figure 5.9a). Experiments would need to be carried out to determine how the Raman signal responds to varying surface area, depth, and mass for samples of liquid water, water ice, and simulated Martian soil. A high accuracy scientific scale could be used to correlate the measured Raman

signal to changes in the sample mass under ambient laboratory conditions. Chamber measurements of perchlorate water uptake and brine formation under Mars conditions could then be compared to the signal response studies to provide a quantification of the water taken up by the sample.

7.1.4 Sample Temperature Measurement

The temperature measured during the experiments was provided by two resistance thermometers that were adhered to the surface of the sample plate on either side of the sample material. Measuring the true temperature of the sample would provide an extra layer of information during the experiments presented here. Deliquescence and adsorption are exothermic processes, therefore differences between the temperature of the sample plate and the sample material could be used to determine when a certain process is occurring. Direct measurements of the sample temperature would also allow for the potential heating of the sample material by the laser beam to be more accurately assessed. Such measurements could be made using an infrared radiation thermometer. Preliminary chamber tests using a Heitronics KT-19 infrared thermometer demonstrated that such an instrument could effectively measure temperature at the low-pressure conditions required for these experiments. Recent advances in infrared temperature sensing technology have resulted in instruments that are able to accurately measure temperatures as low as -100˚C.

7.2 Future Experimental Studies

7.2.1 Detection of Carbonate Formation

Chapter 5 demonstrated that chabazite can simultaneously adsorb water and carbon dioxide under environmental conditions found on Mars. Gas phase carbon dioxide was also able to interact with liquid water perchlorate solution. These scenarios could result in interesting chemistry, such as the formation of carbonate (CO_3^{2-}) or bicarbonate (HCO_3^-) salts. Future experiments should be aimed at investigating these potential reactions, as the active sequestration of atmospheric CO_2 into mineral phases could have significant implications for climate change on Mars [*Tomkinson et al.*, 2013]. Figure 7.1 shows measured Raman spectra of magnesium carbonate and calcium carbonate at temperatures of 25°C and -50°C in an atmosphere of 800 Pa of carbon dioxide. The major Raman peak at 1100 cm^{-1} falls near aluminosilicate and perchlorate ion Raman peaks in the chabazite and magnesium perchlorate Raman spectra, therefore special care would be required to identify small amounts of carbonate formation using the Raman method.

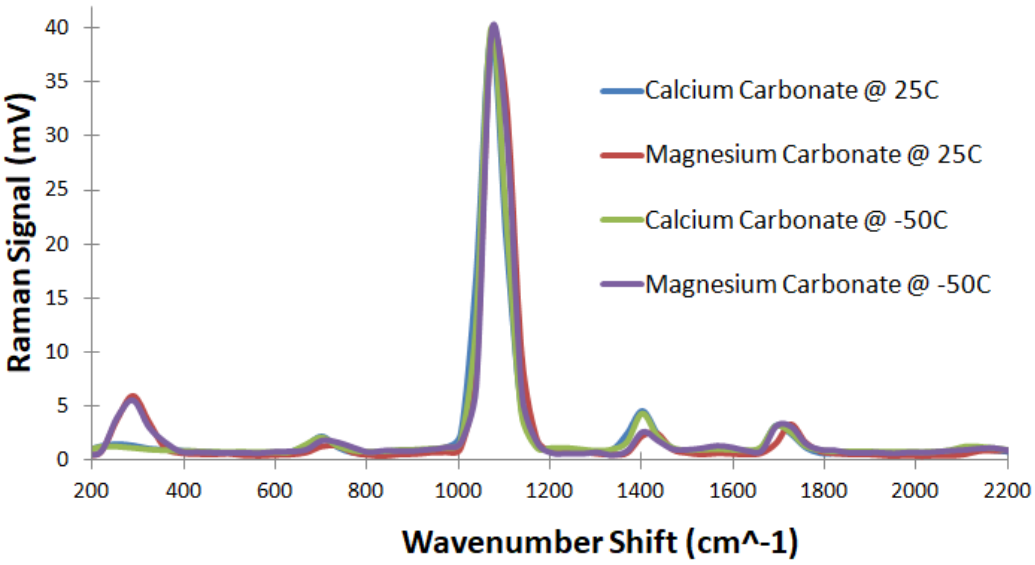

Figure 7.1 Raman spectra of calcium carbonate and magnesium carbonate in 800 Pa of CO_2 measured with the Raman lidar.

7.2.2 Studies of Mineral Hydration

Mineral hydration, a chemical reaction that results in water being added to the crystalline structure of a mineral, presents another possible mechanism in which the surface and atmosphere on Mars can exchange water. Most hydration reactions have very slow kinetics, however there is evidence that minerals such as sulfates can undergo rapid hydration and dehydration. Experiments should be carried out to examine whether such reactions are possible under Martian environmental conditions to assess the potential role of this process in the water cycle. Determining whether mineral hydration is an active process also has implications for the geological history of Mars, as the presence of hydrated minerals is often used as an indicator of past liquid water activity.

7.2.3 Perchlorate Migration Through the Regolith and Interaction with the Subsurface Ice Table

A vital next step in the perchlorate deliquescence experiments would be to examine the potential migration of perchlorate solutions through a realistic regolith column with a subsurface water ice table bottom boundary. Perchlorates are expected to form on the surface of Mars, therefore the downward movement of perchlorate through the regolith would represent a pathway for distributing perchlorate (and hence perchlorate solutions) to the Martian subsurface. This is important as the subsurface features much more moderate fluctuations in temperature as well as protection from the harmful ultraviolet radiation found at the surface and would therefore offer a much more hospitable environment for primitive life. Additionally, these experiments would help to determine if perchlorates have contributed to the growth of the subsurface water ice table e.g. through the emplacement of perchlorate solution at the regolith-ice table boundary. Studies of perchlorate on Earth have demonstrated that perchlorate solutions have a high potential for migrating through the soil since perchlorate is generally poorly adsorbed by soil minerals [*Urbanksy and Brown,* 2003].

A related experiment would be to examine how perchlorate would behave at the interface between the bottom of the surface regolith layer and the top of the subsurface ice table. This scenario could potentially result in a permanent layer of liquid water brine at the top of the ice table.

A robotic arm (OWI535 Robotic Arm Edge) was assembled and modified to operate remotely within the sealed environmental chamber (Fig. 7.2a). Preliminary testing demonstrated that the robotic arm was fully operational under Martian pressure

conditions. This type of arm could be applied to experimental investigations as in a mission scenario to push or scoop the upper layer of surface regolith material and allow the Raman instrument to measure the subsurface (Figs. 7.2b and 7.2c).

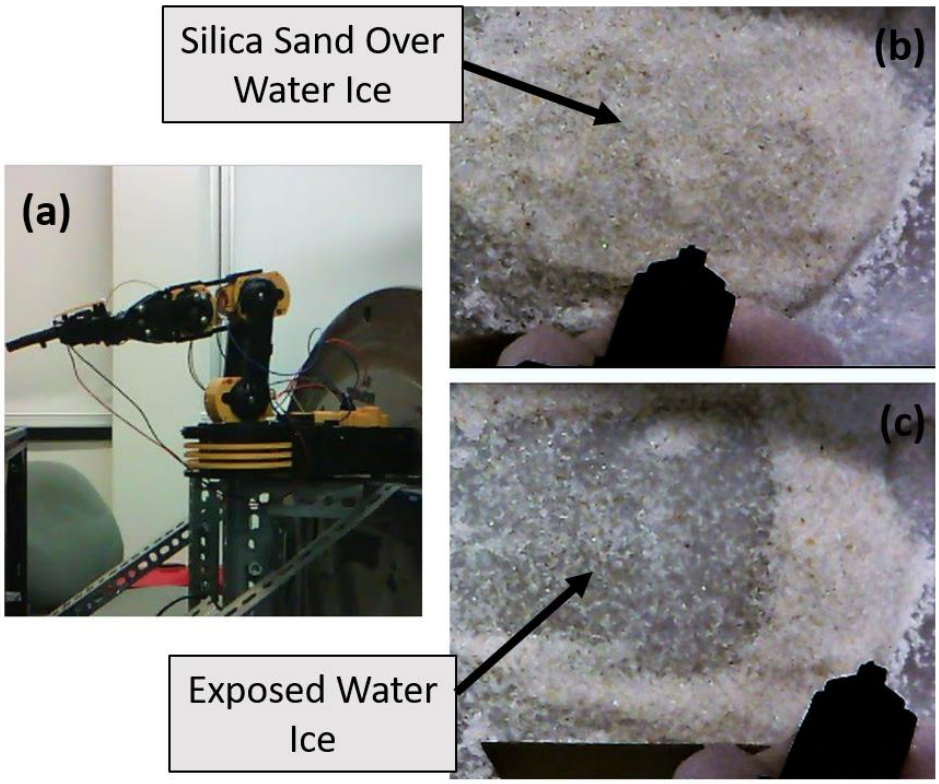

Figure 7.2 (a) Photograph of the robotic arm. **(b)** Photograph of the silica sand covered water ice prior to the robotic arm being used. **(c)** Photograph of the exposed water ice layer after the robotic arm moved the overlying silica sand.

Appendix A

Linear Spectral Unmixing of Raman Spectra

Given a set of measured Raman spectra of individual known pure substances (endmembers) and an aggregate measured Raman spectrum that is composed of several known components that have been sampled at the same discrete wavelength (or wavenumber shift) values, a mixture model can be posed with the following form.

$$X = A1*P1 + A2*P2 + A3*P3 + ... Am*Pm$$

Where

X is the aggregate measured Raman spectrum.

Pm is the measured Raman spectrum of the m^{th} pure substance.

Am is the non-negative relative contribution of the m^{th} pure substance Raman spectrum to the aggregate Raman spectrum, with A1+A2+A3+... = 1

This problem may be solved computationally by employing a non-negative linear least squares algorithm of the following form.

$X(Lx1) = P(LxM)A(Mx1)$

$F(A) = \min \| X(Lx1) - P(LxM)A(Mx1) \|^2 , A_m >= 0$

Where

L is the number of discrete sampled wavelength (or wavenumber shift) values.

M is the number of pure substance endmembers.

X(*Lx1)* is a Lx1 vector containing the measured aggregate Raman spectrum.

P(*LxM)* is an LxM matrix containing all of the measured pure substance Raman spectra.

A(*Mx1*) is a Mx1 vector containing the coefficients that minimize the norm(X*A-P)

subject to a >= 0.

F(A) is a vector that contains the computed coefficients A.

The spectral unmixing presented in Chapter 4 utilized the non-negative linear least squares Matlab function lsqnonneg. This algorithm is an application of the active set method that is detailed in *Lawson and Hanson* [1974].

While this method assumes that the Raman scattering efficiency of each endmember is the same, this is not generally the case. Therefore, this model should only be used as a first estimate towards determining the contribution from each endmember to the aggregate spectrum. A model that incorporates the Raman scattering cross-section of each endmember substance would provide a more accurate estimate of the relative contribution of each endmember to the aggregate spectrum.

References

Abbey, W.J., et al. (2017), Deep UV Raman spectroscopy for planetary exploration: the search for in situ organics, Icarus, 290.

Angell, C.L., et al. (1973), Raman spectroscopic investigation of zeolites and adsorbed molecules, The Journal of Physical Chemistry, 77(2), 222-227, doi:10.1021/j100621a015.

Archer, P. D., Jr. et al. (2014), Abundances and implications of volatile-bearing species from evolved gas analysis of the Rocknest aeolian deposit, Gale Crater, Mars, J. Geophys. Res. Planets, 119, 237–254, doi:10.1002/2013JE004493.

Arvidson, R. E., et al. (2009), Results from the Mars Phoenix Lander Robotic Arm experiment, J. Geophys. Res., 114, E00E02, doi:10.1029/2009JE003408.

ASTM E2529-06 (2014), Standard Guide for Testing the Resolution of a Raman Spectrometer, ASTM International, West Conshohocken, PA, 2014, www.astm.org

Beck, P., Pommerol, A., Schmitt, B., and Brissaud, O. (2010), Kinetics of water adsorption on minerals and the breathing of the Martian regolith, J. Geophys. Res., 115, E10011, doi:10.1029/2009JE003539.

Bevington, P.R. and Robinson, D.K. (1993), Data Reduction and Error Analysis for the Physical Sciences, McGraw-Hill, New York.

Bibring, J. P., et al. (2006), Global mineralogical and aqueous Mars history derived from OMEGA/Mars Express data. Science, 312(5772), 400-404.

Bodnar, R. J. (1993), Revised equation and table for determining the freezing point depression of H2O-NaCl solutions, Geochimica et Cosmochimica Acta, 57(3), 683-684.

Bolis, V. (2013), Fundamentals in adsorption at the solid-gas interface. Concepts and thermodynamics. In Calorimetry and thermal methods in catalysis (pp. 3-50). Springer, Berlin, Heidelberg.

Böttger, H. M., Lewis, S. R., Read, P. L. & Forget, F. (2005), The effects of the martian regolith on GCM water cycle simulations, Icarus, 177, 174-189, doi: 0.1016/j.icarus.2005.02.024.

Bowie, B. T. and Griffiths, P. R. (2003), Determination of the resolution of a multichannel Raman spectrometer using Fourier transform Raman spectra, Applied spectroscopy, 57(2), 190-196.

Boynton, W. V., et al. (2002). Distribution of hydrogen in the near surface of Mars: Evidence for subsurface ice deposits, Science, 297(5578), 81-85.

Bradley, M. (2007), Curve fitting in Raman and IR spectroscopy: basic theory of line shapes and applications, Application Note, 50733.

Buck, A. L. (1981), New equations for computing vapor pressure and enhancement factor, Journal of applied meteorology, 20(12), 1527-1532.

Carr, M. H. (1995), The Martian drainage system and the origin of valley networks and fretted channels, J. Geophys. Res., 100(E4), 7479–7507, doi:10.1029/95JE00260.

Carr, M. H. and Head, J. W. (2010), Geologic history of Mars. Earth and Planetary Science Letters, 294(3), 185-203.

Carrier, B. L. and Kounaves, S.P. (2015), The origins of perchlorate in the Martian soil, Geophys. Res. Lett., 42, 3739–3745. doi: 10.1002/2015GL064290.

Carter, J., F., Poulet, J.-P. Bibring, N. Mangold, and S. Murchie (2013), Hydrous minerals on Mars as seen by the CRISM and OMEGA imaging spectrometers: Updated global view, J. Geophys. Res. Planets, 118, 831–858, doi: 10.1029/2012JE004145.

Catling, D. C., et al. (2010), Atmospheric origins of perchlorate on Mars and in the Atacama, J. Geophys. Res., 115, E00E11, doi:10.1029/2009JE003425.

Chevrier, V. F., Hanley, J., and Altheide, T.S. (2009), Stability of perchlorate hydrates and their liquid solutions at the Phoenix landing site, Mars, Geophys. Res. Lett., 36, L10202, doi:10.1029/2009GL037497.

Chevrier, V. F. and Rivera-Valentin, E.G. (2012), Formation of recurring slope lineae by liquid brines on present-day Mars, Geophys. Res. Lett., 39, L21202, doi:10.1029/2012GL054119.

Chojnacki, M., et al. (2016), Geologic context of recurring slope lineae in Melas and Coprates Chasmata, Mars, J. Geophys. Res. Planets, 121, 1204–1231, doi:10.1002/2015JE004991.

Chou, I.-M. and R. R. Seal II (2007), Magnesium and calcium sulfate stabilities and the water budget of Mars, J. Geophys. Res., 112, E11004, doi:10.1029/2007JE002898.

Clugston, M., and Flemming, R. (2000), Advanced chemistry, Oxford University Press.

Cull, S., et al. (2010), Concentrated perchlorate at the Mars Phoenix landing site: Evidence for thin film liquid water on Mars, Geophysical Research Letters, 37, doi:10.1029/2010GL045269.

Cull, S., et al. (2014), Aqueous and non-aqueous soil processes on the northern plains of Mars: Insights from the distribution of perchlorate salts at the Phoenix landing site and in Earth analog environments, Planetary and Space Science, 96, 29-34, doi:10.1016/j.pss.2014.02.011.

Curran, R. J., et al. (1973), Mars: Mariner 9 spectroscopic evidence for H2O ice clouds, Science, 182, 381–383.

Cziczo, D. J. and Abbatt, J. P. D. (2000), Infrared observations of the response of NaCl, MgCl2, NH4HSO4, and NH4NO3 aerosols to changes in relative humidity from 298 to 238 K, The Journal of Physical Chemistry A, 104(10), 2038-2047.

Daerden, F., et al. (2015), A solar escalator on Mars: Self-lifting of dust layers by radiative heating, Geophysical Research Letters, 42(18), 7319-7326.

Davila, A.F., et al. (2010), Hygroscopic salts and the potential for life on Mars, Astrobiology, 10 (6), 617-628, doi:10.1089/ast.2009.0421.

Dickinson, C.D. (2008), Phoenix Meteorological Data, NASA Planetary Data System, PHX-M-MET-3-PT-RDR-V1.0, MS100RML_00905086235_1BB3M1.

Durickovic, I., et al. (2011), Water–ice phase transition probed by Raman spectroscopy, Journal of Raman Spectroscopy, 42, 1408-1412, doi:10.1002/jrs.2841.

Ehlmann, B. L., et al. (2009), Identification of hydrated silicate minerals on Mars using MRO-CRISM: Geologic context near Nili Fossae and implications for aqueous alteration, J. Geophys. Res., 114, E00D08, doi:10.1029/2009JE003339.

Eisenberg, D. and Kauzmann, W. (2005), The Structure and Properties of Water, Clarendon Press, Oxford.

Erdem, E., et al. (2004), The removal of heavy metal cations by natural zeolites, Journal of colloid and interface science, 280(2), 309-314.

Fassett, C. I. and Head, J. W. (2008), The timing of martian valley network activity: Constraints from buffered crater counting, Icarus, 195(1), 61-89.

Fischer, E., et al., (2014), Experimental evidence for the formation of liquid saline water on Mars, Geophysical Research Letters, 41, 4456-4462, doi:10.1002/2014GL060302.

Fischer, E., Martínez, G. M., and Rennó, N. O. (2016), Formation and Persistence of Brine on Mars: Experimental Simulations throughout the Diurnal Cycle at the Phoenix Landing Site. Astrobiology, 16(12), 937-948.

Galhotra, P., et al. (2009), Carbon dioxide (C16O2 and C18O2) adsorption in zeolite Y materials: effect of cation, adsorbed water and particle size, Energy & Environmental Science, 2(4), 401-409, doi:10.1039/B814908A.

Giammar, D.E., et al. (2005), Forsterite dissolution and magnesite precipitation at conditions relevant for deep saline aquifer storage and sequestration of carbon dioxide, Chemical Geology, 217(3), 257-276, doi:10.1016/j.chemgeo.2004.12.013.

Glavin, D.P., et al. (2013), Evidence for perchlorates and the origin of chlorinated hydrocarbons detected by SAM at the Rocknest aeolian deposit in Gale Crater, Journal of Geophysical Research, 118, 1955–1973, doi:10.1002/jgre.20144.

Gough, R.V., et al. (2011), Laboratory studies of perchlorate phase transitions: Support for metastable aqueous perchlorate solutions on Mars, Earth and Planetary Science Letters, 312, 371-377, doi:10.1016/j.epsl.2011.10.026.

Gregg, S. and Sing, K. (1982), Adsorption, Surface Area and Porosity, Academic Press, New York.

Grotzinger, J. P., et al. (2014), A habitable fluvio-lacustrine environment at Yellowknife Bay, Gale Crater, Mars. Science, 343(6169), 1242777.

Haberle, R. M. and Jakosky, B.M. (1990), Sublimation and transport of water from the north residual polar cap on Mars, J. Geophys. Res., 95(B2), 1423–1437, doi:10.1029/JB095iB02p01423.

Hamamatsu Photonics Technical Publication: Photon Counting Using Photomultiplier Tubes (1998).

Harmon, C. W., et al. (2010), Hygroscopic growth and deliquescence of NaCl nanoparticles mixed with surfactant SDS, The Journal of Physical Chemistry B, 114(7), 2435-2449.

Harri, A.M., et al. (2014), Mars Science Laboratory relative humidity observations: initial results. J. Geophys. Res. Planets 119, 2132–2147, doi:10.1002/2013JE004514.

Head, J. W., et al. (1999), Possible ancient oceans on Mars: evidence from Mars Orbiter Laser Altimeter data, Science, 286(5447), 2134-2137.

Hecht, M. H., et al. (2009), Detection of perchlorate and the soluble chemistry of Martian soil at the Phoenix Lander site, Science, 325, 64–67, doi:10.1126/science.1172466.

Hudson, T., et al. (2007), Laboratory experiments and models of diffusive emplacement of ground ice on Mars, Journal of Geophysical Research, 114, E01002, doi:10.1029/2008JE003149.

Hudson, T. L., Aharonson, O., and Schorghofer, N. (2009), Laboratory experiments and models of diffusive emplacement of ground ice on Mars, J. Geophys. Res., 114, E01002, doi:10.1029/2008JE003149.

Inaba, H., and Kobayasi, T. (1972), Laser-Raman radar - Laser-Raman scattering methods for remote detection and analysis of atmospheric pollution, Opto-electronics, 4(2), 101-123.

Jakosky, B. M. and Farmer, C. B. (1982), The seasonal and global behavior of water vapor in the Mars atmosphere: Complete global results of the Viking atmospheric water detector experiment, Journal of Geophysical Research: Solid Earth, 87(B4), 2999-3019.

Jakosky, B. M., Zent, A. P., and Zurek, R. W. (1997), The Mars water cycle: Determining the role of exchange with the regolith, Icarus, 130(1), 87-95.

Janchen, J., et al. (2006), Investigation of the water sorption properties of Mars-relevant micro- and mesoporous minerals, Icarus, 180(2), 353–358, doi:10.1016/j.icarus.2005.10.010

Jänchen, J., Möhlmann, D., and Stach, H. (2007), Water and carbon dioxide sorption properties of natural zeolites and clay minerals at martian surface temperature and pressure conditions. Stud. Surf. Sci. Catal. 170, 2116-2121, doi:10.1016/S0167-2991(07)81108-6.

Janchen, J., et al. (2009), The H2O and CO2 adsorption properties of phyllosilicate-poor palagonitic dust and smectites under Martian environmental conditions, Icarus, 200(2), 463-467, doi:10.1016/j.icarus.2008.12.006.

Jha, B. and Singh, D.N. (2016), Basics of Zeolites, In Fly Ash Zeolites (pp. 5-31). Springer Singapore.

Keller, J. U. and Staudt, R. (2005), Gas adsorption equilibria: experimental methods and adsorptive isotherms, Springer Science & Business Media.

Kingma, K.J. and Hemley, R.J. (1994), Raman spectroscopic study of microcrystalline silica, American Mineralogist, 79 (3-4), 269-273.

Komguem, L., Whiteway, J. A., Dickinson, C., Daly, M., and Lemmon, M. T. (2013), Phoenix LIDAR measurements of Mars atmospheric dust, Icarus, 223(2), 649-653.

Kounaves, S. P., et al. (2009), The MECA Wet Chemistry Laboratory on the 2007 Phoenix Mars Scout Lander, J. Geophys. Res., 114, E00A19, doi:10.1029/2008JE003084.

Kounaves, S.P., et al. (2014), Evidence of martian perchlorate, chlorate, and nitrate in Mars meteorite EETA79001: Implications for oxidants and organics, Icarus, 229, 206-213, doi:10.1016/j.icarus.2013.11.012.

Kounaves, S. P., et al. (2014), Identification of the perchlorate parent salts at the Phoenix Mars landing site and possible implications, Icarus, 232, 226-231.

Lawson, C.L. and Hanson, R.J. (1974), Solving Least Squares Problems, Prentice-Hall, Chapter 23.

Leighton, R. B., and Murray, B. C. (1966), Behavior of carbon dioxide and other volatiles on Mars, Science, 153(3732), 136-144.

Liu, Z., et al. (2006), Estimating random errors due to shot noise in backscatter lidar observations, Applied optics, 45(18), 4437-4447.

Lopez-Reyes, G., et al. (2013), Analysis of the scientific capabilities of the ExoMars Raman Laser Spectrometer instrument, European Journal of Mineralogy, 25(5), 721-733.

Marion, M.G., et al. (2010), Modeling aqueous perchlorate chemistries with applications to Mars, Icarus, 207, doi:10.1016/j.icarus.2009.12.003.

Martin, S. T. (2000), Phase transitions of aqueous atmospheric particles, Chem. Rev., 100(9), 3403–3454, doi:10.1021/cr990034t.

Martín-Torres, F. J., et al. (2015), Transient liquid water and water activity at Gale crater on Mars. Nature Geoscience, 8(5), 357-361.

Martínez, G. M., et al. (2016), Likely frost events at Gale crater: Analysis from MSL/REMS measurements. Icarus, 280, 93-102.

McEwen, A. S., et al. (2011), Seasonal flows on warm Martian slopes, Science, 333(6043), 740-743.

McEwen A. S., et al. (2014), Recurring slope lineae in equatorial regions of Mars, Nature geoscience, 7(1), 53-58. doi:10.1038/ngeo2014.

McKay, C. P., Toon, O. B., and Kasting, J. F. (1991), Making Mars habitable, Nature, 352(6335), 489-496.

Mellon, M. T., Jakosky, B.M. and Postawko, S.E. (1997), The persistence of equatorial ground ice on Mars, J. Geophys. Res., 102(E8), 19357–19369, doi:10.1029/97JE01346.

Mellon, M. T., and Jakosky B.M. (1993), Geographic variations in the thermal and diffusive stability of ground ice on Mars, J. Geophys. Res., 98(E2), 3345–3364, doi:10.1029/92JE02355.

Möhlmann, D. (2005), Adsorption water-related potential chemical and biological processes in the upper martian surface, Astrobiology, 5(6): 770-777. doi:10.1089/ast.2005.5.770.

Moudden, Y., and McConnell, J. C. (2005), A new model for multiscale modeling of the Martian atmosphere, GM3, Journal of Geophysical Research: Planets, 110(E4).

Mousis, O., et al. (2016), Martian zeolites as a source of atmospheric methane, Icarus, 217, 1-6, doi:10.1016/j.icarus.2016.05.035

Neary L., Daerden, F. (2018), The GEM-Mars general circulation model for Mars: Description and evaluation, Icarus, 300, doi:10.1016/j.icarus.2017.09.028.

Nelli, S. M., N. O. Renno, J. R. Murphy, W. C. Feldman, and S. W. Bougher (2010), Simulations of atmospheric phenomena at the Phoenix landing site with the Ames General Circulation Model, J. Geophys. Res., 115, E00E21, doi:10.1029/2010JE003568.

Nikolakakos, G., and Whiteway, J.A. (2015), Laboratory investigation of perchlorate deliquescence at the surface of Mars with a Raman scattering lidar, Geophys. Res. Lett., 42, 7899–7906, doi:10.1002/2015GL065434.

Nikolakakos, G., and J.A. Whiteway (2018), Laboratory study of adsorption and deliquescence on the surface of Mars, Icarus, 308, 221-229, doi:10.1016/j.icarus.2017.05.006.

Ojha, L., et al. (2015), Spectral evidence for hydrated salts in recurring slope lineae on Mars, Nature Geoscience, 8, 829–832, doi:10.1038/ngeo2546.

Patel, M.B., et al. (1983), Single crystal Raman spectra of magnesium and zinc perchlorate hexahydrates, Journal of Raman Spectroscopy, 14, 406-409, doi:10.1002/jrs.1250140609.

Pearl, J. C., M. D. Smith, B. J. Conrath, J. L. Bandfield, and P. R. Christensen (2001), Observations of Martian ice clouds by the Mars Global Surveyor Thermal Emission Spectrometer: The first Martian year, J. Geophys. Res., 106(E6), 12325–12338, doi:10.1029/1999JE001233.

Pelletier, M. J. (1999), Analytical applications of Raman spectroscopy, Wiley-Blackwell.

Perez, R., et al. (2017), The supercam instrument on the NASA Mars 2020 mission: optical design and performance, In International Conference on Space Optics—ICSO 2016 (Vol. 10562).

Pestova, O.N., et al. (2005), Polythermal Study of the Systems M(ClO4)2-H2O, Russian Journal of Applied Chemistry, 78 (3), 409-413.

Petrucci, R. H., and Harwood, W. S. (1997), General Chemistry, Principles and Modern Applications, Prentice Hall.

Poulet, F., et al. (2010). Mineralogy of the Phoenix landing site from OMEGA observations and how that relates to in situ Phoenix measurements, Icarus, 205(2), 712-715, doi: 10.1016/j.icarus.2009.10.007.

Pruppacher, H. R., and Klett, J. D. (2012), Microphysics of Clouds and Precipitation: Reprinted 1980, Springer Science & Business Media.

Renno, N. O., et al. (2009), Possible physical and thermodynamical evidence for liquid water at the Phoenix landing site, Journal of Geophysical Research, 114, E00E03, doi:10.1029/2009JE003362.

Rivera-Valentin, E.G. and Chevrier, V.F. (2015), Revisiting the Phoenix TECP data: Implications for regolith control of near-surface humidity on Mars, Icarus, 253, 156-158, doi:10.1016/j.icarus.2015.03.003

Robertson, K. and Bish, D. (2011), Stability of phases in the Mg(ClO4)2·nH2O system and implications for perchlorate occurrences on Mars, Journal of Geophysical Research, 116, E07006, doi:10.1029/2010JE003754.

Rouquerol, J., et al. (2013), Adsorption by powders and porous solids: principles, methodology and applications. Academic press.

Ruff, S.W. (2004), Spectral evidence for zeolite in the dust on Mars, Icarus 168, 131-143, doi:10.1016/j.icarus.2003.11.003

Rull, F., et al. (2017), The Raman Laser Spectrometer for the ExoMars Rover Mission to Mars, Astrobiology, 17(6-7), 627-654.

Rummel, J.D., et al. (2014), A New Analysis of Mars "Special Regions": Findings of the Second MEPAG Special Regions Science Analysis Group (SR-SAG2), Astrobiology, 14(11): 887-968, doi:10.1089/ast.2014.1227.

Ruthven, D.M. (2006), Fundamentals of adsorption equilibrium and kinetics in microporous solids, Adsorption and Diffusion, pp. 1-43, Springer, Berlin, Heidelberg.

Savijarvi, H., et al. (2016), The diurnal water cycle at curiosity: role of exchange with the regolith. Icarus 265, 63–69. doi:10.1016/j.icarus.2015.10.008.

Schmidt, F., et al. (2017), Formation of recurring slope lineae on Mars by rarefied gas-triggered granular flows, Nature Geoscience, 10(4), 270-273.

Smith, D. E., et al. (1999), The global topography of Mars and implications for surface evolution, Science, 284(5419), 1495-1503.

Smith, E., and Dent, G. (2013), Modern Raman spectroscopy: a practical approach, John Wiley & Sons.

Smith, M. D. (2004), Interannual variability in TES atmospheric observations of Mars during 1999–2003. Icarus, 167(1), 148-165.

Smith, M. L., et al. (2014), The formation of sulfate, nitrate and perchlorate salts in the martian atmosphere, Icarus, 231, 51-64.

Smith, P. H., et al. (2009), H2O at the Phoenix landing site, Science, 325, 58–61, doi:10.1126/science.1172339.

Spinrad, H., Münch, G., & Kaplan, L. D. (1963), Letter to the Editor: the Detection of Water Vapor on Mars. The Astrophysical Journal, 137, 1319.

Stillman, D. E., and Grimm, R.E. (2011), Dielectric signatures of adsorbed and salty liquid water at the Phoenix landing site, Mars, Journal of Geophysical Research, 116, E09005, doi:10.1029/2011JE003838.

Stillman, D. E., et al. (2014), New observations of Martian southern mid-latitude recurring slope lineae (RSL) imply formation by freshwater subsurface flows, Icarus 233, 328–341.

Stillman, D. E., et al. (2016), Observations and modeling of northern mid-latitude recurring slope lineae (RSL) suggest recharge by a present-day Martian briny aquifer, Icarus 265, 125–138.

Svitek, T., and Murray, B. (1990), Winter frost at Viking Lander 2 site, J. Geophys. Res., 95(B2), 1495–1510, doi:10.1029/JB095iB02p01495.

Tamppari, L.K., et al. (2010), Phoenix and MRO coordinated atmospheric measurements, Journal of Geophysical Research, 115, E00E17, doi:10.1029/2009JE003415.

Taylor, P., et al. (2010), On pressure measurement and seasonal pressure variations during the Phoenix mission, Journal of Geophysical Research, 115, E00E15, doi:10.1029/2009JE003422.

Tomkinson, T., et al. (2013). Sequestration of Martian CO2 by mineral carbonation. Nature communications, 4, 2662.

Toner, J. D., et al. (2014), Soluble salts at the Phoenix Lander site, Mars: A reanalysis of the Wet Chemistry Laboratory data, Geochimica et Cosmochimica Acta, 136, 142-168, doi:10.1016/j.gca.2014.03.030.

Toner, J.D., et al. (2014b), The formation of supercooled brines, viscous liquids, and low-temperature perchlorate glasses in aqueous solutions relevant to Mars, Icarus, 233, 36-47, doi:10.1016/j.icarus.2014.01.018.

Trokhimovskiy, A., et al. (2015), Mars' water vapor mapping by the SPICAM IR spectrometer: Five martian years of observations, Icarus, 251, 50-64.

Trumpolt, C. W., et al. (2005), Perchlorate: sources, uses, and occurrences in the environment. Remediation Journal, 16(1), 65-89.

Urbansky, E. T. (1998), Perchlorate chemistry: implications for analysis and remediation, Bioremediation Journal, 2(2), 81-95.

Urbansky, E. T., and Brown, S. K. (2003), Perchlorate retention and mobility in soils, Journal of Environmental Monitoring, 5(3), 455-462.

Visioli, A. (2006), Practical PID control, Springer Science & Business Media.

Werner, S. C. (2009), The global martian volcanic evolutionary history, Icarus, 201(1), 44-68.

Whiteway, J. A., et al. (2008), LIDAR on the Phoenix Mars Mission, Journal of Geophysical Research, 113, E00A08, doi:10.1029/2007JE003002.

Whiteway, J. A., et al. (2009), Mars water-ice clouds and precipitation, Science, 325, 68–70, doi:10.1126/science.1172344.

Workman Jr, J., and Springsteen, A. (1998), Applied spectroscopy: a compact reference for practitioners. Academic Press.

Wiens, R. C., et al. (2016), The SuperCam remote sensing instrument suite for Mars 2020. In 47th Lunar and Planetary Science Conference (p. 1322).

Wray, J. J., et al. (2009), Diverse aqueous environments on ancient Mars revealed in the southern highlands. Geology, 37 (11), 1043–1046. doi:10.1130/G30331A.1.

Yu, Y., et al. (2001), Characterization of aluminosilicate zeolites by UV Raman spectroscopy, Microporous and Mesoporous Materials, 46 (1), 23–34, doi:10.1016/S1387-1811(01)00271-2.

Zent, A. P., and Quinn, R.C. (1995), Simultaneous adsorption of CO2 and H2O under Mars-like conditions and application to the evolution of the Martian climate, J. Geophys. Res., 100(E3), 5341–5349, doi:10.1029/94JE01899.

Zent, A. P., Howard, D.J., and Quinn R.C. (2001), H2O adsorption on smectites: Application to the diurnal variation of H2O in the Martian atmosphere, J. Geophys. Res., 106(E7), 14667–14674, doi:10.1029/2000JE001394.

Zent, A., et al. (2010), Initial results from the thermal and electrical conductivity probe (TECP) on Phoenix, Journal of Geophysical Research, 115, E00E14, doi:10.1029/2009JE003420.

Zent, A. P., et al. (2016), A revised calibration function and results for the Phoenix mission TECP relative humidity sensor, J. Geophys. Res. Planets, 121, 626–651, doi:10.1002/2015JE004933.